PhD Thesis

Coherent phonon spectroscopy of carbon nanotubes and graphene

Ahmad Ridwan Tresna Nugraha

Department of Physics, Graduate School of Science
Tohoku University

August 2013

Acknowledgments

Abstract

The atomic motions at different locations in a crystal are usually at random phase. However, when the atoms receive ultrashort force they can start oscillating at the same time and become in-phase in the crystal lattices. These lattice vibrations are called coherent phonons. Single wall carbon nanotubes (SWNTs) and graphene nanoribbons (GNRs) have been particularly an important material providing a one-dimensional model system to study the dynamics and interactions of electrons and phonons. These properties are known to be very sensitive to their geometrical structure. With rapid advances in ultrafast pump-probe spectroscopy, it has recently been possible to observe lattice vibrations of SWNTs in terms of the oscillations of either the differential transmittance or reflectance corresponding to the coherent phonon oscillations, although the related phenomena in GNRs are not observed yet.

In this thesis, we develop a microscopic theory for the generation and detection of coherent phonons for SWNTs and GNRs within an tight binding model and effective mass theory. We particularly examine the so-called radial breathing mode (RBM) and radial breathing like mode (RBLM), in SWNTs and GNRs, respectively, in which the tube diameter and the ribbon width can initially expand or contract depending on the SWNT and GNR geometrical structure, and depending on the laser excitation energy. We find that the expansion and contraction of these materials originate from the electron-phonon interaction of each SWNT and GNR as a function of the one-dimensional wavevectros of these materials. Based on our calculations, we predict the expansion and contraction phenomena for different SWNT and GNR structures.

Furthermore, it is known that excitons, or electron-hole pairs bound by Coulomb interaction, have a large binding energy (up to 1 eV) so that the excitons can survive even at room temperature. All optical processes in SWNTs thus should be expressed in terms of excitons. The excitons in SWNTs are localized spatially with a typical size of about 1 nm. Therefore, when we consider the exciton-phonon interactions the coherent vibrations should occur locally at each site where an exciton is exists. In order to connect the observed macroscopic oscillations in terms of the differential transmittance (or reflectance) with the microscopic localized vibrations, we propose theoretically that the pump-probe spectroscopy can only measure a spatial average of localized coherent phonon amplitudes in the SWNTs. By taking an average of the cal-

culated amplitudes per nanotube length, we obtain time-dependent coherent phonon amplitudes that resemble homogeneous oscillations observed in the pump-probe experiments. We also calculate the time-dependent absorption spectra as a result of macroscopic atomic displacements induced by the coherent phonon oscillations and thus reproduce the oscillation feature of the transmission or reflectance in the pump-probe measurements.

Contents

Chapter 1

Introduction

1.1 Purpose of the study

Low-dimensional nanocarbon materials, such as single wall carbon nanotubes (SWNTs), graphene, and graphene nanoribbons (GNRs), have been an exciting material to be explored because of their unique physical properties, which are very promising for future optoelectronic applications [1, 2, 3]. In particular, SWNTs (graphene sheets rolled up into a seamless cylinder) and GNRs (strips of graphene sheet with ultra-thin width) provide a one-dimensional (1D) model system for studying the dynamics and interactions of electrons, photons, and phonons, that strongly depend on their geometrical structure [4]. With rapid advances in ultrafast pump-probe spectroscopy, it is possible to probe electronic and vibrational dynamics of solids in real time by measuring the change in transmittance ($\Delta T/T$) or reflectance ($\Delta R/R$) within a pump-probe technique. Oscillations observed in the transmittance or reflectance as a function of probe delay time are utilizing the so-called coherent phonons, which are collective and in-phase atomic vibrations in solids.

Coherent phonons can be generated when the pump pulse width is much smaller than a typical phonon period. For example, the radial breathing modes (RBMs) in SWNTs, which correspond to the lattice vibration along the nanotube diameter direction, have a phonon period of about $100-150$ fs, thus sub-10-fs pulses are commonly used to generate the RBM phonons coherently [5]. Recent experiments have given us some hints that the coherent phonon amplitudes for a particular SWNT strongly depends on the excitation energy [6, 7, 8]. Moreover, it was also noticed that some SWNTs might start their coherent RBM vibrations by initially expanding their diameters [8], while others might start their RBM vibrations by initially shrinking their diameters [9]. However, the systematic behavior related to the SWNT structure is not well-understood yet. On the other hand, there were no observations on the coherent phonons in GNRs system, yet we think that coherent phonon behavior in the GNRs is

similar to that in the SWNTs because they share similar uniqueness on their electronic structure.

The purpose of the present study is to understand and to predict theoretically coherent phonon properties in both SWNTs and GNRs. In this thesis, a microscopic theory for the generation and detection of coherent phonons in SWNTs and GNRs is developed within the extended tight-binding approximation and effective mass theory. For SWNTs, we also particularly consider the excitonic effects on the coherent phonon generation. Since the physical properties of SWNTs and GNRs are characterized by their geometrical structures, we present the dynamics of coherent phonons in SWNTs and GNRs with different structures. Based on some special characteristics of each material, the purpose of this thesis is categorized into two subthemes.

1.1.1   Coherent phonon amplitudes in SWNTs and GNRs

In SWNTs and GNRs, there are several phonon modes that can be coherently excited. We will particularly focus on the so-called the radial breathing mode (RBM) phonons in SWNTs and radial breathing like mode (RBLM) phonons in GNRs. The RBM phonons correspond to the radial oscillations along the nanotube diameter, while the RBLM phonons correspond to the oscillations along the nanoribbon width. These two modes are interesting because they are directly related to the change in the SWNT and GNR electronic properties, i.e. the bandgaps can be modulated by the coherent RBM and RBLM oscillations. In this thesis, we calculate the RBM and RBLM coherent phonon amplitudes as a function of laser excitation energy. We also consider different geometrical structures of SWNTs and GNRs, characterized by the nanotube chirality (n, m) and the number of carbon atom pairs in the ribbon width N_{ab}, respectively. We would like to understand how the SWNT diameter and the GNR width could change in response to femtosecond laser excitation. We will discuss that the coherent phonon amplitudes change the sign depending on the pump excitation energy, and that the phase of oscillations for each SWNT or GNR is strongly structure-dependent. From this simulation, we propose a simple rule that determines whether the SWNT diameter and GNR width initially increase or decrease.

1.1.2   Excitonic effects on coherent phonon dynamics in SWNTs

In 1D materials such like SWNTs, a photoexcited electron and a hole can form excitons, strongly bound by Coulomb interaction. The excitons in SWNTs exist even at room temperature. Therefore, we should discuss the electron-phonon and electron-photon interactions in terms of the exciton-phonon and exciton-photon interactions, respectively. The problem which then arises is that how the excitons will affect the coherent phonon oscillations. As observed in the experiments, $\Delta T/T$ or $\Delta R/R$ data show oscillating feature as a function of time, which indicate that the phonon oscilla-

tions have the same phase along the nanotube axis. We can observe such macroscopic oscillations of $\Delta T/T$ or $\Delta R/R$ because the coherent phonon oscillations modulate the electronic and optical properties of the SWNTs. However, the excitons in SWNTs are localized spatially with a typical size of about 1 nm in the direction along the nanotube axis and thus when we consider the exciton-phonon interactions the coherent oscillations should occur locally at the exciton sites. We then need to bridge such a gap between the macroscopic picture of coherent phonon spectroscopy and the microscopic picture of excitons, which will be discussed by assuming that coherent phonon spectroscopy can only measure a spatial average of localized coherent amplitudes in the SWNTs.

1.2   Organization of the thesis

This thesis is organized into six chapters. Chapters 1-3 form basic foundations of this thesis. In Chapter 1, all necessary backgrounds for the thesis are introduced. In Chapter 2, the fundamentals of carbon nanotubes and graphene are reviewed, especially regarding the geometrical structure, electronic properties, and vibrational properties. The electronic structure is considered within the simple tight-binding (STB) and extended tight-binding (ETB) models. The vibrational properties are calculated by the force constant model. In Chapter 3, the calculation methods and formulations used in this thesis are discussed. The microscopic coherent phonon theory based on some previous works is reviewed [10, 11], and is extended in the present study for SWNT and GNR systems [12, 13]. The main (original) results of this thesis are presented in Chapters 4 and 5. In Chapter 4, we show the calculation results for coherent phonon amplitudes of SWNTs and GNRs within the ETB model and effective mass theory [12, 13]. In Chapter 5, we show the recent results of excitonic effects on coherent phonons in SWNTs [14]. Finally, in Chapter 6, a summary of this thesis is given.

1.3   General backgrounds

In this section, we review some important backgrounds that motivate the present work. We will start with some general concepts on coherent phonon spectroscopy and then review some recent experimental results related to this thesis.

1.3.1   Coherent phonon spectroscopy

The development of ultrafast, femtosecond laser sources has enabled researchers to study dynamical properties coupled with lattice vibrations of a wide variety of semiconductor nanostructures. These lasers are ideal for studying electron and hole dynamics since scattering times of photoexcited carriers typically span from $10-100$ fs

in most semiconductors. The most common femtosecond experiment is a pump-probe experiment where the pump laser pulse creates a nonequilibrium distribution of photoexcited electrons and holes, while the probe laser pulse is used to trace the change in the dielectric function due to the carriers and lattice vibrations in the materials.

One can study the relaxation dynamics of nonequilibrium photoexcited carriers back to equilibrium by measuring the transmission or reflection of the probe pulse as a function of probe delay time with respect to the pump pulse. The decay of the transmission or reflection of the probe pulse as a function of delay time from the pump pulse provides valuable information concerning details of the nonequilibrium carrier dynamics. The differential transmission $\Delta T/T$ is defined as

$$\frac{\Delta T_t}{T} = \frac{T_t - T}{T}, \tag{1.1}$$

where T is the transmission in the absence of the pump pulse, while T_t is the transmission with the presence of the pump pulse, measured after a certain time delay Δt. It should be noted that depending on the experimental setup of the samples, the measurement of differential reflectance $\Delta R/R$ might be preferable instead of $\Delta T/T$. Information obtained from such experiments includes the electronic structure, scattering rates of photoexcited carriers, relaxation dynamics and mechanisms, and many-body effects in a given material [5].

In addition to the carrier dynamic effects, ultrafast pump-probe experiments produce oscillating signals superimposed on the background carrier dynamics signal. For example, in Fig. 1.1, we show $\Delta T/T$ as a function of time delay of the probe pulse with respect to the time of the pump pulse for a SWNT system. In the raw pump-probe signal shown in Fig. 1.1, we can see oscillating signals in $\Delta T/T$ superimposed on the background carrier dynamics (decay) signal. The beating amplitudes come from superposition of several oscillation frequencies which are close to each other. These oscillations match one of the phonon modes of the material and are assigned as *coherent phonons* [6, 15]. A typical phonon mode can be excited coherently because the ultrashort laser pulse have a duration shorter than the period of the lattice vibration. If we subtract off the background signal, the oscillation can be seen more clearly as shown in the inset of Fig. 1.1. One can perform a Fourier transforms to calculate the power spectrum (or intensity), which is proportional to the square of the Fourier coefficient amplitudes. The power spectrum gives information of the phonon modes that are coherently excited in the system, whereas the original $\Delta T/T$ data provides the real time information of the coherent oscillations. The study of these oscillations is then known as *coherent phonon spectroscopy*. Coherent phonon spectroscopy thus allows the direct measurement of excited state phonon dynamics in the time domain and includes information on the phase of the vibration, the electron-phonon coupling, and the dephasing times [5].
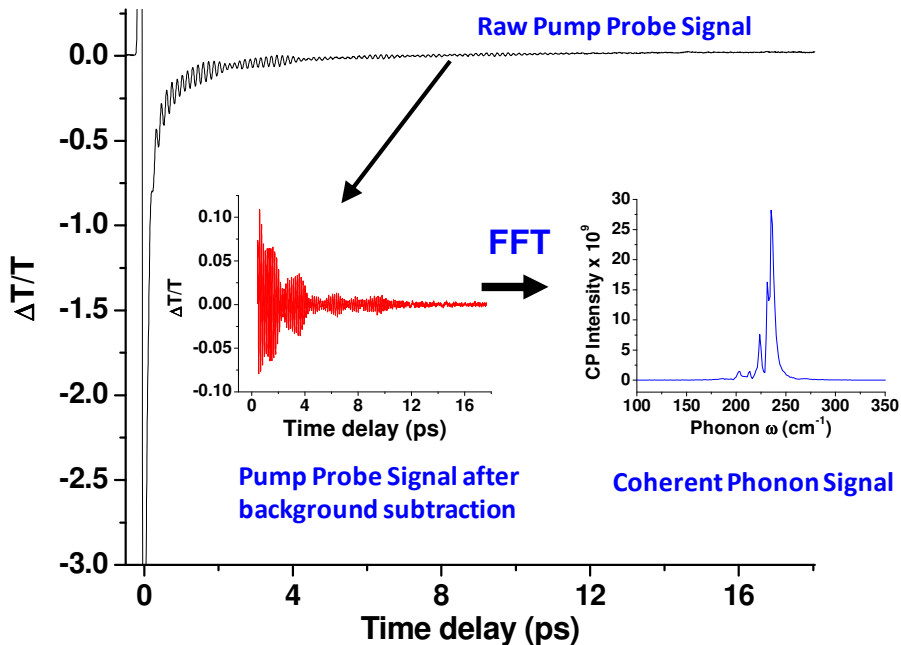
Figure 1.1   Time-resolved change in transmission ($\Delta T/T$) of the laser probe pulse as a function of time delay of probe with respect to the pump pulse for a SWNT system. The oscillations superimposed on the background electron and hole relaxation dynamics signal are known as *coherent phonons*. Inset shows the pump-probe signal after background substraction. To study the coherent phonons, it is necessary to subtract off the signal of background carrier dynamics from the raw pump-probe signal and then performs a Fourier transform to calculate the power spectrum.

1.3.2   Coherent phonons and incoherent phonons

In early years of the coherent phonon research, the oscillations observed in the differential transmission and reflectivity data are interpreted in terms of a phenomenological driven harmonic oscillator [15]. The evolution of a coherent phonon amplitude Q in the presence of a driving force exerted by ultrafast laser pulse can be expressed by

$$\frac{\partial^2 Q(t)}{\partial t^2} + 2\gamma_{\mathrm{D}} \frac{\partial Q(t)}{\partial t} + \omega_0^2 Q(t) = \frac{F(t)}{m}, \tag{1.2}$$

where ω_0 is the frequency of the phonon mode, γ_{D} is the damping parameter, m is the mass of the oscillator, and F is the driving force. This force can be fitted as function of carrier density, temperature, or other parameters of the system. The damping parameter γ_{D} is the inverse of the dephasing time of the coherent phonon mode [16]. However, at that time it was unclear how the coherent phonons can be generated and how the oscillations in $\Delta T/T$ should be described quantum mechanically.

Fig. 1.1: fig/fch1-deltaT.eps
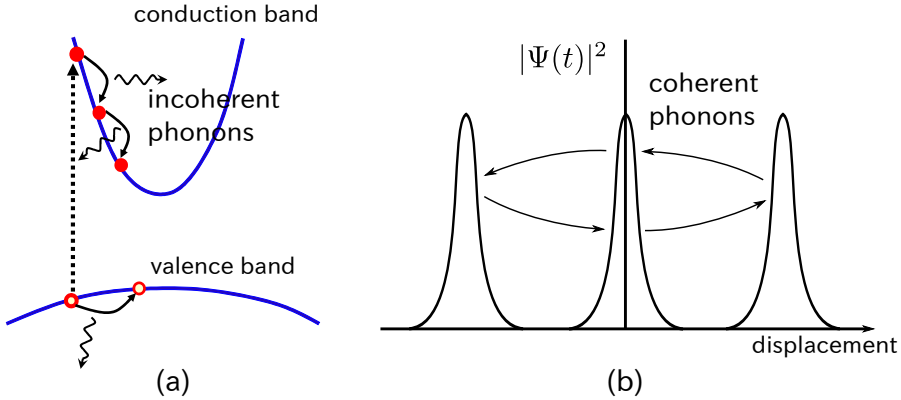
Figure 1.2 (a) Femtosecond laser excitation generates electronhole pairs across the gap which relax and lose energy through phonon emission. These phonons are incoherent phonons and do not lead to oscillations in the differential transmission or reflection. (b) Coherent phonon wavepackets as a function of the harmonic oscillator displacement. These are formed from the superposition of two or more of the eigenstates of the harmonic potential. They oscillate back and forth in the harmonic potential without broadening.

It was then realized that when an ultrafast optical laser pulse rapidly creates photoexcited electron-hole pairs across the bandgap in a semiconductor, the optical and and acoustic phonons emitted during the electron-hole relaxation are actually *incoherent phonons* and are not related to the oscillations observed in the differential transmission or reflectivity spectra [10]. In Fig. 1.2(a) we show an illustration for the incoherent phonons emitted during the photoexcited carrier relaxation. The incoherent phonons are emitted at random times and have no distinct phase relationship and thus not responsible for the oscillations in the pump-probe signal. Instead, the incoherent phonons are responsible for the decay of the background signal. Coherent phonons, on the other hand, are formed from a coherent superposition of phonon harmonic oscillator eigenstates, i.e. the states with definite phonon number. If a large number of phonon harmonic oscillator eigenstates can be excited, then the canonical coherent states can be defined for each complex number z in terms of eigenstate of harmonic oscillator,

$$\Psi^{\mathrm{coh}} = |z\rangle = \sum_n \frac{z^n}{\sqrt{n!}} \mathrm{e}^{-z^2} |n\rangle, \tag{1.3}$$

where $|n\rangle$ are the eigenstates of the harmonic oscillator.

The coherent phonon states in Eq. (1.3) are essentially the same as those used in quantum optics to describe the quasi-classical photon states of the electromagnetic field. These states are eigenfunctions of the phonon annihilation operator $b_{\mathbf{q}}$ for phonons with wavevector q, i.e. $b_{\mathbf{q}}|z\rangle = z|z\rangle$, and represent minimum-uncertainty Gaussian wavepackets that oscillate back and forth in the parabolic potential without

Fig. 1.2: fig/fch1-cohincoh.eps

broadening, as illustrated in Fig. 1.2(b). When the amplitude z is large, the coherent phonons will behave like a macroscopic harmonic oscillator. The idea of quantum mechanical coherent phonon states can thus explain the oscillations of $\Delta T/T$. In general, both coherent and incoherent phonons can be generated at the same time. That is why a typical $\Delta T/T$ data consist of an oscillating feature and also a decay feature, corresponding to the generation of coherent phonons and incoherent phonons, respectively.

1.3.3 Generation mechanism of coherent phonons

Based on the idea of the coherent phonons described above, we might then ask how one can generate coherent phonons. A simple explanation for the generation of the coherent phonons is shown in Fig. 1.3 for two prototypical systems [17]: (a) a bulk semi-conducting system (GaAs), and (b) a molecular system. The electron-phonon coupling in GaAs is weaker than that in the molecular system. Therefore, the electron-phonon coupling is treated as a perturbation to the electronic states (i.e. band structure) in GaAs, while in the molecular system we consider the combined electronic-vibrational levels.

GaAs is a polar semiconductor, thus the electrons in GaAs prefer to couple with the phonons by the polar coupling because the polar coupling is stronger than the deformational electron-phonon coupling. It is then possible to have a depletion region near the surface of the GaAs sample. The depletion region could come either from surface states or an externally applied electric field. The energy band diagram for bottom of the conduction band and top of the valence band are shown in Fig. 1.3(a). Bending of the bands near the surface lead to a depletion of charge carriers for a certain width from the surface. This leads to large external electric fields near the surface. Before photoexcitation, in response to the surface depletion field, the Ga and As ions are slightly displaced by an amount x_1 and x_2 from their equilibrium positions deep within the semiconductor. After photoexcitation by the pump laser pulse, electrons and holes are photoexcited which create carriers near the semiconductor surface that can (partially) screen out the depletion field. If the photoexcited carriers are created on a fast time scale, the displaced Ga and As ions want to return to their equilibrium (no depletion electric field) position and then trigger the coherent oscillation.

A similar situation is shown in Fig. 1.3(b) for a typical molecule. Shown in the figure are the combined electronic and vibrational states for the ground state and the first excited state. The pump pulse creates a rapid photoexcitation of an electron from the ground state energy surface to the excited state energy surface. Since the minimum in the excited state energy surface is at different point from that in the ground state energy surface, the rapid photoexcitation to the higher state energy surface triggers the coherent oscillation.
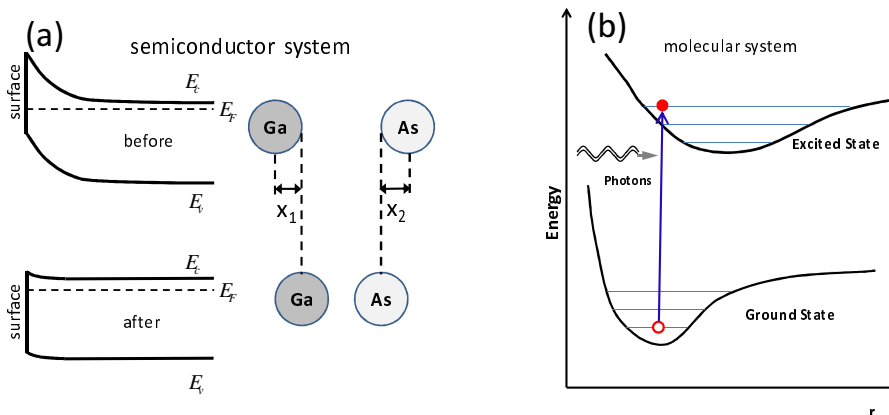
Figure 1.3 Generation mechanisms for coherent phonons. (a) A conventional polar semiconductor like GaAs. Before photoexcitation by the pump pulse, the surface depletion field cause the Ga and As ions to be displaced by an amount x_1 and x_2 from their equilibrium (no depletion field) position. After photoexcitation, the electrons and holes generated near the surface will screen the depletion field, causing the Ga and As ions to return to their equilibrium position, and trigger the coherent phonon. (b) A typical molecule. The combined electronic and vibrational energy levels for the grounds state energy surface and an excited state energy surface are shown. The ground state and excited state energy surfaces have different minima, and thus photoexcitation by the pump pulse from the grounds state to the excited state triggers the coherent phonon and the system wants to move to a new minima.

From these two simple examples, we see that the coherent phonon generation mechanism varies depending on the material properties. However, the coherent phonon oscillations in various materials can be explained within the same equations of motion such like Eq. (1.2). The difference in the generation mechanism between one material and another will particularly contribute to the different form of driving force term in Eq. (1.2). Consideration of such an explicit form of the driving force is actually the main issue of this thesis, especially for the SWNT and GNR systems.

1.3.4   Coherent phonons in SWNTs and GNRs

SWNTs and GNRs are interesting to be studied as a model system for coherent phonon generation because they lie between the simple molecular systems and the bulk semiconducting systems. In addition, the electron-phonon coupling in these carbon based nanostructures is not polar like in GaAs. In calculating and modeling the coherent phonon spectra in carbon nanotubes and graphene, several important effects must be addressed. These include: (1) *electronic structure* (needed to determine the electron and hole states), (2) *optical matrix elements* (needed to determine what states are excited by the pump laser pulse), (3) *phonon modes*, (4) *electron phonon matrix elements* (to determine which coherent phonon modes are triggered by the photoexcited

electrons) and (5) the *generation and detection mechanisms*. Each of these effects will be discussed further in the later chapters.

In the following, we briefly reviewed some experimental observations of coherent phonons in SWNTs and also previous theoretical studies which attempt to explain the coherent phonon properties in SWNTs. The experimental observations for coherent phonons in GNRs, however, are *not available yet* till now, and thus it will be shown in this thesis how the coherent phonon properties in GNRs are predicted similarly to those in SWNTs.

Observation of coherent phonons in SWNTs

Coherent phonon spectroscopy applied to SWNTs has several advantages over other spectroscopic techniques such as resonant Raman spectroscopy and photoluminescence spectroscopy [7, 18]. In coherent spectroscopy there is no photoluminescence signal or Rayleigh scattering background. Coherent phonons in an ensemble of micelle suspended SWNTs have been generated by ultrafast laser pulses and detected using femtosecond pump-probe spectroscopy. These coherent phonon spectroscopy experiments measure periodic changes in nanotube optical properties induced by coherent lattice vibrations and, unlike Raman or photoluminescence spectroscopy, allows one to directly measure phonon dynamics, including phase information, in the time domain.

Using pulse shaping techniques to create a train of pump pulses resonant with the coherent phonon period, it is possible to generate and detect coherent phonons in nanotubes of a specific chirality in an ensemble sample [8, 18]. These resonant coherent phonon spectroscopy experiments provide information on the chirality-dependence of light absorption, coherent phonon generation, and coherent phonon-induced band structure changes. The lowest frequency coherent phonons that can be photoexcited in SWNTs using ultrafast laser pulses are coherent radial breathing mode (RBM) phonons with phonon wavevector $q = 0$ corresponding to a mode in which the diameter of the nanotube periodically expands and contracts.

Actually real-time observation of coherent RBM oscillations is already possible without pulse shaping by applying standard femtosecond pump-probe spectroscopy [6]. However, we will observe several chiralities in the coherent phonon spectra instead of obtaining detailed information on a specific nanotube chirality. Figure 1.4(a) shows transmission modulations of the probe beam induced by coherent lattice modulations, which were generated by pump pulses with a pulse width of 50 fs and a central wavelength of 800 nm (1.55 eV). The time-domain beating profiles reflect the simultaneous generation of several RBM frequencies from nanotubes in the ensemble with different chiralities, which are clearly seen in Fig. 1.4(b) with the Fourier transformation of the time-domain data. Although resonance conditions and mode frequencies lead to the assignment of chiralities to their corresponding peaks, obtaining detailed information on dynamical quantities such as the phase information of phonon oscillations becomes
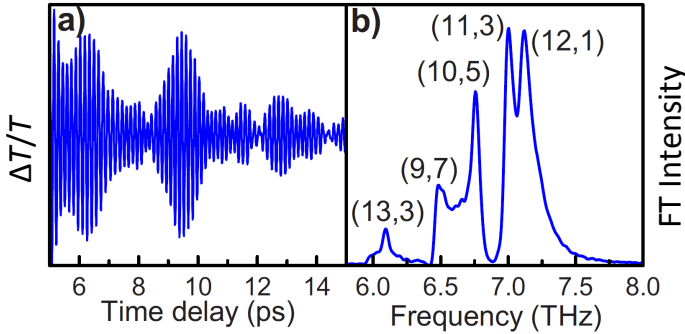
Figure 1.4 Generation and detection of coherent RBM phonons in SWNTs. (a) Time-domain transmission modulations due to coherent RBM vibrations in ensemble SWNT solution that were generated by standard pump-probe spectroscopy without pulse shaping. (b) Fourier transformation of time-domain oscillations with chirality assigned peaks. Reproduced from Ref. [8].

rather challenging. Additionally, if adjacent phonon modes overlap in the spectral domain, this can lead to peak distortions.

By introducing pulse shaping, multiple pulses with different repetition rates are used to excite RBM oscillations. As shown in Figs. 1.5(a)-(d), chirality selectivity was successfully obtained. With the appropriate repetition rate of the pulse trains, a single specific chirality dominantly contributes to the signal, while other nanotubes are suppressed. For example, by choosing a pump repetition rate of 7.07 THz, we can selectively excite only the $(11, 3)$ as seen in Fig. 1.4(a). Similarly, with a pump repetition rate of 6.69 THz, the $(10, 5)$ nanotubes are selectively excited, as seen in Fig. 1.5(b). The accuracy of selectivity depends on the number of pulses in the tailored pulse train as well as the distribution of chiralities in the nanotubes ensemble. Furthermore, selective excitation of a specific chirality also requires the pump energy to be resonant with the corresponding band-to-band transition (in this case the E_{22} transition) for each chirality-specific nanotubes.

The ability to excite single-chirality nanotubes also allows us to perform detailed studies of excited states of single-walled carbon nanotubes. For example, by placing a series of 10 nm bandpass filters in the probe path before the detector, we can measure the wavelength dependence of RBM-induced transmission changes in order to understand exactly how the tube diameter changes during coherent phonon RBM oscillations and how the diameter change modifies the nanotube band structure. In Fig. 1.6, the differential transmission is shown for three cases, from top to bottom, corresponding to probe photon energies above, on, and below resonance, respectively, for selectively excited $(11, 3)$ carbon nanotubes.

Although the transmission is strongly modulated at the RBM frequency 7.07 THz

---

Fig. 1.4: fig/fch1-pulse1.eps
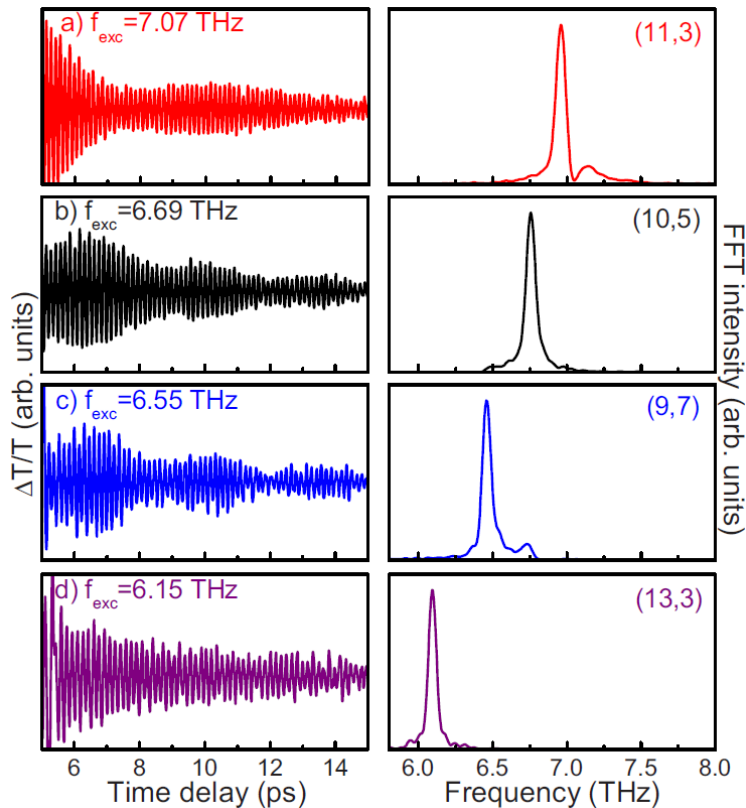
Figure 1.5 (Left) Time-domain coherent RBM oscillations selectively excited by multiple pulse trains via pulse shaping with corresponding repetition rates from 6.15 to 7.07 THz. (Right) Fourier transformations of corresponding oscillations, with their dominant nanotube chirality (n, m). Reproduced from Ref. [8].

for all three cases in Fig. 1.6, the amplitude and phase of oscillations vary noticeably for varying probe wavelengths. Specifically, the amplitude of oscillations becomes minimal at resonance and, in addition, there is clearly a π-phase shift between the above- and below-resonance traces. Since the bandgap energy and diameter are inversely related to each other, and since it is the RBM frequency at which the diameter is oscillating, we can conclude from this data that the energy of the E_{22} resonance is oscillating at the RBM frequency. Namely, when the band gap is decreasing, absorption above (below) resonance is decreasing (increasing), resulting in positive (negative) differential transmission. Furthermore, it is also possible to determine the initial response of the SWNT lattice based on this experiment, i.e. the given nanotube may start vibration by expanding or shrinking its diameter depending on the excitation energy, although more observations are needed to clarify such phenomena.

Fig. 1.5: fig/fch1-pulse2.eps
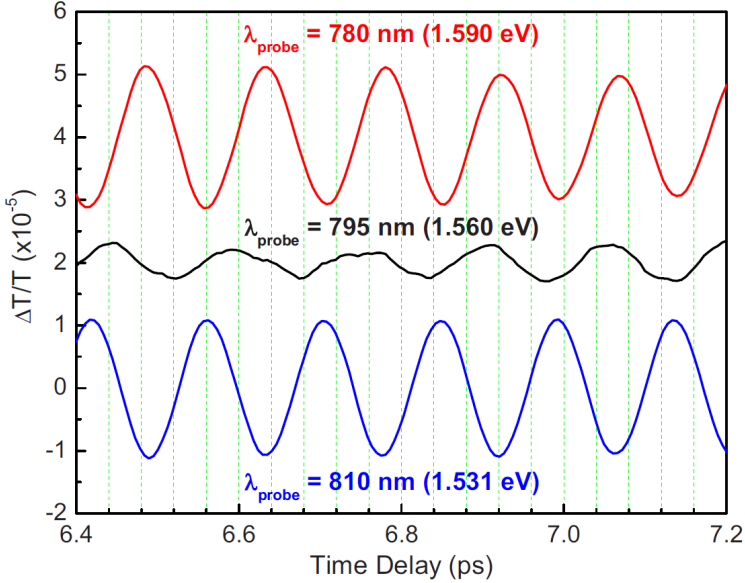
Figure 1.6 Differential transmission as a function of time delay at probe wavelengths of 780, 795, and 810 nm for the selective RBM excitation of the $(11, 3)$ nanotube. There is a π-phase shift between the 780 and 810 nm data. These three wavelengths (from the top to the bottom of the figure) correspond to photon energies above, at, and below the energy of the second exciton resonance, respectively, of the $(11, 3)$ nanotube. Reproduced from Ref. [8].

Previous theoretical studies

There were a number of theoretical studies previously done regarding coherent phonons in SWNTs [19, 20, 21, 22]. However, most of them mainly dealt with molecular-dynamics simulation to study how the defects in SWNTs interact with laser pulses. A particularly useful theoretical study related to this thesis was done by Sanders *et al.* who developed a microscopic theory for the coherent RBM phonon generation [11]. By using a simple tight-binding approximation for the electronic states and force constant model for the phonon dispersion, they calculated coherent phonon intensities for the RBM phonons of two nanotube families, namely, the type-I $[\mathrm{mod}(2n + m, 3) = 1]$ and the type-II $[\mathrm{mod}(2n + m, 3) = 2]$ semiconducting SWNTs, and found that the coherent phonon intensity in type-I nanotubes was generally larger than that in type-II nanotubes.

By calculating the driving force for the coherent phonon generation and solving the equation of motion like that in Eq. (1.2) (but without damping term), Sanders *et al.* also noticed that some SWNTs start their coherent RBM vibrations by initially expanding their diameters, while others start their RBM vibrations by initially shrinking their diameters. As shown in Fig. 1.7, these phenomena might depend on the laser

Fig. 1.6: fig/fch1-pulse3.eps
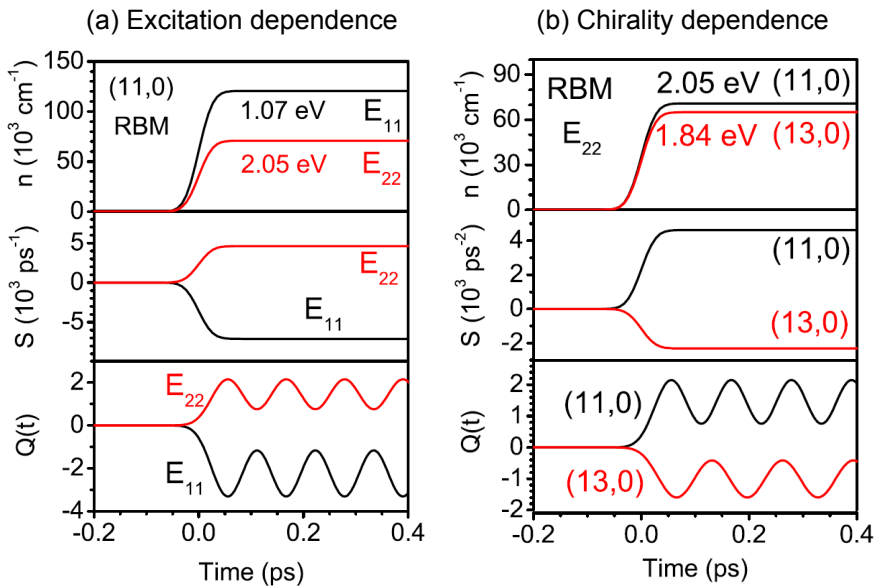
Figure 1.7 (a) Coherent phonon generation in a $(11,0)$ nanotube by photoexcitation at the E_{11} and E_{22} transition energies. (b) Coherent phonon generation in $(11,0)$ type-I and $(13,0)$ type-II semiconducting nanotubes by photoexcitation at the E_{22} transition energy. In both (a) and (b), the upper panel shows the density of photoexcited electron-hole pairs per unit length, the middle panel shows the coherent phonon driving function, and the bottom panel shows the RBM coherent phonon amplitude. Reproduced from Ref. [11].

excitation energy, or these may depend on the nanotube chirality. In Fig. 1.7(a), the photoexcited carrier density $n(t)$, the coherent phonon driving function $S(t)$, and the coherent phonon amplitude $Q(t)$ are plotted for RBM coherent phonons in a $(11,0)$ tube for 50 fs z-polarized laser pulses with photoexcitation energies of 1.07 and 2.05 eV. These energies correspond to the E_{11} and E_{22} transitions in the $(11,0)$ tube, respectively. The photoexcited carrier density $n(t)$ determine the strength of the driving force. However, the coherent phonon driving functions $S(t)$ and amplitudes $Q(t)$ have different signs in the two cases. This means that for photoexcitation at the E_{11} transition in type-I nanotubes the tube diameter decreases and oscillates about a smaller equilibrium diameter. On the other hand, the opposite situation is true for photoexcitation at the E_{22} transition energy.

Furthermore, a comparison of the coherent phonon motion between different chirality, i.e. $(11,0)$ type-I and $(13,0)$ type-II nanotubes, is shown in Fig. 1.7(b), but now the laser energy used to excite the nanotubes is the one that only match the E_{22} transition in each chirality. For the $(11,0)$ tube the pump energy is set to be 2.05 eV and for the $(13,0)$ tube the pump energy is 1.84 eV. It can be seen that for the $(11,0)$ tube the coherent phonon driving function and corresponding coherent phonon am-

plitude are positive (indicating initial expansion of the tube diameter), while for the $(13, 0)$ tube the driving function and corresponding coherent phonon amplitude are found to be negative (indicating initial contraction of the tube diameter. A detailed physical reason for the excitation energy-dependent and chirality-dependent coherent phonon amplitude is not yet understood in that work. Such properties will be one of main issues to be discussed in this thesis, especially to understand the origin of the coherent phonon phenomena, and to also apply the theory for the graphene nanoribbon systems.

1.3.5 Excitons in carbon nanotubes

In this part we briefly review some historical aspects of the finding of excitons in SWNTs and how the excitons can affect optical properties of SWNTs. We will also give a general idea for the excitonic effects on coherent phonon dynamics in SWNTs.

Basically, an exciton consists of a photo-excited electron and a hole bound to each other by the Coulomb interaction in a semiconducting material. In most semiconductors, we can calculate the binding energy of an exciton in bulk materials by a hydrogenic model with a reduced effective mass and a dielectric constant. The resulting binding energy is typically on the order of $10 \, \text{meV}$, thus optical absorption to exciton levels is usually observed only at low temperatures. However, in SWNTs, because of its 1D properties, the electron-hole attraction energy becomes larger and can be as large as $1 \, \text{eV}$, so exciton effects can be observed at room temperature. Excitons are therefore essential for explaining optical processes in SWNTs.

Pioneering researches on excitons in SWNTs originally came from a curiousity that there always be systematic discrepancies between the calculated single particle bandgaps and the optical transition energies E_{ii} observed in some experiments [23, 24, 25]. To explain the observed E_{ii}, much insight has actually been gained from the simple (nearest-neighbor) tight-binding (STB) model of the single particle band structure of SWNTs [26]. This method predicts the transition energies varying approximately as the inverse of diameter and having a weak dependence on the chiral angle, as shown in the STB Kataura plot (energy as a function of diameter) in Fig. 1.8(a). However, experimental results point out the fact that the single particle approximation is insufficient for an accurate description of the optical transitions in SWNTs. For example, as has been reported by Weisman *et al.*, the E_{ii} values calculated by the STB model are lower than those measured in their photoluminescence experiment [25]. They also observed the so-called family spread, in which nanotubes with the same $(2n + m)$ show a unique pattern for the smaller diameter.

The electron-electron and electron-hole interactions change the E_{ii} dependence on diameter significantly. Both the electron-electron and electron-hole interactions are due to the screened Coulomb interactions. The former describes the repulsive energy,
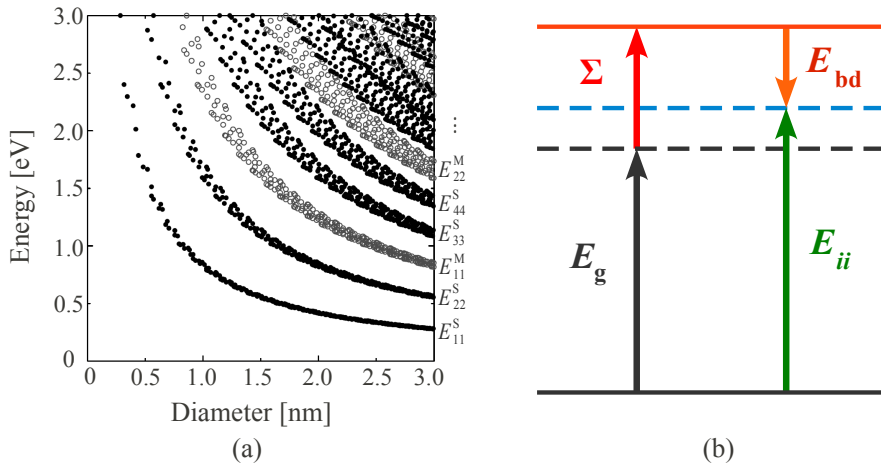
Figure 1.8 (a) Optical transition energy as a function of nanotube diameter, known as the Kataura plot, considered within the STB approximation. The vertical energy axis is simply the nanotube bandgap [26]. (b) Single particle band gap E_g is not simply the transition energy. Self energy Σ and binding energy $E_{\rm bd}$ corrections give the true transition energy E_{ii}.

called self-energy Σ, that is needed to add an additional electron to the system, hence, increases the band gap. In contrast, the electron-hole interaction gives the attractive Coulomb interaction, called exciton binding energy $E_{\rm bd}$, which lowers the excitation energy. The overall effect is a blue-shift so that the positive self energy dominates over the negative exciton binding energy. This is illustrated in Fig. 1.8(b).

The importance of many-body effects in the form of excitonic electron-hole attraction and Coulombic electron-electron repulsion in SWNTs was discussed extensively in the context of the so-called ratio problem [23, 24], where the ratio between the second and first transition energies in semiconducting SWNTs are not equal to two as predicted by the STB model [26]. Some experiments such as two-photon absorption measurements [27, 28], then provided strong evidence for the excitonic nature of the lower energy transition. In particular, a two-photon experiment by Wang *et al.*, which is the first breakthrough in the nanotube $E_{\rm bd}$ measurements, is described in Fig. 1.9, after Ref. [27].

From the theoretical point of view, the importance of excitons in SWNTs was introduced much earlier by T. Ando who studied excitations of nanotubes within a static screened Hartree-Fock approximation [29]. He especially calculated the dynamical conductivity in SWNTs taking the exciton effects into account. After some experimental results started to show the rise of excitons, detailed first-principles calculations of the effects of many-body interactions on the optical properties of SWNTs were then performed [30, 31]. Some descriptions of excitons in nanotubes based on simpler or

---

Fig. 1.8: fig/fch1-kata.eps
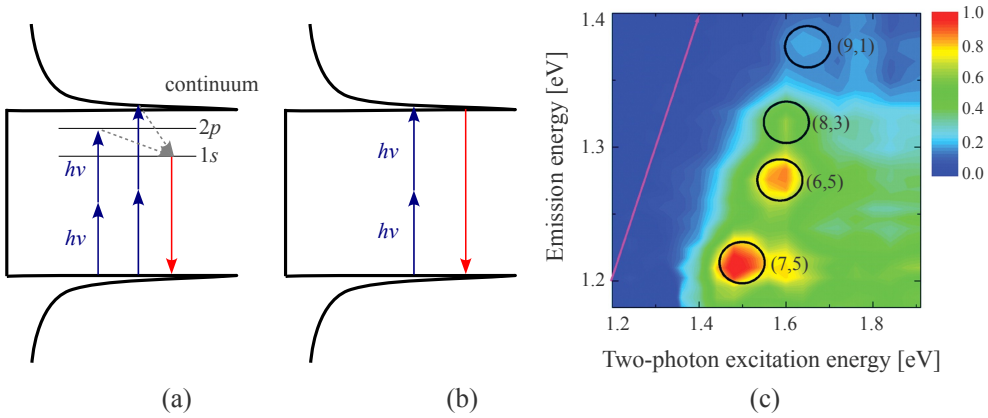
Figure 1.9 Two-photon experiment by Wang *et al.* [27]. (a) In the exciton picture, the $1s$ exciton state is forbidden under two-photon excitation. The $2p$ exciton and continuum states are excited. They relax to the $1s$ exciton state and fluoresce through a one-photon process. (b) In the simple band picture, two-photon excitation energy is the same as emission energy, but this case is not observed. (c) Contour plot of two-photon excitation spectra of SWNTs. By comparison with the solid line describing equal excitation and emission energies, it is clear that the two-photon excitation peaks are shifted above the energy of the corresponding emission feature. The large shift arises from the excitonic nature of the nanotube optical transitions. E_{bd} is found to be as large as up to $1\,\mathrm{eV}$, thus excitons play an important role in the nanotube optics.

different models were also developed [32, 33].

In this thesis, we will use the extended tight-binding (ETB) model to calculate the exciton energies and corresponding wavefunctions based on the previous work by Jiang *et al* [34, 35]. The Bethe-Salpeter equation is solved for obtaining the excitation energies E_{ii} that already include the self energy corrections and the exciton binding energy. The ETB model includes the curvature effects through the σ-π hybridization that cannot be neglected for nanotubes of small diameter. Furthermore, exciton-photon and exciton-phonon matrix elements can be obtained to replace the electron-photon and electron-phonon interactions as the driving force for the coherent phonon oscillations. It is found that the excitons in SWNTs are localized spatially with a typical size of about $1\,\mathrm{nm}$. Therefore, when we consider the exciton-phonon interactions the coherent vibrations should occur locally at each site where an exciton is generated.

1.3.6   Lineshapes of coherent phonon excitation profile

Another issue related to the presence of excitons in SWNTs is regarding the lineshapes of the coherent phonon excitation profile, i.e. the coherent phonon signal intensity plot-

---

Fig. 1.9: fig/fch1-tp.eps
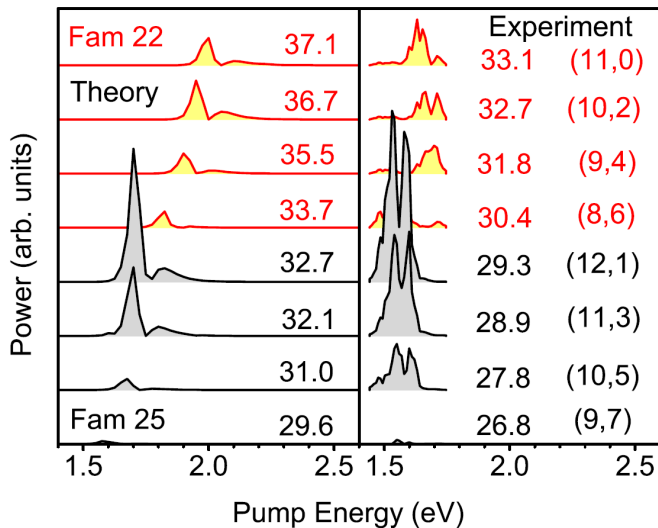
Figure 1.10 Coherent phonon intensity at the RBM frequency as a function of pump-probe energy for several type-I semiconducting nanotubes at the E_{22} transition. The experimental coherent phonon spectra are in the right panel and the simulated coherent phonon spectra are in the left panel. The upper four curves in each panel are for nanotubes within family $\mathrm{mod}(2n + m, 3) = 22$ and the lower four curves are for tubes within $\mathrm{mod}(2n + m, 3) = 25$. Each curve is labeled with the chirality (n, m) and the RBM phonon energy in meV is given on the plots.

ted as a function of several different excitation energies in a given SWNT. It was firstly noticed by Lim *et al.* that the coherent phonon excitation profile for a particular mode shows symmetric double-peak features [7]. They argued that such features are directly related to the excitonic nature of the SWNT. Furthermore, Sanders *et al.* also calculated the coherent phonon intensity within the single particle picture and compared it with the experimental data. They found a clear difference in the lineshape of the intensity, as shown in Fig. 1.10. Both theoretical calculation and experimental results show two peaks; however, the calculation within the single particle picture give asymmetric lineshapes in the double peak-features, unlike the experimental observations which give symmetric lineshapes.

The reason why the symmetric double-peak features appear in the coherent phonon excitation profile can be explained as follows. The generation of coherent RBM phonons modifies the electronic structure of SWNTs and thus it can be detected as temporal oscillations in the transmittance of the probe beam. Since the RBM is an isotropic vibration of the nanotube lattice in the radial direction, i.e. the diameter periodically oscillates at frequency of ω_{RBM}, this causes the band gap E_g to also oscillate at ω_{RBM} because E_g directly depends on the nanotube diameter (roughly $E_g \propto 1/d_t$).

Fig. 1.10: fig/fch1-line1.eps
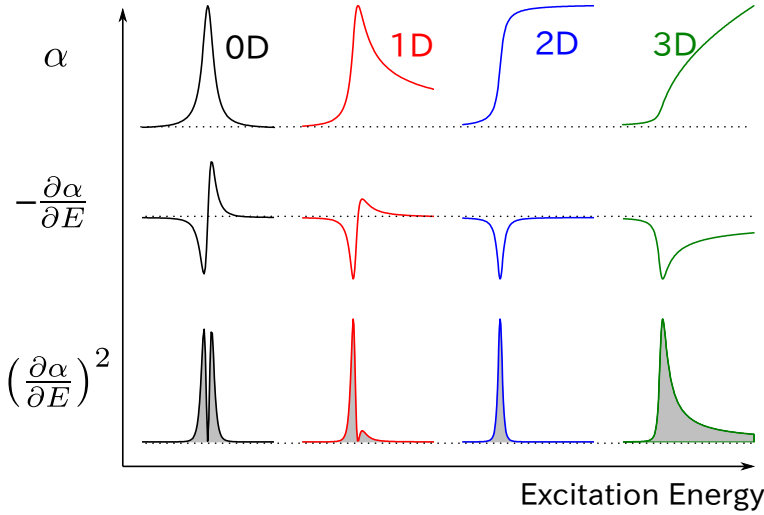
Figure 1.11 Schematic dimensionality dependence of coherent phonon intensity as function of photon energy. Top row: absorption coefficient versus photon energy for 0, 1, 2, and 3-dimensional carbon structures. Middle row: negative of the derivative of the absorption coefficient proportional to transient differential transmission. Bottom row: square of the derivative of the absorption coefficient proportional to the coherent phonon intensity. The absorption curves have been convoluted to take into account lifetime broadening of the states.

As a result, interband transition energies oscillate in time, leading to ultrafast modulations of optical constants at ω_{RBM}, which naturally explains the oscillations in probe transmittance. Furthermore, these modulations imply that the absorption coefficient $\alpha(E)$ at a fixed probe photon energy E is modulated at ω_{RBM}. Correspondingly, the photon energy dependence of the coherent phonon signal shows a derivative-like behavior. The excitonic absorption coefficient has a symmetric lineshape with a single peak, the derivative will give the symmetric double-peak feature, in contrast to the asymmetric shape expected from the 1D van Hove singularity.

More explicitly, the effect on the absorption α for small changes in the gap can be modeled by

$$\alpha(E - E_g) \approx \alpha(E - E_g^0) - \frac{\partial \alpha(E - E_g^0)}{\partial E}.\delta E_g + \dots, \qquad (1.4)$$

which gives

$$\Delta \alpha \approx -\frac{\partial \alpha(E - E_g^0)}{\partial E}.\delta E_g \qquad (1.5)$$

Since the coherent phonon intensity is obtained by taking the Fourier transform of the differential transmission, the coherent phonon intensity is thus proportional to the square of the derivative of the absorption coefficient. In fact, depending on the dimensionality of the materials, the absorption lineshapes would be different one another.

Fig. 1.11: fig/fch1-line2.eps

In Fig. 1.11, the dimensionality dependence of coherent phonon intensity is shown schematically. The top row shows the absorption coefficient as a function of photon energy. The curves are convoluted with a Lorentzian to take into account the linewidths of the transitions. The middle row shows the negative of the derivative of the absorption coefficient, which is proportional to the transient differential transmission due to coherent phonon induced band gap oscillations. The bottom row shows the square of the derivative of the absorption coefficient, which is roughly proportional to the coherent phonon intensity measured in the experiments. We note that the double-peaked structure is obtained for the 0D and 1D systems, which are symmetric and asymmetric, respectively. Based on this argument, in Chapter 5, we will discuss the lineshapes of the coherent phonon excitation profile calculated by considering the excitonic effects.

Chapter 2

Basics of carbon nanotubes and graphene

Basic physical properties of single wall carbon nanotubes (SWNTs), graphene, and also graphene nanoribbons (GNRs), are reviewed in this chapter. The discussion includes a description of the geometrical structure, electronic properties and vibrational properties properties of SWNTs and GNRs. An SWNT can be imagined as a single layer graphene sheet rolled up into a cylinder, while a GNR can be imagined as a strip of single layer graphene sheet with finite width, therefore their electronic and vibrational structures are inferred based on those of graphene. The electronic and vibrational structures are derived within the tight-binding framework and force constant model, respectively. In addition, excitonic properties of SWNTs are also discussed in this chapter.

2.1 Geometrical structure

2.1.1 Graphene unit cell

Graphene is a single atomic layer of carbon atoms in a two-dimensional (2D) honeycomb lattice. Graphene is a basic building block for all graphitic materials of other dimensionalities. Several layers of graphene sheet stacked together will form three-dimensional graphite, where the carbon atoms in each 2D layer make strong sp^2 bonds and the van der Waals forces describe a weak interlayer coupling. In 0D, graphene can be wrapped up into fullerenes (carbon cluster made up by a closed surface like a ball), and in 1D, as a main discussion in this chapter, it can be rolled up to form the nanotubes or it can be cut in one direction to make a finite width graphene called graphene nanoribbons.

Figure 2.1 gives the unit cell and Brillouin zone of graphene. The graphene sheet is generated from the dotted rhombus unit cell shown by the lattice vectors $\mathbf{a}_1$ and
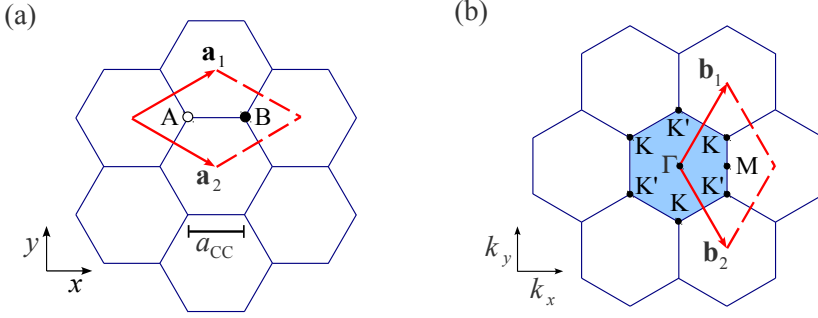
Figure 2.1 (a) The unit cell and (b) Brillouin zone of graphene are shown, respectively, as the dotted rhombus and the shaded hexagon. $\mathbf{a}_i$ and $\mathbf{b}_i$, where $i = 1, 2$, are unit vectors and reciprocal lattice vectors, respectively. The unit cell in real space contains two carbon atoms A and B. The dots labeled Γ, K, K′, and M in the Brillouin zone indicate the high-symmetry points.

$\mathbf{a}_2$, which are defined in (x, y) coordinate as

$$\mathbf{a}_1 = a \left(\frac{\sqrt{3}}{2}, \frac{1}{2} \right), \quad \mathbf{a}_2 = a \left(\frac{\sqrt{3}}{2}, -\frac{1}{2} \right), \tag{2.1}$$

where $a = \sqrt{3} a_{\mathrm{CC}}$ is the lattice constant for the graphene sheet and $a_{\mathrm{CC}} \approx 0.142 \, \mathrm{nm}$ is the nearest-neighbor interatomic distance. The unit cell consists of two distinct carbon atoms from the A and B sublattices shown, respectively, by open and solid dots in Fig. 2.1(a).

The reciprocal lattice vectors $\mathbf{b}_1$ and $\mathbf{b}_2$ are related to the real lattice vectors $\mathbf{a}_1$ and $\mathbf{a}_2$ according to the definition

$$\mathbf{a}_i \cdot \mathbf{b}_j = 2\pi \delta_{ij}, \tag{2.2}$$

where δ_{ij} is the Kronecker delta, so that $\mathbf{b}_1$ and $\mathbf{b}_2$ are given by

$$\mathbf{b}_1 = \frac{2\pi}{a} \left(\frac{1}{\sqrt{3}}, 1 \right), \quad \mathbf{b}_2 = \frac{2\pi}{a} \left(\frac{1}{\sqrt{3}}, -1 \right). \tag{2.3}$$

The first Brillouin zone is shown as a shaded hexagon in Fig. 2.1(b), where Γ (center), K , K′ (hexagonal corners), and M (center of edges) denote the high symmetry points.

2.1.2   Nanotube unit cell

Carbon nanotube forms a periodical structure or lattice, which are non-Bravais lattice. Referring to the unrolled graphene sheet shown in Fig. 2.2, the unit cell of a SWNT is limited by two vectors: the chiral vector $\mathbf{C}_h$, and the translational vector $\mathbf{T}$. The chiral

---

Fig. 2.1: fig/fch2-grunit.eps
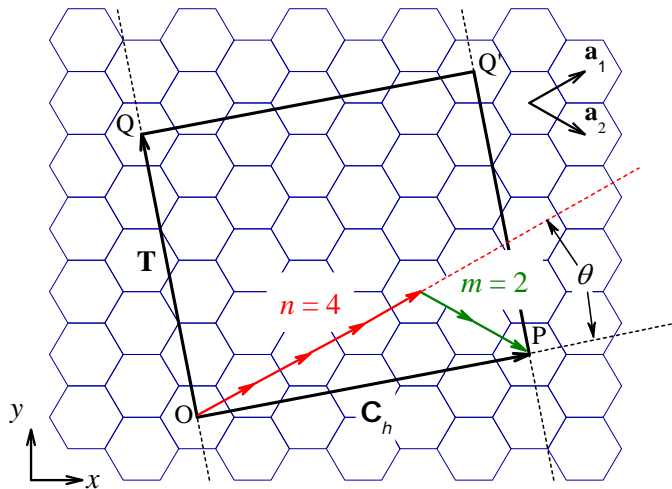
Figure 2.2 Geometry of a $(4,2)$ SWNT viewed as an unrolled graphene sheet with the graphene unit vectors $\mathbf{a}_1$ and $\mathbf{a}_2$. The rectangle OPQ'Q is the 1D SWNT unit cell. Total hexagons covered within this rectangle unit cell is $N = 28$. **OP** and **OQ** define the chiral vector $\mathbf{C}_h$ and translation vector $\mathbf{T}$, respectively, whereas the chiral angle θ is the angle between $\mathbf{a}_1$ and $\mathbf{C}_h$. From the figure, it is obvious $\mathbf{C}_h = (4,2)$ and $\mathbf{T} = (4,-5)$. If the site O is connected to P, and the site Q is connected to Q', the cylindrical SWNT can be constructed.

vector is defined as the way the graphene sheet is rolled up. It gives the circumference of a SWNT. One-dimensional periodicity in the direction of the nanotube axis is then determined by a vector perpendicular to the chiral vector, which is the translational vector $\mathbf{T}$.

The chiral vector $\mathbf{C}_h$ can be written in terms of the unit vectors of graphene $\mathbf{a}_1$ and $\mathbf{a}_2$,

$$\mathbf{C}_h = n\mathbf{a}_1 + m\mathbf{a}_2 \equiv (n, m), \tag{2.4}$$

where (n, m) is a pair of integer indices with $n \geq m$, $n > 0$, and $m \geq 0$. Since $\mathbf{C}_h$ specifies the circumference of the SWNT, it is straightforward to obtain the relations for the circumferential length L and diameter d_t:

$$L = |\mathbf{C}_h| = a\sqrt{n^2 + nm + m^2}, \tag{2.5}$$

$$d_t = \frac{L}{\pi} = \frac{a\sqrt{n^2 + nm + m^2}}{\pi}. \tag{2.6}$$

Fig. 2.2: fig/fch2-construct.eps

The chiral angle θ is the angle between $\mathbf{C}_h$ and $\mathbf{a}_1$, with values of θ in the range of $0 \leq |\theta| \leq 30°$. Taking the inner product of $\mathbf{C}_h$ and $\mathbf{a}_1$, an expresion for $\cos \theta$ can be obtained, thus relating θ to the chiral index (n, m),

$$\cos \theta = \frac{\mathbf{C}_h \cdot \mathbf{a}_1}{|\mathbf{C}_h||\mathbf{a}_1|} = \frac{2n + m}{2\sqrt{n^2 + nm + m^2}}. \tag{2.7}$$

As can be seen in Fig. 2.2, the translation vector $\mathbf{T}$ is perpendicular to $\mathbf{C}_h$ and thus become the tube axis, it can be expressed as

$$\mathbf{T} = t_1 \mathbf{a}_1 + t_2 \mathbf{a}_2 \equiv (t_1, t_2), \tag{2.8}$$

where t_1 and t_2 are obtained from the condition $\mathbf{C}_h \cdot \mathbf{T} = 0$,

$$t_1 \frac{2m + n}{d_R}; \quad t_2 = -\frac{2n + m}{d_R}. \tag{2.9}$$

$$\tag{2.10}$$

Here d_R is the greatest common divisor (gcd) of $(2m + n)$ and $(2n + m)$ so that $\gcd(t_1, t_2) = 1$. The length of the translation vector, T, is then given by

$$T = |\mathbf{T}| = \sqrt{3}L/d_R. \tag{2.11}$$

The unit cell of a SWNT is defined as the area covered by $\mathbf{C}_h$ and $\mathbf{T}$. The area is given by the magnitude of the vector product of $\mathbf{C}_h$ and $\mathbf{T}$. The number of hexagons per unit cell of the SWNT, N_{hex}, is obtained by dividing the area of the SWNT unit cell with the area of the hexagonal unit cell in the graphene sheet:

$$N_{\text{hex}} = \frac{|\mathbf{C}_h \times \mathbf{T}|}{\mathbf{a}_1 \times \mathbf{a}_2} = \frac{2(n^2 + nm + m^2)}{d_R}. \tag{2.12}$$

All the basic structural parameters of the SWNT are shown in Fig. 2.2. The SWNT can then be classified according to its (n, m) or θ value (see Fig. 2.3). This classification is based on the symmetry of the SWNT. There are three types of carbon nanotubes: (a) zigzag, (b) chiral, and (c) armchair nanotubes, as shown in Fig. 2.3. Chiral SWNTs exhibit a spiral symmetry whose mirror image cannot be superposed onto the original one. Zigzag and armchair SWNTs have mirror images that are identically the same as the original ones when we put a nanotube axis in the mirror. The names of of armchair and zigzag arise from the shape of the cross-sectional ring in the circumferential direction of the SWNTs. We then have various SWNT geometries that can change diameter, chirality, and also cap structures, giving rich physical properties of carbon nanotubes.

While the 1D unit cell of a SWNT in real space is expressed by $\mathbf{C}_h$ and $\mathbf{T}$, the corresponding vectors in reciprocal space are the vectors $\mathbf{K}_1$ along the tube circumference and $\mathbf{K}_2$ along the tube axis. Since nanotubes are 1D materials, only $\mathbf{K}_2$ is a
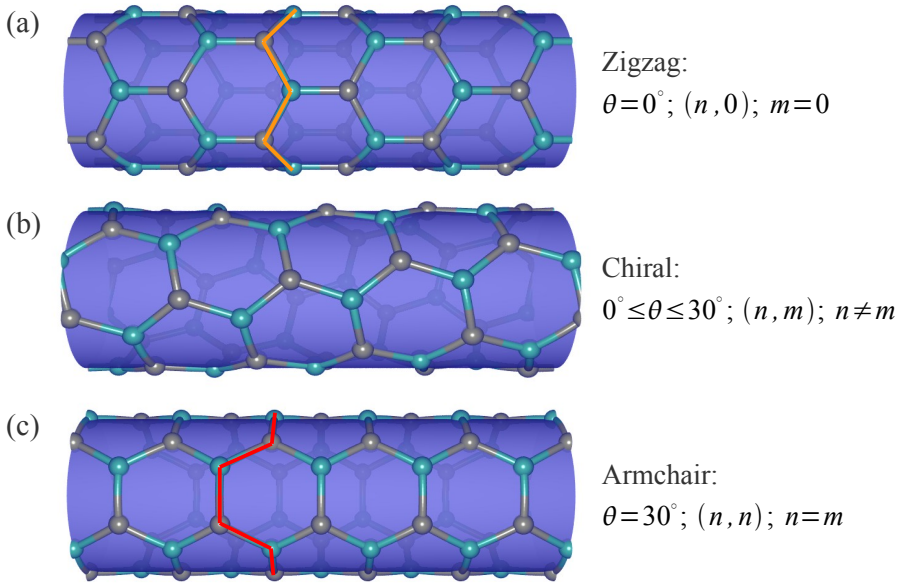
Figure 2.3 Classification of carbon nanotubes: (a) zigzag, (b) chiral, (c) armchair SWNTs. From left to right, the chiral index of each SWNT above is $(5,0)$, $(4,2)$, $(3,3)$, respectively. In (a) and (c), thick solid lines are to emphasize "zigzag" and "armchair" structures, respectively.

reciprocal lattice vector. $\mathbf{K}_1$ gives discrete k values in the direction of $\mathbf{C}_h$. Expressions for $\mathbf{K}_1$ and $\mathbf{K}_2$ are obtained from their relations with $\mathbf{C}_h$ and $\mathbf{T}$:

$$\mathbf{C}_h \cdot \mathbf{K}_1 = 2\pi, \quad \mathbf{T} \cdot \mathbf{K}_1 = 0, \tag{2.13}$$

$$\mathbf{C}_h \cdot \mathbf{K}_2 = 0, \quad \mathbf{T} \cdot \mathbf{K}_2 = 2\pi. \tag{2.14}$$

It follows,

$$\mathbf{K}_1 = \frac{1}{N_{\mathrm{hex}}}(-t_2\mathbf{b}_1 + t_1\mathbf{b}_2), \mathbf{K}_2 = \frac{1}{N_{\mathrm{hex}}}(m\mathbf{b}_1 - n\mathbf{b}_2), \tag{2.15}$$

where $\mathbf{b}_1$ and $\mathbf{b}_2$ are the reciprocal lattice vectors of graphene. In Fig. 2.4, $\mathbf{K}_1$ and $\mathbf{K}_2$ are shown for the $(4,2)$ SWNT. The N_{hex} line segments with length of $\mathbf{K}_2$ construct the 1D Brillouin zone of the SWNT, which we call as "cutting lines".

The allowed wave vector $\mathbf{k}$ of a SWNT is

$$\mathbf{k} = \mu\mathbf{K}_1 + k\frac{\mathbf{K}_2}{|\mathbf{K}_2|} \tag{2.16}$$

where $\mu = 0, 1, \ldots, N_{\mathrm{hex}} - 1$ is the "cutting line" index, and k is in the range of $-\pi/T < k < \pi/T$. The length of $\mathbf{K}_1$ and $\mathbf{K}_2$ are given by:

$$|\mathbf{K}_1| = \frac{2\pi}{L} = \frac{2}{d_t}, \quad |\mathbf{K}_2| = \frac{2\pi}{T}. \tag{2.17}$$

Fig. 2.3: fig/fch2-swnt.eps
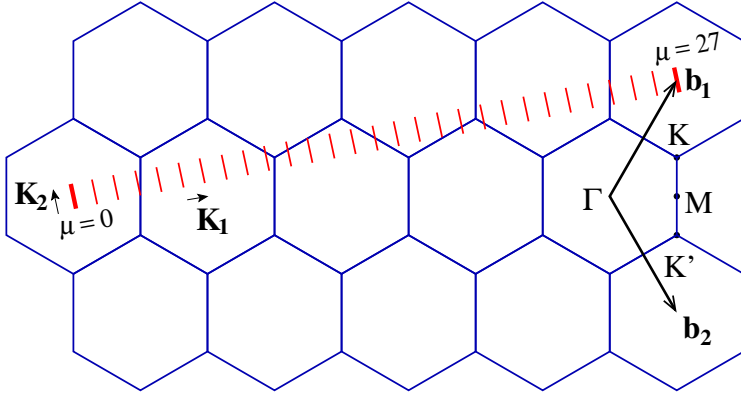
Figure 2.4 The reciprocal lattice vectors $\mathbf{K}_1$ and $\mathbf{K}_2$, and the Brillouin zone of a $(4, 2)$ SWNT represented by the set of $N = 28$ parallel cutting lines. The vectors $\mathbf{K}_1$ and $\mathbf{K}_2$ in reciprocal space correspond to $\mathbf{C}_h$ and $\mathbf{T}$ in real space, respectively. The cutting lines are labeled by the integer angular momentum index μ.

The unit cell of the SWNT contains N_{hex} hexagons, then the first Brillouin zone of the SWNT consists of N_{hex} cutting lines. Therefore, N_{hex} parallel cutting lines are related to the discrete value of the angular momentum μ, and the cutting line length $\mathbf{K}_2$ determines the periodicity of the 1D momentum k.

2.1.3   Nanoribbon unit cell

A single layer graphene nanoribbon (GNR) can be imagined as a strip of single layer graphene sheet with finite ultrathin width. Since we confine the graphene sheet in one direction, GNRs can also be considered as 1D materials. Depending on the position where we cut the graphene sheet, we may have two specific GNR structures: armchair GNRs and zigzag GNRs, as shown in Fig. 2.5.

Armchair ribbons and zigzag ribbons are denoted by N_{ab} aGNR and N_{ab} zGNR, respectively, where N_{ab} is the number of AB carbon dimers in the translational unit cell. In zigzag ribbons, the length L of the translational unit cell is a and the width W of the ribbon is $(N_{ab} - 1)\frac{\sqrt{3}}{2}a$ where $a = 2.49$ is the hexagonal lattice constant in graphene. In armchair ribbons, the translational unit cell length is $\sqrt{3}a$ and the ribbon width is $(N_{ab} - 1)\frac{1}{2}a$. Note that in zigzag and armchair ribbons with the same number of atoms per unit cell, the area of the unit cells are equal. The k-space properties of GNRs can be then be derived similarly as those of SWNTs [36, 37], in which we will also have 1D Brillouin zone in terms of the cutting lines μ depending on the GNR structure.

Fig. 2.4: fig/fch2-bz.eps
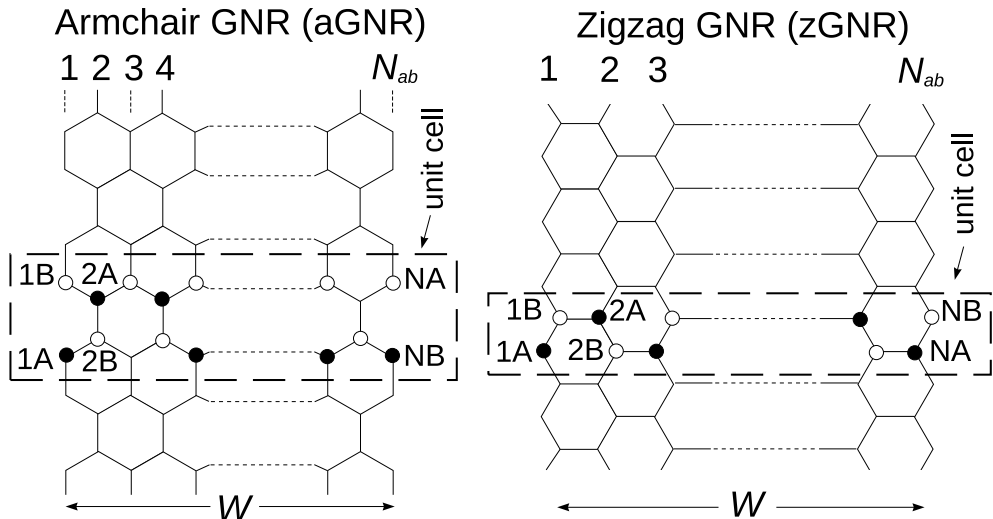
Figure 2.5 Lattice structures and translational unit cells for armchair (aGNR) and zigzag (zGNR) graphene nanoribbons. The width of the nanoribbons is W.

2.2   Electronic properties

The electronic dispersion relations of SWNTs are derived from those of a graphene sheet. The tight-binding model is reviewed here, starting from a simple tight-binding (STB) model. In a later section, the extended tight-binding (ETB) model that gives a good agreement with some optical spectroscopy measurements are described.

The electronic dispersion relations of a graphene sheet are obtained by solving the single particle Schrödinger equation:

$$H\Psi^b(\mathbf{k},\mathbf{r}) = E\Psi^b(\mathbf{k},\mathbf{r}),\qquad(2.18)$$

where $H = T + V(\mathbf{r})$ is the single-particle Hamiltonian, T is the kinetic energy operator, $V(\mathbf{r})$ is the periodic potential, $\Psi^b(\mathbf{k},\mathbf{r})$ is the one-electron wavefunction, b is the band index, $\mathbf{k}$ is the electron wavevector, $\mathbf{r}$ is the spatial coordinate, and E is the energy eigenvalue. The electron wavefunction $\Psi^b(\mathbf{k},\mathbf{r},t)$ is approximated by a linear combination of atomic orbitals (LCAO) in terms of Bloch functions:

$$\Psi^b(\mathbf{k},\mathbf{r},t) = \exp\left(-iE^b(\mathbf{k})t/\hbar\right)\sum_{so}C_{so}^b(\mathbf{k})\Phi_{so}(\mathbf{k},\mathbf{r}),$$

$$\Phi_{so}(\mathbf{k},\mathbf{r}) = \frac{1}{\sqrt{N_u}}\sum_{u}^{N_u}\exp\left(i\mathbf{k}\mathbf{R}_{us}\right)\phi_o(\mathbf{r}-\mathbf{R}_{us}),\qquad(2.19)$$

where $E^b(\mathbf{k})$ is the one-electron energy, $C_{so}^b(\mathbf{k})$ is the Bloch amplitude, $\Phi_{so}(\mathbf{k},\mathbf{r})$ is the Bloch wavefunction, $\phi_o(\mathbf{r})$ is the atomic orbital, $\mathbf{R}_{us}$ is the atomic coordinate, the

Fig. 2.5: fig/fch2-ribbonstruct.eps

index $u = 1, \ldots, N_u$ is for all the N_u unit cells in a graphene sheet ($N_u = N_{\text{hex}}$ for a SWNT and $N_u = N_{\text{ab}}$ for a GNR), the index $s = A, B$ labels the two inequivalent atoms in the unit cell, and the index $o = 1s, 2s, 2p_x, 2p_y, 2p_z$ gives the atomic orbitals of a carbon atom.

The Schrödinger equation for the Bloch amplitudes $C_{so}^b(\mathbf{k})$ can be written in the matrix form:

$$\sum_{so} H_{s'o'so}(\mathbf{k}) C_{so}^b(\mathbf{k}) = \sum_{so} E^b(\mathbf{k}) S_{s'o'so}(\mathbf{k}) C_{so}^b(\mathbf{k}) \,, \tag{2.20}$$

where the Hamiltonian $H_{s'o'so}(\mathbf{k})$ and overlap $S_{s'o'so}(\mathbf{k})$ matrices are given by:

$$H_{s'o'so}(\mathbf{k}) = \sum_{u}^{U} \exp\left(i\mathbf{k}\left(\mathbf{R}_{us} - \mathbf{R}_{u's'}\right)\right) \int \phi_{o'}^*(\mathbf{r} - \mathbf{R}_{u's'}) H \phi_o(\mathbf{r} - \mathbf{R}_{us}) d\mathbf{r} \,,$$

$$\tag{2.21}$$

$$S_{s'o'so}(\mathbf{k}) = \sum_{u}^{U} \exp\left(i\mathbf{k}\left(\mathbf{R}_{us} - \mathbf{R}_{u's'}\right)\right) \int \phi_{o'}^*(\mathbf{r} - \mathbf{R}_{u's'}) \phi_o(\mathbf{r} - \mathbf{R}_{us}) d\mathbf{r} \,,$$

and the index u' labels the unit cell under consideration. The orthonormality condition for the electron wavefunction of Eq. (2.19) becomes:

$$\int \Psi^{b'\,*}(\mathbf{k}, \mathbf{r}, t) \Psi^b(\mathbf{k}, \mathbf{r}, t) d\mathbf{r} = \sum_{s'o'} \sum_{so} C_{s'o'}^{b'\,*}(\mathbf{k}) S_{s'o'so}(\mathbf{k}) C_{so}^b(\mathbf{k}) = \delta_{b'b} \,. \tag{2.22}$$

To evaluate the integrals in Eq. (2.21), the periodic potential $V(\mathbf{r})$ in the single particle Hamiltonian H of Eq. (2.18) is expressed by a sum of the spherically-symmetric potentials $U(\mathbf{r} - \mathbf{R}_{u''s''})$ centered at the atomic sites $\mathbf{R}_{u''s''}$:

$$V(\mathbf{r}) = \sum_{u''s''} U(\mathbf{r} - \mathbf{R}_{u''s''}) \,. \tag{2.23}$$

The Hamiltonian matrix $H_{s'o'so}(\mathbf{k})$ then contains the three-center integrals that involve two orbitals $\phi_{o'}^*(\mathbf{r} - \mathbf{R}_{u's'})$ and $\phi_o(\mathbf{r} - \mathbf{R}_{us})$ at two different atomic sites $\mathbf{R}_{u's'}$ and $\mathbf{R}_{us}$, while the potential $U(\mathbf{r} - \mathbf{R}_{u''s''})$ originates from a third atomic site $\mathbf{R}_{u''s''}$. On the other hand, the overlap matrix $S_{s'o'so}(\mathbf{k})$ contains two-center integrals only. Neglecting the three-center integrals in $H_{s'o'so}(\mathbf{k})$, the remaining two-center integrals in both $H_{s'o'so}(\mathbf{k})$ and $S_{s'o'so}(\mathbf{k})$ can be parameterized as functions of the interatomic vector $\mathbf{R} = \mathbf{R}_{us} - \mathbf{R}_{u's'}$ and of the symmetry and relative orientation of the atomic orbitals $\phi_{o'}^*(\mathbf{r})$ and $\phi_o(\mathbf{r})$:

$$\varepsilon_o = \int \phi_o^*(\mathbf{r}) H \phi_o(\mathbf{r}) d\mathbf{r} \,,$$

$$t_{o'o}(\mathbf{R}) = \int \phi_{o'}^*(\mathbf{r}) \left(T + U(\mathbf{r}) + U(\mathbf{r} - \mathbf{R})\right) \phi_o(\mathbf{r} - \mathbf{R}) d\mathbf{r} \,, \tag{2.24}$$

$$s_{o'o}(\mathbf{R}) = \int \phi_{o'}^*(\mathbf{r}) \phi_o(\mathbf{r} - \mathbf{R}) d\mathbf{r} \,,$$

where ε_o is the atomic orbital energy, $t_{o'o}(\mathbf{R})$ is the transfer integral, and $s_{o'o}(\mathbf{R})$ is the overlap integral. A numerical calculation of parameters ε_o, $t_{o'o}(\mathbf{R})$, and $s_{o'o}(\mathbf{R})$ defines the non-orthogonal tight-binding model. Within the orthogonal tight-binding model, $s_{o'o}(\mathbf{R})$ is set to zero (unity) for $\mathbf{R} \neq 0$ ($\mathbf{R} = 0$).

2.2.1 Graphene electronic structure

In the STB model, we neglect the σ bonding of C-C atoms and the long-range atomic interactions in the π bonding for $R > a_{\mathrm{CC}}$. The STB model thus has three parameters: the atomic orbital energy ε_{2p}, the transfer integral $t_{\pi\pi}(a_{\mathrm{CC}})$, and the overlap integral $s_{\pi\pi}(a_{\mathrm{CC}})$. The transfer and overlap integrals will simply be referred to as t, and s, respectively.

To construct the Hamiltonian $H_{s'o'so}(\mathbf{k})$ and overlap $S_{s'o'so}(\mathbf{k})$ matrices of Eq. (2.20), consider the nearest-neighbor interactions ($R = a_{\mathrm{CC}}$) in the unit cell of a graphene sheet. The unit cell contains two atoms, A and B, each of which has three nearest neighbors of the opposite atom type (A and B). The absence of nearest-neighbor interactions within the same A or B sublattice gives the diagonal Hamiltonian and overlap matrix elements, $H_{\mathrm{A}\pi\mathrm{A}\pi} = H_{\mathrm{B}\pi\mathrm{B}\pi} = \varepsilon_{2p}$ and $S_{\mathrm{A}\pi\mathrm{A}\pi} = S_{\mathrm{B}\pi\mathrm{B}\pi} = 1$, independent of the transfer t and overlap s integrals. For the $H_{\mathrm{A}\pi\mathrm{B}\pi}$ and $S_{\mathrm{A}\pi\mathrm{B}\pi}$ matrix elements, the interatomic vectors $\mathbf{R}$ from atom A to its three nearest-neighbors in Eq. (2.20) are given by $(\mathbf{a}_1 + \mathbf{a}_2)/3$, $(\mathbf{a}_1 - 2\mathbf{a}_2)/3$, and $(\mathbf{a}_2 - 2\mathbf{a}_1)/3$. Substituting these vectors into Eq. (2.20), one can obtain $H_{\mathrm{A}\pi\mathrm{B}\pi} = tf(\mathbf{k})$ and $S_{\mathrm{A}\pi\mathrm{B}\pi} = sf(\mathbf{k})$, where $f(\mathbf{k})$ is the sum of the phase factors over the nearest neighbors given by

$$f(\mathbf{k}) = \exp\left(i\frac{k_x a}{\sqrt{3}}\right) + \exp\left(-i\frac{k_x a}{2\sqrt{3}} + i\frac{k_y a}{2}\right) + \exp\left(-i\frac{k_x a}{2\sqrt{3}} - i\frac{k_y a}{2}\right). \qquad (2.25)$$

The $H_{\mathrm{B}\pi\mathrm{A}\pi}$ and $S_{\mathrm{B}\pi\mathrm{A}\pi}$ matrix elements are derived in a similar way. The interatomic vectors $\mathbf{R}$ have the opposite signs, giving $H_{\mathrm{B}\pi\mathrm{A}\pi} = tf^*(\mathbf{k})$ and $S_{\mathrm{B}\pi\mathrm{A}\pi} = sf^*(\mathbf{k})$. The Schrödinger equation in the matrix form, Eq. (2.20), can be written as

$$\begin{pmatrix} \varepsilon_{2p} & tf(\mathbf{k}) \\ tf^*(\mathbf{k}) & \varepsilon_{2p} \end{pmatrix} \begin{pmatrix} C_{\mathrm{A}\pi}^b(\mathbf{k}) \\ C_{\mathrm{B}\pi}^b(\mathbf{k}) \end{pmatrix} = E^b(\mathbf{k}) \begin{pmatrix} 1 & sf(\mathbf{k}) \\ sf^*(\mathbf{k}) & 1 \end{pmatrix} \begin{pmatrix} C_{\mathrm{A}\pi}^b(\mathbf{k}) \\ C_{\mathrm{B}\pi}^b(\mathbf{k}) \end{pmatrix}. \qquad (2.26)$$

Solving this secular equation yields the energy eigenvalues:

$$E^v(\mathbf{k}) = \frac{\varepsilon_{2p} + tw(\mathbf{k})}{1 + sw(\mathbf{k})}, \quad E^c(\mathbf{k}) = \frac{\varepsilon_{2p} - tw(\mathbf{k})}{1 - sw(\mathbf{k})}, \qquad (2.27)$$

where the band index $b = \mathrm{v, c}$ indicates the valence and conduction bands, $t < 0$, and $w(\mathbf{k})$ is the absolute value of the phase factor $f(\mathbf{k})$, i.e., $w(\mathbf{k}) = \sqrt{f^*(\mathbf{k})f(\mathbf{k})}$:

$$w(\mathbf{k}) = \sqrt{1 + 4\cos\frac{\sqrt{3}k_x a}{2}\cos\frac{k_y a}{2} + 4\cos^2\frac{k_y a}{2}}. \qquad (2.28)$$
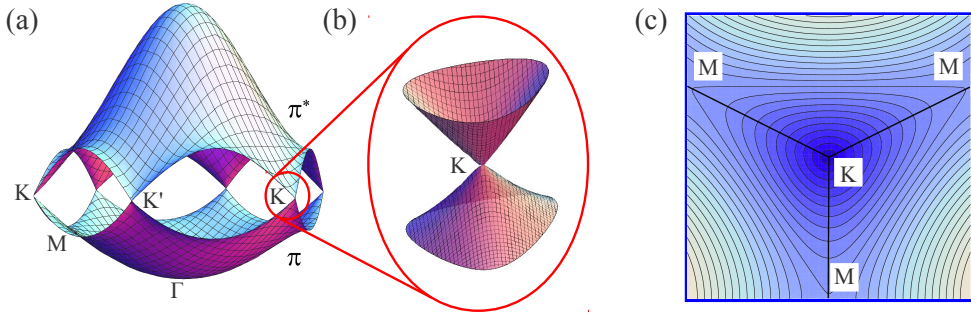
Figure 2.6 The π bands of graphene within the simple tight-binding method. In (a), the energy dispersion is shown throughout the whole region of the Brillouin zone. (b) Near the K point, the energy dispersion relation is approximately linear, showing two symmetric cone shapes, the so-called Dirac cones. (c) Contour plot of the energy dispersion near the K point. The tight-binding parameters used here are $\epsilon_{2p} = 0\,\text{eV}$, $t = -3.033\,\text{eV}$, and $s = 0.129$.

According to Eq. (2.27), the atomic orbital energy ε_{2p} is an arbitrary reference point in the orthogonal STB model ($s = 0$), while ε_{2p} is a relevant parameter in the non-orthogonal ETB model ($s \neq 0$).

Fitting the dispersion relations of the graphene sheet given by Eq. (2.27) to the energy values obtained from an *ab initio* calculation gives the values of the transfer integral $t = -3.033\,\text{eV}$ and overlap integral $s = 0.129$, and set the atomic orbital energy equal to zero (origin of the energy scale), $\varepsilon_{2p} = 0\,\text{eV}$ [1]. Fig. 2.6 (a) shows the dispersion relations of the graphene sheet given by Eq. (2.27) with the above parameters throughout the entire area of the first Brillouin zone. The lower (valence) band is completely filled with electrons in the ground state, while the upper (conduction) band is completely empty of electrons in the ground state.

Unlike most semiconductors, the band structure of a graphene sheet shows linear dispersion relations around the K and K′ points near the Fermi level, as can be seen in Fig. 2.6(b). The electron wavevector around the K point in the first Brillouin zone can be written in the form $k_x = \Delta k_x$ and $k_y = -4\pi/(3a) + \Delta k_y$, where Δk_x and Δk_y are small compared to $1/a$. Substituting this wavevector into Eq. (2.28) and making the expansion in a power series in $\Delta k_x a$ and $\Delta k_y a$ up to the second order, one can obtain $w = \frac{\sqrt{3}}{2}\Delta k a$, where $\Delta k = \sqrt{\Delta k_x^2 + \Delta k_y^2}$ is the distance from the electron wavevector to the K point. Substituting w into Eq. (2.27) gives the electronic dispersion relations in the valence and conduction bands:

$$E^v\left(\Delta k\right) = \varepsilon_{2p} - \frac{\sqrt{3}}{2}\left(\varepsilon_{2p}s - t\right)a\,\Delta k\,, \quad E^c\left(\Delta k\right) = \varepsilon_{2p} + \frac{\sqrt{3}}{2}\left(\varepsilon_{2p}s - t\right)a\,\Delta k\,, \quad (2.29)$$

which are linear in Δk. The linear dispersion relations near the Fermi level suggest that the non-relativistic Schrödinger equation used for conventional semiconductors with

---

Fig. 2.6: fig/fch2-piband.eps
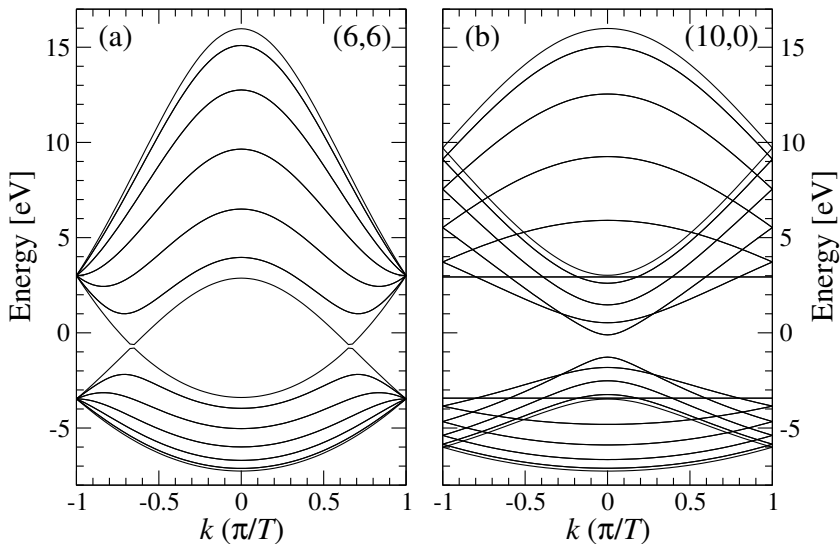
Figure 2.7 Examples of 1D energy dispersion relations of SWNTs: (a) armchair $(6,6)$, and (b) zigzag $(10,0)$ SWNTs. No bandgaps can be seen in (a), thus the SWNT is metallic, whereas the SWNT in (b) is semiconducting because there is an open gap.

parabolic energy bands is not sufficient to explain the electrons in a graphene sheet. Instead, the π electrons in a graphene sheet mimic massless particles whose behavior is described by the relativistic Dirac equation. Furthermore, the linear dispersion relations increase the mobility of the π electrons in a graphene sheet compared to that of conventional semiconductors. In contrast to the π electrons, the σ electrons fully occupy the energy band, and therefore do not contribute to the transport properties. Indeed, the σ energy bands lie several eV away from the Fermi level, as obtained by solving Eq. (2.20) for the σ molecular orbitals. In Fig. 2.6(c), the contour plot of the energy dispersion near the K point is shown. The energy surface changes from circle to triangle with increasing distance from the K point, giving rise to the so-called trigonal warping effect [26], which strongly affects the optical transitions in SWNTs.

2.2.2 Nanotube electronic structure

Now the electronic structure of a SWNT can be derived from the energy dispersion calculation of graphene in Eq. (2.27). As we discussed in Sec. 2.1.2, the allowed wave vectors $\mathbf{k}$ (the cutting lines) around the SWNT circumference become quantized. The energy dispersion relations of the SWNT are then given by the corresponding energy dispersion relations of graphene along the cutting lines. When the 1D cutting lines $\mu\mathbf{K}_1 + k\mathbf{K}_2/|\mathbf{K}_2|$ of a SWNT in Eq. (2.16) are superimposed on the 2D electronic energy dispersion surface of the graphene sheet in Eq. (2.27), N pairs of energy dispersion
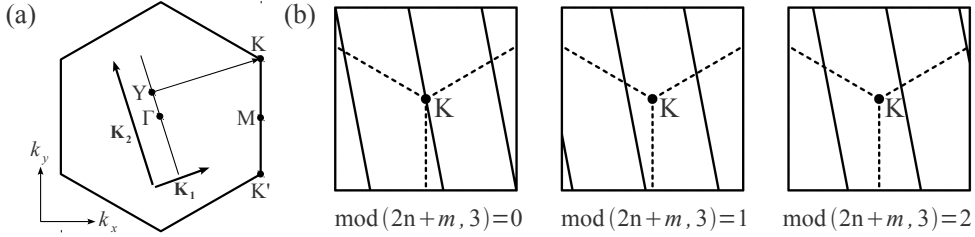
Figure 2.8 (a) Condition for metallic energy bands is related to the ratio of the length of vector $\mathbf{YK}$ to that of $\mathbf{K}_1$. If the ratio is an integer, metallic energy bands are obtained [1]. (b) Three possible configurations of the cutting lines in the vicinity of the K point depending on the value of $\mathrm{mod}(2n+m,3)$. From left to right, the nanotube type is M- (metallic), S1- (type-I semiconducting), and S2- (type-II semiconducting) SWNT, respectively. The solid lines represent the cutting lines and the dashed lines indicate the KM directions, which are the boundaries of the first Brillouin zone of the SWNT.

relations of the SWNT, $E^b_{\mathrm{SWNT}}(\mu, k)$, are obtained:

$$E^b_{\mathrm{SWNT}}(\mu, k) = E^b_{\mathrm{2D}}\left(\mu \mathbf{K}_1 + k\frac{\mathbf{K}_2}{|\mathbf{K}_2|}\right), \quad \left(\mu = 0, 1, \ldots, N-1; -\frac{\pi}{T} < k < \frac{\pi}{T}\right).$$
(2.30)

For a particular (n, m) SWNT, if a cutting line passes through K or K′ point of the Brillouin zone of graphene, where the valence and conduction bands touch to each other, the 1D energy bands of the SWNT have a zero energy gap, therefore, they become metallic. However, if a cutting line does not pass through K or K′, the (n, m) is semiconducting with a finite energy gap. Figure 2.7 gives two examples of the SWNT dispersion relations.

As shown in Fig. 2.8(a), if we project the $\mathbf{\Gamma K}$ vector pointing toward the K point onto the $\mathbf{K}_1$ direction perpendicular to the cutting lines, that can be denoted by $\mathbf{\Gamma Y} = \mathbf{\Gamma K} \cdot \mathbf{K}_1/\sqrt{\mathbf{K}_1 \cdot \mathbf{K}_1}$, we can find:

$$\frac{\mathbf{\Gamma K}}{\sqrt{\mathbf{K}_1 \cdot \mathbf{K}_1}} = \frac{\frac{1}{3}(2\mathbf{b}_1 + \mathbf{b}_2) \cdot \frac{1}{N}(t_1\mathbf{b}_2 - t_2\mathbf{b}_1)}{\sqrt{\frac{1}{N}(t_1\mathbf{b}_2 - t_2\mathbf{b}_1) \cdot \frac{1}{N}(t_1\mathbf{b}_2 - t_2\mathbf{b}_1)}}$$
(2.31)

$$= \frac{2n + m}{3},$$
(2.32)

If $(2n + m)/3$ is an integer, $\mathbf{\Gamma K}$ has an integer number of $\mathbf{K}_1$ components, so that one of the cutting lines passes through the K point, hence giving a metallic SWNT. If $(2n + m)/3$ is not an integer, i.e, the residual is 1 or 2, the K point lies at 1/3 or 2/3 of the spacing between two adjacent cutting lines near the K point, hence giving a semiconducting SWNT, as shown in Fig. 2.8(b). These three types of SWNTs are referred to as M-, S1-, and S2-SWNTs, respectively:

Fig. 2.8: fig/fch2-class.eps
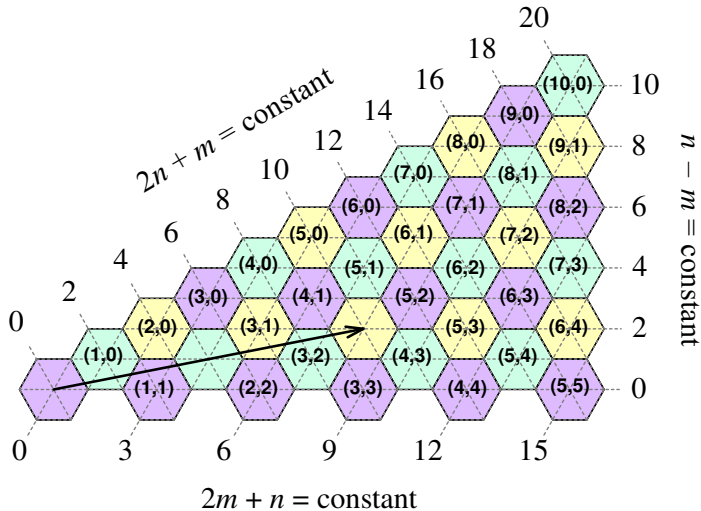
Figure 2.9 Nanotubes family classification on the unrolled graphene sheet for the nanotubes of diameter less than 1 nm. The (n, m) indices written in the hexagons represent the chiral vectors pointing to the centers of the hexagons. Here the chiral vector of a $(4, 2)$ SWNT is shown by an arrow. The dashed lines represent the families of constant $2n + m$, $n - m$, and $2m + n$ for each family. The magenta, light yellow, and cyan hexagons correspond to the chiral vectors of M-, S1-, and S2-SWNTs, respectively.

$$\text{M} \quad : \quad \text{mod}(2n + m, 3) = 0, \tag{2.33}$$

$$\text{S1} \quad : \quad \text{mod}(2n + m, 3) = 1, \tag{2.34}$$

$$\text{S2} \quad : \quad \text{mod}(2n + m, 3) = 2. \tag{2.35}$$

The S1- and S2-SWNTs are often written as type-I and type-II semiconducting SWNTs. There are also other metallicity notations frequently used in the nanotube research community depending on the value of $\text{mod}(n - m, 3)$ as follows:

$$\text{mod}\,0 \quad : \quad \text{mod}(n - m, 3) = 0, \tag{2.36}$$

$$\text{mod}\,1 \quad : \quad \text{mod}(n - m, 3) = 1, \tag{2.37}$$

$$\text{mod}\,2 \quad : \quad \text{mod}(n - m, 3) = 2. \tag{2.38}$$

With a simple algebra, it can be shown that $\text{mod}\,0$, $\text{mod}\,1$, and $\text{mod}\,2$ SWNTs are the same as M-, S2-, S1-SWNTs, respectively.

In Fig. 2.9, the chiral vectors for M-, S1-, and S2-SWNTs are shown. Within the triangular graphene sheet, the diagonal lines of each hexagon are connected to the diagonal lines of the adjacent hexagons, shown by the dashed lines in Fig. 2.9. These

---

Fig. 2.9: fig/fch2-famnum.eps
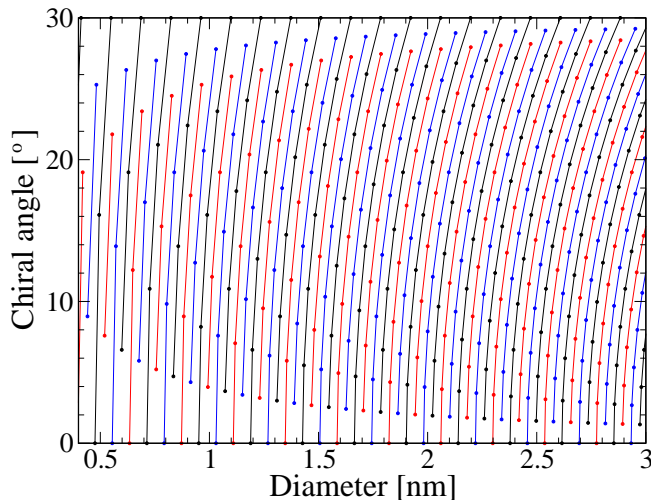
Figure 2.10   Chiral angle (θ) versus diameter (d_t) of all SWNTs in the range of $0.5 < d_t < 3$ nm. Nanotubes of the same family number ($2n + m$) are connected by lines. Up to $d_t \approx 1.2$ nm, the constant $2n + m$ nanotubes have similar diameters.

lines with constant values of ($2n + m$), ($2m + n$), and ($n - m$) are called the family lines. Especially for the ($2n + m$) families, the SWNTs which belong to the same ($2n + m$) have the closest diameters, compared to the ($2m + n$) or ($n - m$) families, as obviously can be seen in Fig. 2.10.

2.2.3   Density of states and transition energies

The electronic density of states (DOS) or the number of available electronic states for a given energy interval per carbon atom is especially very important for understanding optical properties of materials. The DOS is known to depend on the dimension of the materials. For parabolic energy bands found in most semiconductors, the DOS rises as the square root of the energy above the energy bottom E_0 in the 3D cases such as diamond and graphite, $g(E) \propto (E - E_0)^{1/2}$. For a 1D system such as SWNT, E_0 is equal to the subband edge energy E_i^b, where the DOS magnitude becomes singular, known as the van-Hove singularity (VHS).

The presence of VHSs in the DOS of SWNTs has a great impact on their optical properties, a significant enhancement in the SWNT response is observed when the excitation energy for the probe matches one of the VHSs in the DOS in the valence and conduction bands of the SWNT. For example, optical absorption is strongly enhanced when the photon energy is in resonance with the allowed transition between two VHSs in the valence and conduction bands. This enhancement is generally interpreted in terms of the joint density of electronic states (JDOS) which takes into
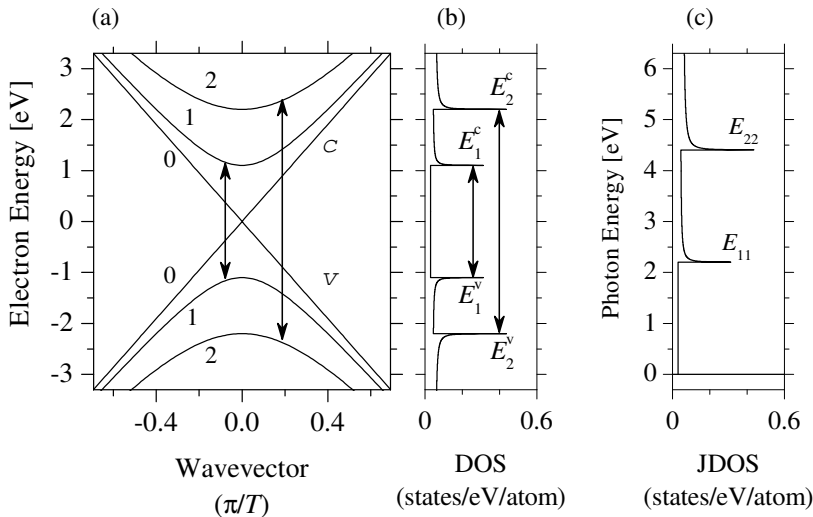
Figure 2.11 (a) The dispersion relations and (b) density of electronic states DOS of the $(15, 0)$ SWNT. The arrows show the allowed optical transitions between the first and second valence and conduction subbands. (c) The joint density of states (JDOS) of the $(15, 0)$ SWNT. The labels E_{11} (E_{22}) correspond to the transition between E_1^v and E_1^c (E_2^v and E_2^c) shown in panel (b). Reproduced from Ref. [38].

account the dipole selection rules. The optical transitions should conserve both angular and linear momenta in SWNTs, thus the transitions are vertical in k-space, as shown in Fig. 2.11(a).

The optical response of SWNTs is dominated by the VHSs in the JDOS labeled by E_{ii}. The optical transition energies E_{ii} for $i = 1, 2, 3, \ldots$ and for all the possible (n, m) SWNTs are summarized in the so-called Kataura plot [39] as a function of the SWNT diameter d_t. In Fig. 2.12(a), the Kataura plot calculated within the STB model is shown, in which the transition energies are interpreted as the energy gaps between i-th VHSs in the conduction and valence bands. The same STB Kataura plot is shown in Fig. 2.12 (b) as a function of the inverse SWNT diameter $1/d_t$, which is more convenient for direct comparison with experiments, since $1/d_t$ is proportional to ω_{RBM}. Furthermore, the $1/d_t$ scale allows us to explore the small d_t region ($d_t < 1.2\,\mathrm{nm}$), which has a lower density of (n, m) indices. As one can see from Fig. 2.12, the E_{ii} energies for M-, S1-, and S2-SWNTs show distinct behavior. Within the M-, S1-, and S2-types, the E_{ii} energies that belong to the families of constant $2n+m$ group together in the Kataura plot.
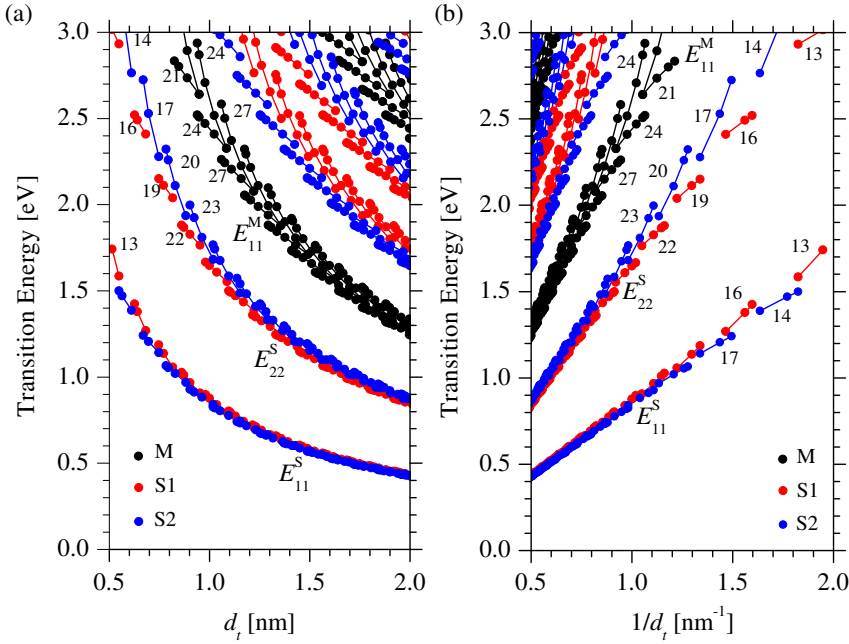
Figure 2.12 The optical transition energies E_{ii} for $i = 1, 2, 3, \ldots$ and for all possible (n, m) SWNTs in the range of $0.5 < d_t < 2.0$ nm calculated within the STB model as a function of (a) SWNT diameter d_t, and (b) inverse diameter $1/d_t$, known as the Kataura plot. Black, red, and blue dots correspond to M-, S1-, and S2 SWNTs, respectively. The constant $2n + m$ families are connected by lines. Reproduced from Ref. [38].

2.2.4   Extended tight-binding model

Recent E_{ii} measurements by photoluminiscence (PL) and resonance Raman spectroscopy (RRS) indicate that the STB calculation is not sufficient to interpret the experimental results. Figures 2.13 and 2.14 give the same E_{ii} energies for the same SWNT sample, that is HiPco SWNTs suspended by SDS surfactant in aqueous solution. The experimental Kataura plots in Figs. 2.13(b) and 2.14(b) differ from the theoretical STB Kataura plot in Fig. 2.12 two aspects: in the large diameter limit and in the small diameter limit. In the large d_t limit the ratio of E_{22}^S to E_{11}^S reaches 1.8 in the experimental Kataura plots, while the same ratio goes to 2 in the theoretical STB Kataura plot [40], which is called as the ratio problem. This problem can be understood by means of the many-body interactions related to the excitons, that will be discussed in Sec. 2.4. In the small d_t limit, the families of constant $2n + m$ deviate from the mean E_{ii} energy bands in the experimental Kataura plots, while the family spread in the theoretical Kataura plot remains relatively moderate [25].

Fig. 2.12: fig/fch2-stbkat.eps
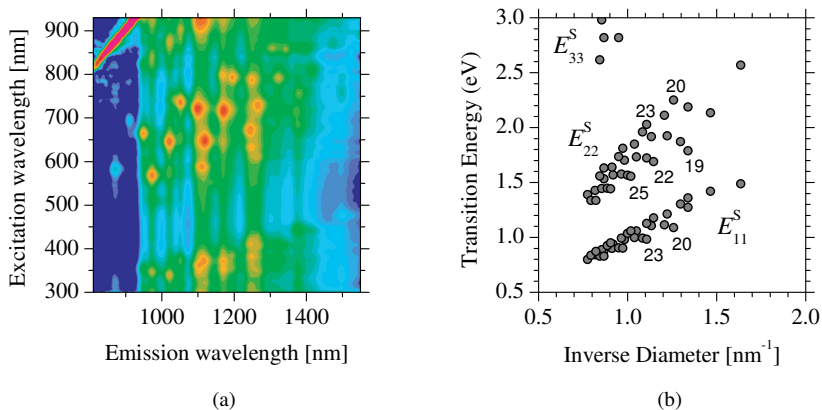
Figure 2.13 (a) 2D photoluminiscence (PL) map measured on wrapped HiPco SWNTs suspended by SDS surfactant in aqueous solution [40]. (b) The Kataura plot extracted from the PL map [25]. The numbers show the constant $2n+m$ families. Reproduced from Ref. [38].
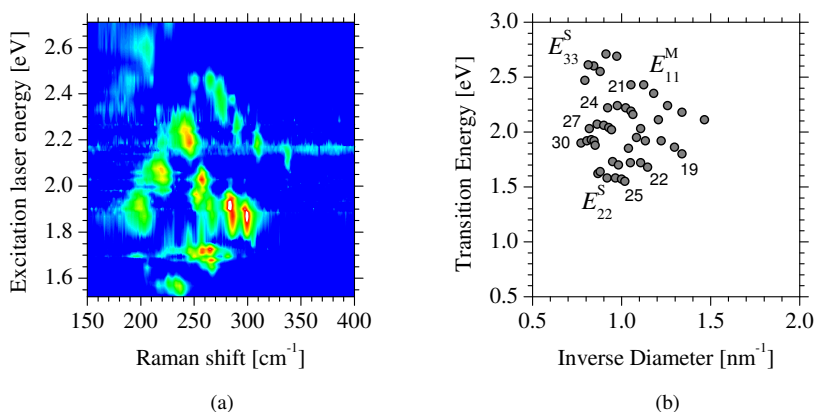
Figure 2.14 (a) The resonance Raman spectral density map in the frequency range of the RBM measured on wrapped HiPco SWNTs suspended by SDS surfactant in aqueous solution[41]. (b) The Kataura plot extracted from the map in (a). The numbers show the constant $2n + m$ families. Reproduced from Ref. [38].

In search for the origin of the family spread, we reconsider the limitations of the STB model discussed previously. Within the STB model, the long-range atomic interactions and the effect of the curvature of the cylindrical surface of a SWNT are both neglected. The long-range atomic interactions are known to change the electronic band structure of the graphene sheet and SWNTs. On the other hand, in the presence

---

Fig. 2.13: fig/fch2-pl.eps
Fig. 2.14: fig/fch2-rrs.eps
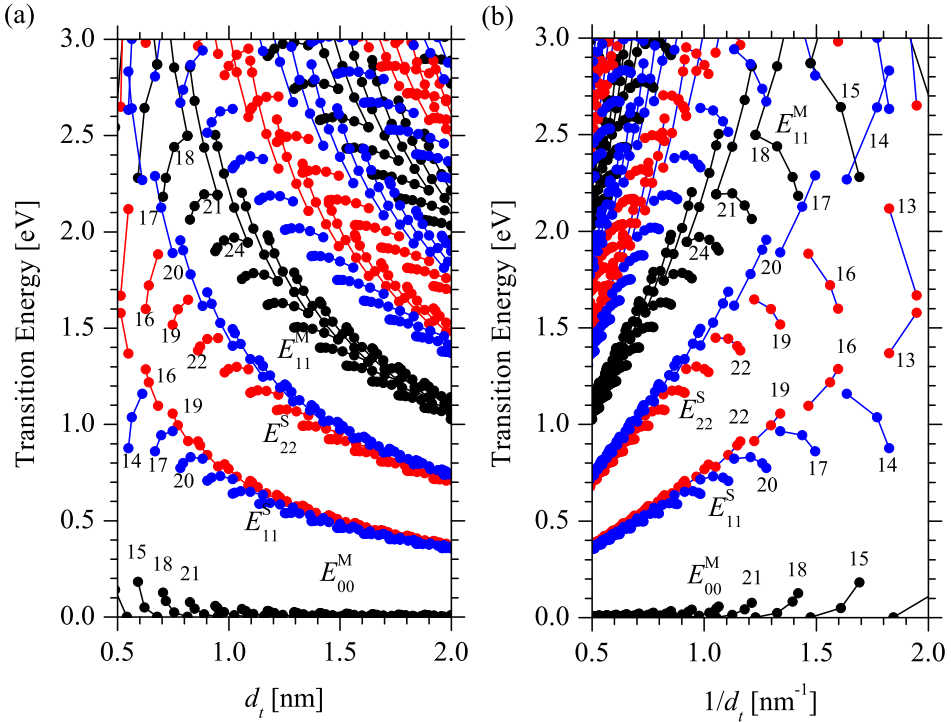
Figure 2.15   The ETB Kataura plot similar to the STB Kataura plot in Fig. 2.12 as a function of (a) SWNT diameter d_t, and (b) inverse diameter $1/d_t$. The ETB model takes into account the long-range atomic interactions, the curvature effects of small diameter SWNTs, and the optimized geometrical structures of the SWNTs. Black, red, and blue dots correspond to M-, S1-, and S2 SWNTs, respectively. The constant $2n + m$ families are connected by lines. Reproduced from Ref. [38].

of the curvature, the π orbitals are mixed with the σ orbitals. Furthermore, the σ-π rehybridization suggests that the geometrical structure of a small diameter SWNT deviates from the rolled up graphene sheet. A geometrical structure optimization must thus be performed to allow for atomic relaxation to equilibrium positions. This in turn affects the E_{ii} energies of the small diameter SWNTs. In the case of GNRs and large diameter SWNTs, however, the σ molecular orbitals are irrelevant because the surface is flat and thus the σ and π molecular orbitals are orthogonal to each other.

Based on the above consideration, the STB model is extended by including the long-range atomic interactions and the σ molecular orbitals, and by optimizing the geometrical structure. The resulting model is referred to as the extended tight-binding model (ETB). Within the framework of the ETB model, we use the tight-binding parametrization determined from density-functional theory (DFT) employing
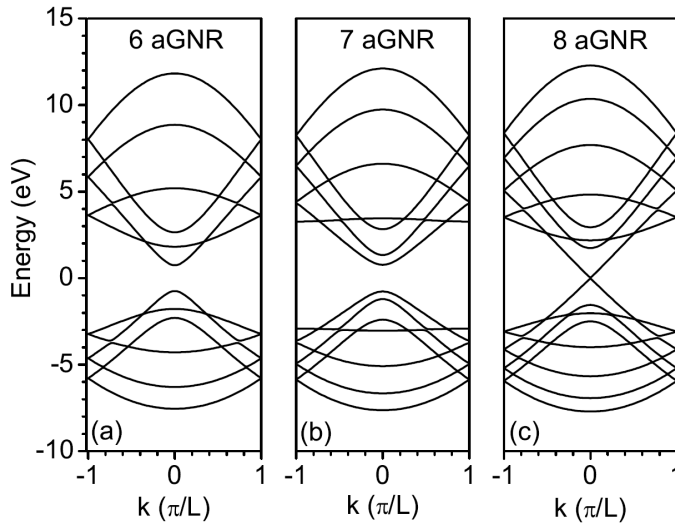
Figure 2.16 Electronic energy bands for 6-, 7- and 8-aGNR nanoribbons calculated in the ETB model.

the local-density approximation (LDA) and using a local orbital basis set [42]. The ETB model is calculated in detail by Samsonidze *et. al* [43]. We closely follow his approach for the ETB electronic structure calculation.

Figure 2.15 show the calculated ETB Kataura plot as a function of tube diameter and inverse diameter. The plot exhibits a similar family spread to the PL and RRS experimental Kataura plots in Figs. 2.13(b) and 2.14(b). The family spread is concluded to be related to the curvature effect of SWNTs. However, although the family spread of the ETB model is in good agreement with the PL and RRS Kataura plots, it still deviates $200 - 300\,\mathrm{meV}$ from the PL and RRS experiments. This deviations originates from the excitonic many-body effects which will be discussed in Sec. 2.4

2.2.5   Nanoribbon electronic structure

The GNR electronic structure depends on the edge shape. In the case of armchair GNRs (aGNRs), they can belong to one of three families depending on the mod number $\mathrm{mod}(N_{ab}, 3)$. Similar to the SWNTs with the use of an ETB calculation considering the long-range interactions but neglecting the curvature effects, we can classify mod 0 and mod 1 aGNRs as semiconductors and mod 2 aGNRs as metals [37, 44].

Bandstructures for π electrons in three representative aGNRs calculated within the ETB model are shown in Fig. 2.16. The 6-aGNR and 7-aGNR ribbons are semi-

---

Fig. 2.16: fig/fch2-agnrelstruct.eps
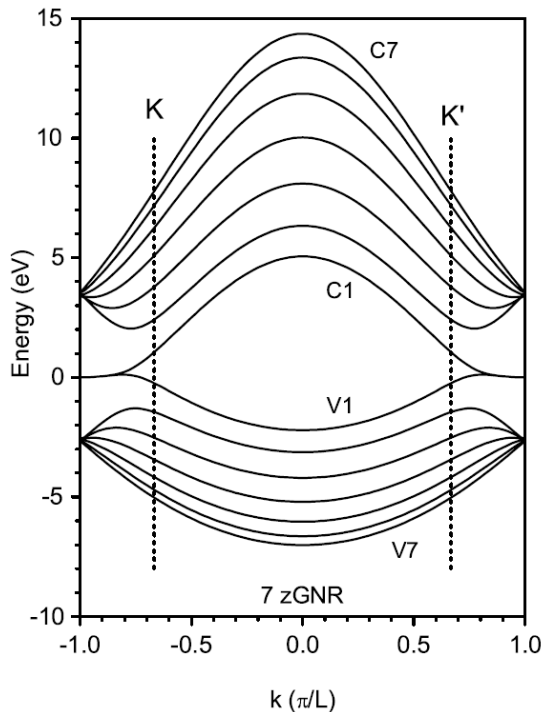
Figure 2.17 Electronic energy bands a 7-zGNR nanoribbon calculated in the ETB model. The lowest seven bands labeled v1 ... v7 are the valence bands, while the highest seven bands labeled c1 ... c7 are the conduction bands.

conducting with finite band gaps, while the 8-aGNR ribbon is metallic. Armchair semiconducting nanoribbons have direct gaps that arise from quantum confinement and edge effects and all the electronic wavefunctions near the band edge are distributed throughout the width of the ribbon.

In the case of zigzag GNRs, all of them are metallic and there is no classification into qualitatively distinct types like there is in armchair nanoribbons. It should be noted, however, that the localized electronic energy band, which are the so-called edge states, exists for zGNR in which the c1 and v1 energy bands as shown in Fig. 2.17 are merged into degenerate energy bands at the zone boundary region. Since the contribution of the edge states to coherent phonon amplitudes is not clear yet, we will not discuss the coherent phonon properties in zGNRs and we will mainly consider the aGNRs in Chapter 4

Fig. 2.17: fig/fch2-zgnrelstruct.eps
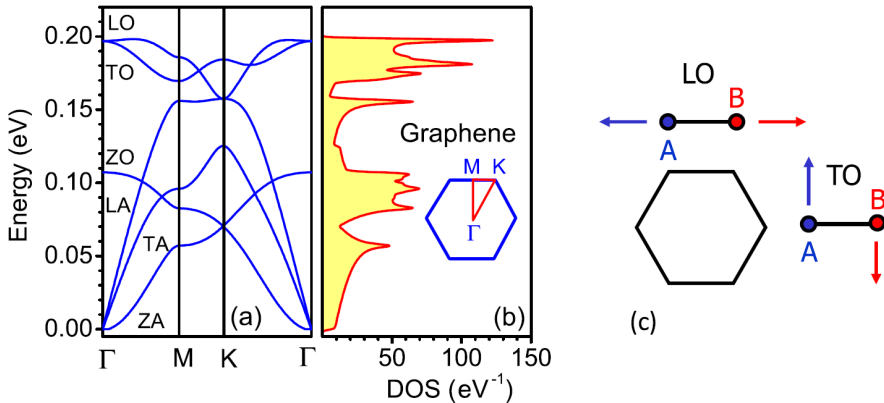
Figure 2.18 (a) Graphene phonon energies, $\hbar\omega(\mathbf{q})$, along high symmetry lines in the hexagonal Brillouin zone. (b) Phonon density of states in units of phonon modes per hexagonal unit cell per eV. The high symmetry lines are shown schematically in the inset where the Brillouin zone has been rotated clockwise by $30°$. In (c) the mode displacement vectors for the $\mathbf{q} = 0$ in-plane LO and TO phonons are shown schematically.

2.3 Vibrational properties

Phonons in graphene, SWNTs and GNRs have been studied by a number of techniques including elastic continuum models [45, 46], force constant models [1, 47, 48, 49, 50] bond charge models[51], and *ab initio* methods [52, 53, 54, 55]. Here, we treat phonon dispersion relations in planar graphene using a force constant model [47], which we also refer to as the valence force field model (VFF). We include radial (r) bond-stretching interactions as well as transverse in-plane (ti) and out-of-plane (to) bond bending interactions. The force constants for these interactions are denoted $\phi_r^{(n)}$, $\phi_{ti}^{(n)}$, and $\phi_{to}^{(n)}$ respectively where the integers $n = 1 \ldots 4$ label the nearest neighbor atomic shells surrounding each carbon atom.

We must include at least fourth neighbor interactions to describe the bond twisting interaction involving a carbon-carbon sp^2 bond and the four attached carbon-carbon bonds with a total of six carbon atoms. The most widely separated of these six carbon atoms are separated by the fourth neighbor distance. We use 12 force constant values obtained from fits to experimental data [47] keeping up to fourth neighbor interactions. In graphene, there are two atoms per hexagonal unit cell giving rise to six phonon branches. The phonon energies $\hbar\omega(\mathbf{q})$ and corresponding mode displacement vectors are obtained by diagonalizing a 6×6 dynamical matrix [47].

The graphene phonon dispersion relations are shown in Fig. 2.18(a) where phonon energy is plotted along high symmetry lines in the hexagonal Brillouin zone. There are six phonon modes. The corresponding density of states for the phonon modes in
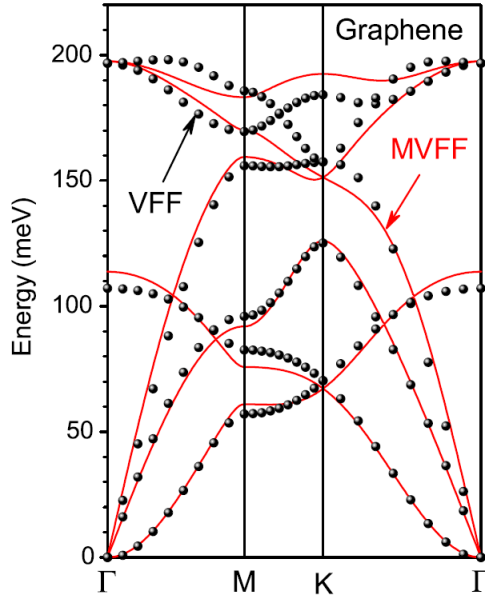
Figure 2.19 Graphene phonon energies, $\hbar\omega(\mathbf{q})$, along high symmetry lines in the hexagonal Brillouin zone. Black dots are obtained using the 12 parameter valence force field model (VFF) described in the text and the solid red curves are the best fit phonon energies for the 7 parameter modified valence force field model (MVFF). The MVFF fits are optimized for low phonon energies.

units of modes per hexagonal unit cell per eV is shown in Fig. 2.18(b). Near the Γ point ($\mathbf{q} = 0$), there are three acoustic and three optical branches. The lowest acoustic branch is an out-of-plane transverse mode (ZA) whose energy varies as $\mathbf{q}^2$. There are two in-plane acoustic modes with energies varying linearly as $|\mathbf{q}|$. The lower lying of these two modes is a transverse acoustic mode (TA) and the higher lying mode is a longitudinal acoustic mode (LA). The lowest lying optical branch is an out-of-plane transverse mode (ZO) with a negative $\mathbf{q}^2$ energy dependence at the Γ point. The remaining two optical branches are in-plane transverse optical (TO) and longitudinal optical (LO) modes which are degenerate at the Γ point and whose energy dependence is approximately constant for small values of $\mathbf{q}$. For the Γ point LO mode the A and B atoms vibrate parallel to the graphene $\hat{x}$ axis (parallel to the bond connecting the A and B atoms) 180 degrees out of phase with each other. For the Γ point TO mode the atoms vibrate out of phase with each other parallel to the graphene $\hat{y}$ axis. The mode displacement vectors for the LO and TO modes are shown schematically in Fig. 2.18(c).

The above valence force field model works well for graphene and planar carbon structures such as GNRs. However, in SWNTs where the curvature effects are impor-

Fig. 2.19: fig/fch2-grphdisp2.eps
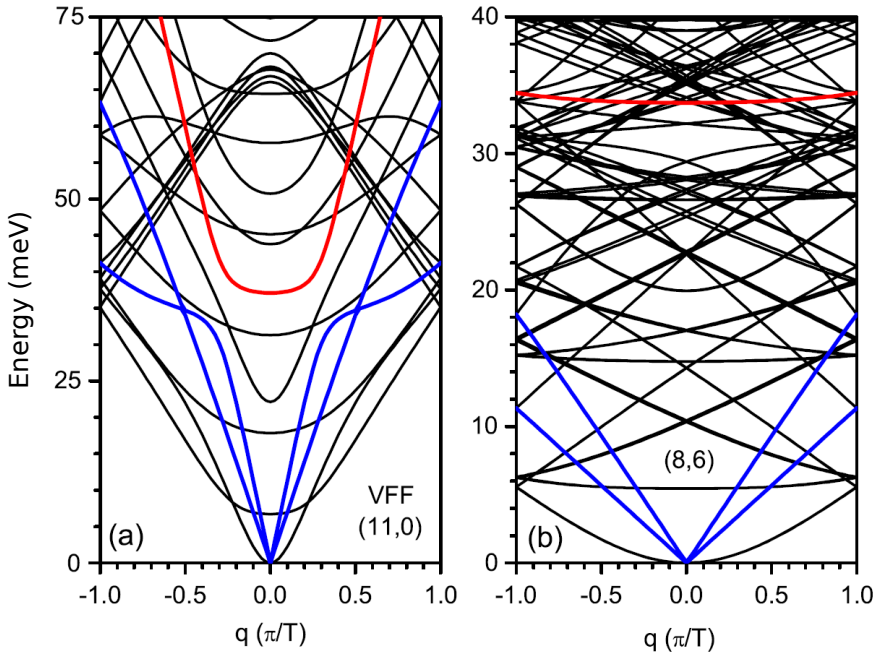
Figure 2.20 Phonon dispersion relations for (a) the (11,0) zigzag SWNT and (b) the (8,6) chiral SWNT calculated using the modified valence force field model. The acoustic modes are thick blue lines and the radial breathing mode (RBM) is shown as a thick red line.

tant, special care must be taken to ensure that the force constant sum rule is obeyed [56]. This simply means that the valence force field potential energy terms must be invariant under rigid translations and rigid rotations of the nanotube about the nanotube axis. In Ref. [49], Mahan and Jeon pointed out that many calculations in the literature use force field models that violate the force constant sum rule and fail to reproduce long wavelength flexure modes predicted by elasticity theory. To remedy this problem in our calculations, we treat lattice dynamics in carbon nanotubes using a modified valence force field model (MVFF) in which the force constant sum rule is obeyed so that the force field potentials are invariant under rigid translations and rotations. In our MVFF model, we include bond stretching, in-plane bond bending, out-of-plane bond bending, and bond twisting potentials. Our MVFF model for SWNTs has seven force constants [11], four due to bond stretching interactions out to fourth nearest neighbor shells and one each from the remaining three interactions. We obtained force constants for the MVFF model by fitting our MVFF results for graphene to the ordinary VFF results shown in Fig. 2.18.

Figure 2.19 shows the best fit MVFF results as red solid lines and the VFF model results as black dots. In the fitting procedure, we gave added emphasis to the low

frequency phonons. In what follows, we will use the VFF model in graphene and GNRs and the MVFF model for SWNTs. The force constants in our phonon models are, however, independent of the density of photoexcited carriers and cannot describe phonon softening observed at high values of the laser fluence, which are not considered in this work, because we will not discuss the high-frequency optical phonon modes.

Figure 2.20 shows the computed phonon dispersion relations for the zigzag (11,0) and chiral (8,6) semiconducting SWNTs. Because of the SWNT screw symmetries, the phonon dynamical matrix can be block diagonalized into 6×6 submatrices each of which corresponds to a different value of the cutting line index $\mu = 0, \ldots, N_{\text{hex}}-1$. The coherent phonon active phonon modes are $q = 0$ modes with nonzero frequency and cutting line index $\mu = 0$. The coherent phonon active mode with the lowest frequency is the radial breathing mode (RBM) which corresponds to the lattice vibration along the tube diameter direction. In Fig. 2.20 the $\mu = 0$ acoustic phonon branches are shown as blue lines while the $\mu = 0$ branches containing the $q = 0$ RBM are shown as thick red lines.

As for the GNR system, we show the phonon dispersion for a representative armchair GNR in Fig. 2.21. A typical mod 1 semiconducting nanoribbon is the 7-aGNR. In GNRs, the coherent phonon active mode with the lowest phonon energy is the radial-breathing-like mode (RBLM) mode at $q = 0$. Figure 2.21 shows the 7-aGNR unit cell with 14 carbon atoms, and superimposed on these atoms are vectors proportional to the atomic displacements in the RBLM mode as determined in the valence force field model. As can be seen in the figure, the RBLM mode represents a periodic expansion and contraction of the ribbon width. The inset shows the phonon dispersion relations for out-of-plane modes (red curves) and in-plane phonon modes (black curves). The phonon branch containing the RBLM mode is shown as a thick black line and the RBLM mode at $q = 0$ is indicated by a yellow dot. Additionally, the RBLM phonon energy is found to be 51 meV.

2.4   Excitonic properties of SWNTs

Exciton effects in SWNTs are very important due to confinement of electrons and holes in the 1D system. Though in the previous sections we have seen that the single particle (electron) model within the tight-binding approximation can partially describe the optical transition energies, the presence of excitons in the real case cannot be neglected, as is indicated by the large exciton binding energy measured in the experiments [27, 28]. Moreover, the many-body corrections can only be understood by taking into account the exciton effects. In this section, the methods for calculating the transition energies in the exciton picture are reviewed and some relevant results will be discussed. The electron-hole corrections are included via the Bethe-Salpeter equation and the

---

Fig. 2.21: fig/fch2-agnrphdisp.eps
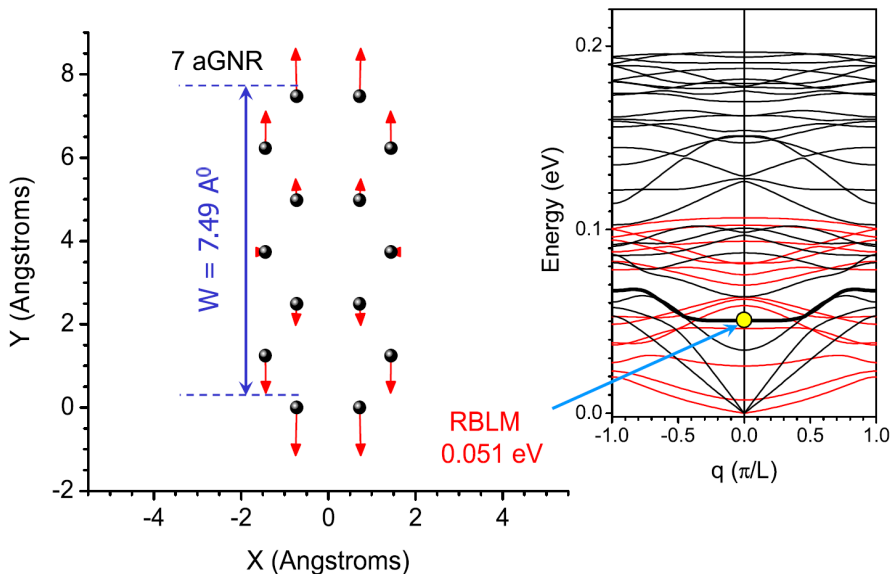
Figure 2.21 Phonon mode pattern for the RBLM mode (phonon energy 51 meV) in a 7-aGNR mod 1 semiconducting nanoribbon. The coherent phonon amplitude is proportional to the ribbon width and increasing amplitude corresponds to ribbon width expansion. The phonon dispersion relation is shown on the right with the phonon branch containing the RBLM mode at $q = 0$ shown as a thick black line. The red lines correspond to out-of-plane modes and the black lines are in-plane modes.

calculation is again performed within the ETB approximation as the ETB model has been proven to accurately predict the electronic properties of SWNTs. This framework has been summarized into an exciton energy calculation package following the work by Jiang *et al.* [34] and Sato *et al.* [57]. The computer program is now maintained in our research group.

2.4.1 Bethe-Salpeter equation

Exciton is an electron-hole pair bound by a Coulomb interaction and thus localized either in real space or k space. But in solids, all wave functions are delocalized as the Bloch wave functions, which are specified by the electron wavevector ($\mathbf{k}_c$) or the hole wavevector ($\mathbf{k}_v$). To create an exciton wave function from the electron and hole wave functions, the electron and hole Bloch functions at many ($\mathbf{k}_c$) and ($\mathbf{k}_v$) wave vectors have to be mixed. The mixing of different wavevectors by the Coulomb interaction is obtained by the so-called Bethe-Salpeter equation [58, 59, 34]:

$$\sum_{\mathbf{k}_c, \mathbf{k}_v} [(E(\mathbf{k}_c) - E(\mathbf{k}_v))\delta(\mathbf{k}'_c, \mathbf{k}_c)\delta(\mathbf{k}'_v, \mathbf{k}_v) + K(\mathbf{k}'_c\mathbf{k}'_v, \mathbf{k}_c\mathbf{k}_v)]\Psi^n(\mathbf{k}_c, \mathbf{k}_v) = \Omega_n \Psi^n(\mathbf{k}'_c, \mathbf{k}'_v),$$

$$(2.39)$$

where $E(\mathbf{k}_c)$ and $E(\mathbf{k}_v)$ are the quasi-electron and quasi-hole energies, respectively. The "quasiparticle" means that a Coulomb interaction is added to the single particle energy and the particle has a finite life time in an excited state. Ω_n and Ψ^n are the n-th excited state exciton energy and corresponding exciton wavefunction.

The mixing term or kernel $K(\mathbf{k}'_c\mathbf{k}'_v, \mathbf{k}_c\mathbf{k}_v)$ is given by

$$K(\mathbf{k}'_c\mathbf{k}'_v, \mathbf{k}_c\mathbf{k}_v) = 2\delta_S K^x(\mathbf{k}'_c\mathbf{k}'_v, \mathbf{k}_c\mathbf{k}_v) - K^d(\mathbf{k}'_c\mathbf{k}'_v, \mathbf{k}_c\mathbf{k}_v), \qquad (2.40)$$

with $\delta_S = 0$ for spin triplet states and $\delta_S = 1$ for spin singlet states. The direct interaction kernel K^d for the screened Coulomb potential w is given by the integral

$$
\begin{aligned}
K^d(\mathbf{k}'_c\mathbf{k}'_v, \mathbf{k}_c\mathbf{k}_v) &= W(\mathbf{k}'_c\mathbf{k}_c, \mathbf{k}'_v\mathbf{k}_v) \\
&= \int d\mathbf{r}' d\mathbf{r} \psi^*_{\mathbf{k}'_c}(\mathbf{r}')\psi_{\mathbf{k}_c}(\mathbf{r}')w(\mathbf{r}',\mathbf{r})\psi_{\mathbf{k}'_v}(\mathbf{r})\psi^*_{\mathbf{k}_v}(\mathbf{r}), \qquad (2.41)
\end{aligned}
$$

and the exchange interaction kernel K^x for the bare Coulomb potential v is

$$K^x(\mathbf{k}'_c\mathbf{k}'_v, \mathbf{k}_c\mathbf{k}_v) = \int d\mathbf{r}' d\mathbf{r} \psi^*_{\mathbf{k}'_c}(\mathbf{r}')\psi_{\mathbf{k}'_v}(\mathbf{r}')v(\mathbf{r}',\mathbf{r})\psi_{\mathbf{k}_c}(\mathbf{r})\psi^*_{\mathbf{k}_v}(\mathbf{r}), \qquad (2.42)$$

where ψ is the single particle wave function.

The quasi-particle energies are calculated from the single particle energy $\epsilon_{\text{sp}}(\mathbf{k})$ by including the self-energy corrections $\Sigma(\mathbf{k})$:

$$E(\mathbf{k}_c) = \epsilon_{\text{sp}}(\mathbf{k}_c) + \Sigma(\mathbf{k}_c), \qquad (2.43)$$

$$E(\mathbf{k}_v) = \epsilon_{\text{sp}}(\mathbf{k}_v) + \Sigma(\mathbf{k}_v), \qquad (2.44)$$

where $\Sigma(\mathbf{k})$ is expressed as

$$\Sigma(\mathbf{k}_c) = -\sum_{\mathbf{q}} W[\mathbf{k}_c(\mathbf{k}+\mathbf{q})_v, (\mathbf{k}+\mathbf{q})_v\mathbf{k}_c], \qquad (2.45)$$

$$\Sigma(\mathbf{k}_v) = -\sum_{\mathbf{q}} W[\mathbf{k}_v(\mathbf{k}+\mathbf{q})_v, (\mathbf{k}+\mathbf{q})_v\mathbf{k}_v]. \qquad (2.46)$$

In order to obtain the kernel and self energy, the single particle Bloch wave function $\psi_{\mathbf{k}}(\mathbf{r})$ here is approximated by an ETB wave function. The dielectric screening effect is considered within a random phase approximation (RPA), in which the static screened Coulomb interaction is given by

$$W = \frac{V}{\kappa\epsilon(\mathbf{q})}, \qquad (2.47)$$

with the dielectric function $\epsilon(\mathbf{q}) = 1 + v(\mathbf{q})\Pi(\mathbf{q})$ that describes effects of the polarization of the π bands. The effect of electrons in core states, σ bonds, and the surrounding materials are all represented by a static dielectric constant κ. By calculating the polarization function $\Pi(\mathbf{q})$ and the Fourier transformation of the unscreened
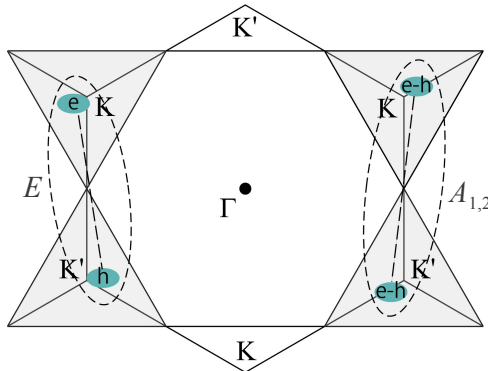
Figure 2.22 Symmetry of an exciton. If both the electron and hole are from the K (or K′) region (right side of the above figure), the corresponding exciton is an $A_{1,2}$ symmetry exciton. If an electron is from the K region and a hole is from the K′ region (left side of the above figure), the corresponding exciton is an E symmetry. One more case is not shown here, the E^* exciton, which is just an opposite situation of the E exciton.

Coulomb potential $v(\mathbf{q})$, the exciton energy calculation can be performed. For 1D materials, the Ohno potential is commonly used for the unscreened Coulomb potential $v(\mathbf{q})$ for π orbitals [29]. After obtaining the excitation energy Ω_n, the exciton bind- ing binding energy E_{bd} can be calculated by substracting the quasi particle energy $E_{\mathrm{QP}} = E_c(\mathbf{k}_c) - E_v(\mathbf{k}_v)$ with Ω_1,

$$E_{\mathrm{bd}} = E_{\mathrm{QP}} + \Omega_1. \tag{2.48}$$

Here Ω_1, which is the first (lowest) exciton state, is interpreted as the transition energy E_{ii}, where an electron and a hole lie on the same i-th cutting line with respect to the K point of the 2D Brillouin zone of graphene. The difference between E_{ii} and the single particle band gap gives the many-body corrections E_{mb} which is also the difference between the self energy and binding energy,

$$E_{\mathrm{mb}} = \Sigma - E_{\mathrm{bd}}. \tag{2.49}$$

2.4.2 Exciton symmetry

To discuss the exciton symmetry, wave vectors $\bar{\mathbf{K}}$ for center-of-mass motion and $\mathbf{k}$ for relative motion are introduced,

$$\bar{\mathbf{K}} = (\mathbf{k}_c - \mathbf{k}_v)/2, \quad \mathbf{k} = \mathbf{k}_c + \mathbf{k}_v. \tag{2.50}$$

The exciton state can then be denoted as $|\mathbf{k}, \bar{\mathbf{K}}\rangle$ and the Bethe-Salpeter equation is rewritten in terms of $\bar{\mathbf{K}}$ and $\mathbf{k}$. Because the Coulomb interaction is related to the

Fig. 2.22: fig/fch2-wfzone.eps
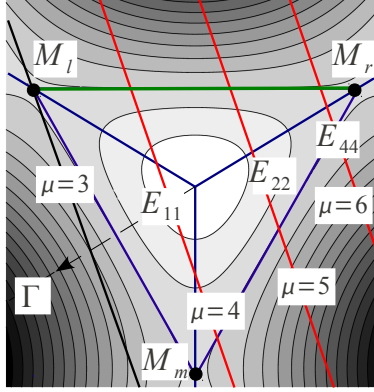
Figure 2.23 Wave vectors of a $(6,1)$ SWNT nanotube around the K point. The cutting lines must cross the $M_l M_r$ line in order to have an E_{ii} within the 3M region. The index μ is counted from the Γ point.

relative coordinate of an electron and a hole, the excitons in SWNTs can be classified according to the $2\bar{\mathbf{K}}$ value in the regions shown in Fig. 2.22.

There are three inequivalent regions in the 2D Brillouin zone of graphene, i.e. two triangle regions around K, K′, and a hexagonal region around the Γ point. For SWNTs, the optical transitions are related to the electron and hole on the cutting lines in the K or K′ regions. If both the electron and hole are from the K (or K′) region, the corresponding exciton is an $A_{1,2}$ symmetry exciton. The center-of-mass momentum $2\bar{\mathbf{K}}$ lies in the Γ region and $\mathbf{k}$ will be around K (or K′) region. If an electron is from the K region and a hole is from the K′ region, the corresponding exciton is an E symmetry. The momentum $2\bar{\mathbf{K}}$ lies in the K region. If an electron is from the K′ region and a hole is from the K region, their $2\bar{\mathbf{K}}$ lies in the K′ region, and this exciton is an E^* symmetry exciton.

The E and E^* excitons, which have a large angular momentum for the center-of-mass momentum, are dark excitons because the photon wave vector is nearly zero. For A excitons, the electron-hole pair $|\mathbf{k}_c, \mathbf{k}_v\rangle = |\mathbf{k}, \bar{\mathbf{K}}\rangle$ with the electron and hole from the K′ region and $|-\mathbf{k}_c, -\mathbf{k}_v\rangle = -|\mathbf{k}, \bar{\mathbf{K}}\rangle$ with the electron and hole from the K′ region have the same value for $\bar{\mathbf{K}}$. Here $|\mathbf{k}, \bar{\mathbf{K}}\rangle$ is antisymmetric, whereas $-|\mathbf{k}, \bar{\mathbf{K}}\rangle$ is symmetric, under the C_2 rotation. The corresponding excitons are labeled A_2 and A_1 excitons, respectively. The optical dipole moment is defined as

$$\mathcal{M} \propto \hat{\mathbf{P}} \cdot \langle \Psi | \nabla | \Psi_0 \rangle, \tag{2.51}$$

with $\langle \Psi |$ and $|\Psi_0\rangle$ denoting the excited and ground states, respectively, and $\hat{\mathbf{P}}$ is the light polarization vector. The ground state $|\Psi_0\rangle$ has an s symmetry and operator ∇ is antisymmetric under the C_2 rotation. In order to get a nonzero $\mathcal{M}$, $|\Psi\rangle$ thus should

Fig. 2.23: fig/fch2-mmm.eps
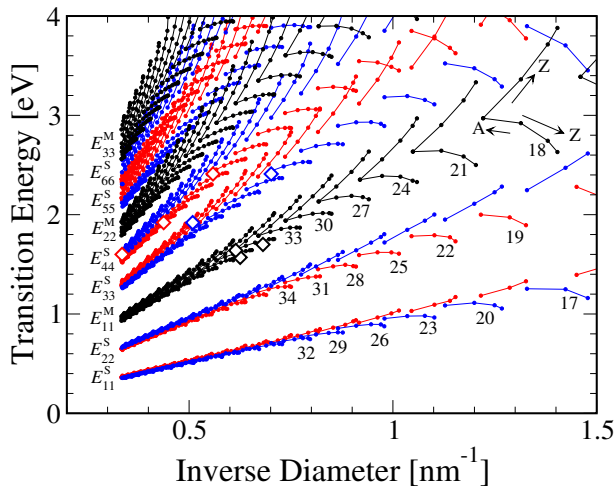
Figure 2.24 The bright exciton energy Kataura plot as a function of inverse diameter $1/d_t$ for $\kappa = 2.22$. The exciton energies E_{ii} shown here are up to E_{66}^{S} and E_{33}^{M}. Black, red, and blue dots correspond to M-, S1-, and S2 SWNTs, respectively. The eight diamond symbols are experimental data by Michel *et al.* (Ref. [61]). The $2n + m$ family patterns are clearly seen for smaller diameter SWNTs. The arrows with A (Z) symbols correspond to the near armchair (zigzag) SWNTs.

be antisymmetric, too. Therefore, A_1 excitons are dark excitons, and only A_2 excitons are bright excitons. Hereafter, only the case of bright excitons is considered because the optical transitions in coherent phonon generation are related to the optical dipole transitions of the bright exciton.

For the bright excitons, the cutting lines k_{ii} near the K point is important to determine exciton energies E_{ii}. A triangular region which connects three M points, i.e., M_l, M_r, and M_m around the K is defined as the 3M triangle as shown in Fig. 2.23. Only in this region the energy dispersion of the conduction (valence) band for a SWNT has a minimum (maximum). The remaining region of the Brillouin zone is a hexagonal region which connects six M points around the Γ point. In the hexagonal region, the conduction (valence) bands have a maximum (minimum). This gives a singular joint of density of states but a minimum electron-photon matrix element at the singular point [60]. Thus a cutting line will not contribute to the optical absorption at E_{ii} if the cutting line lies outside of the $3M$ triangle. As for example, a $(6, 1)$ SWNT shown in Fig. 2.23 does not have E_{33} optical absorption because the corresponding cutting line cannot lie within the $3M$ triangle. Therefore, E_{33} is skipped, only E_{11}, E_{22}, and E_{44} are observed in experiments, though all E_{ii} values can be calculated by theory.

Figure 2.24 shows the calculated results for the lowest bright exciton states but different cutting lines k_{ii}, which then give the exciton energies E_{ii}. The results for
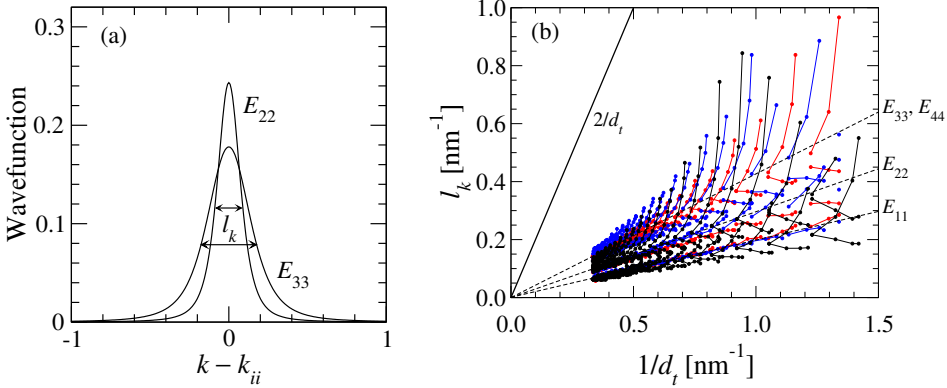
Figure 2.25 (a) Exciton wave functions in 1D k space for a $(20,0)$ semiconducting SWNT. The states shown here are for E_{22} and E_{33}. The wave function half-width l_k increases with E_{ii}. (b) l_k for many SWNTs as a function of $1/d_t$. The cutting line spacing $2/d_t$ is shown by the solid line for comparison. The dashed lines indicate the corresponding E_{ii} states. The spacing between E_{33} and E_{44} is not distinguished clearly.

higher exciton states on a given cutting line is beyond the scope of the present discussion. The Kataura plot in figure 2.24 is given as a function of inverse tube diameter in the range of $0.3 < d_t < 3.0$ nm. The E_{ii} calculation is performed by taking a single constant $\kappa = 2.22$ which is fitted from the experimental E_{ii} data of the RRS or PL measurements for SWNT bundle samples. Like the single particle ETB model, the exciton ETB Kataura plot also shows the $2n+m$ family patterns, but unlike the single particle picture this excitonic plot can be adjusted by changing κ.

    The eight diamond symbols are experimental results for suspended SWNTs given by Michel *et al.* [61] in which they succeeded with an assignment of (n,m) for SWNTs with diameters of up to 3 nm. Although their results are for isolated suspended SWNTs, and the calculation is for bundles, the calculated results for their assigned (n,m) values reproduce well all eight points within the environmental effect shifts up to 80 meV [62].

2.4.3   Exciton size

The localized exciton wavefunction is constructed by mixing many k states in which the mixing coefficients are determined by the Bethe-Salpeter equation. In Fig. 2.25(a), the wave function for a $(20,0)$ SWNT is shown. The exciton wave function half-width l_k indicates the exciton size in reciprocal space. Since the Fourier transformation of this wave function will also give a similar localized function, the width in real space gives the exact exciton size or radius, that is the effective distance between an electron and a hole in the bound electron-hole pair. The exciton size in real space is thus

inversely proportional to l_k.

To study the wave function size dependence on chirality, the width l_k for the E_{11} up to E_{44} states are calculated for all SWNTs with diameters d_t in the same range as in the exciton energy calculation, $0.3 < d_t < 3.0\,\mathrm{nm}$, shown in Fig. 2.25. For comparison, the cutting line spacing $2/d_t$ is also shown in the figure by the solid line. It is clear that l_k is always smaller than the cutting line spacing $2/d_t$. Because l_k measures the extended length of a wave function in k space, this result indicates that one cutting line is sufficient to describe E_{ii} states. Fig. 2.25 also implies that the inverse of l_k, which is the exciton size in real space, spans around $0.5 - 2.0\,\mathrm{nm}$. Later in Chapter 5 we will particularly consider a $(11, 0)$ tube which has exciton size in real space of about $0.9\,\mathrm{nm}$.

Fig. 2.25: fig/fch2-lk.eps

Chapter 3

Theory of coherent phonon generation process

In this chapter, we provide the theory of coherent phonon generation process in general semiconductor nanostructures [10]. We then derive the equation of motion for coherent phonons in single-wall carbon nanotubes (SWNTs) [11, 12, 14] and graphene nanoribbons (GNRs) [13]. It is found that the coherent optical phonon amplitudes satisfy a driven harmonic oscillator equation and that the carriers photoexcited by an ultrafast pump acted as a driving source for coherent optical phonon oscillations via the deformation potential coupling between electrons (or holes) and phonons. The calculation methods for electron-photon and electron-phonon interactions, which govern the driving force of coherent phonons, are also presented in this chapter. We particularly utilize the tight-binding approximation and effective-mass theory for describing the electronic states appearing in the interaction processes.

3.1 Phenomenological model of coherent phonons

To explain oscillations observed in the differential transmission and reflectivity data of the pump-probe experiments, early researchers attributed these phenomena to the coherent phonon oscillations which phenomenologically follow a driven harmonic oscillator [15]. The evolution of a coherent phonon amplitude Q in the presence of a driving force exerted by ultrafast laser pulse is governed by the differential equation which follow a phenomenological driven oscillator model,

$$\frac{\partial^2 Q(t)}{\partial t^2} + 2\gamma_{\mathrm{D}} \frac{\partial Q(t)}{\partial t} + \omega_0^2 Q(t) = \frac{F(t)}{M_{\mathrm{s}}},$$ (3.1)

where ω_0 is the frequency of the phonon mode, γ_{D} is the damping parameter, M_{s} is the mass of the system, and F is the driving force. This force may depend on carrier density, temperature, and other parameters of the system. The damping parameter

γ_D is the inverse of the dephasing time of the coherent phonon mode [16]. The dephasing time comes from a combination of phase-destroying processes and population decreasing processes, such as anharmonicity and electron-phonon interaction lifetime.

Phenomenological model in Eq. (3.1) can be solved analytically by using Fourier transform or Green's function method with the initial condition that both $Q(t)$ and $\partial Q/\partial t$ are zero before the force $F(t)$ is applied. The solution is given by [5]

$$Q(t) = \int\limits_{-\infty}^{\infty} \frac{F(t-\tau)}{M_s} \frac{e^{-\gamma_D \tau} \sin(\sqrt{\omega_0^2 - \gamma_D^2}\,\tau)}{\sqrt{\omega_0^2 - \gamma_D^2}} d\tau \qquad (3.2)$$

In this solution, the form of the driving force plays an important role in determining the oscillator properties. Let us consider two limiting cases of the forcing functions. The first kind is impulsive force, which has the following form:

$$F(t) = I\delta(t), \qquad (3.3)$$

where $\delta(t)$ is a Dirac delta function in time and thus $I = \int F(t)dt$ is the total impulse delivered to the oscillator. The second kind is displacive force,

$$F(t) = D\theta(t), \qquad (3.4)$$

where $\theta(t)$ is the Heaviside step function and D is the force magnitude.

The generation of the coherent phonons depends on the rapid photoexcitation of electrons and holes by a pump laser pulse. If the pump pulse is not resonant with the electronic levels, quantum mechanics still allows for the creation of electron and holes for a short period of time consistent with the time-energy uncertainty principle. These so called "virtual" carriers adiabatically follow the pump pulse envelope and disappear after the pump pulse is gone. For a short pulse, this is approximately a Dirac delta function and corresponds to impulsive excitation. If the pump laser energy is resonant with the energy levels of the system, then "real" carriers (electrons and holes) are generated during the pump pulse. In this case, the carrier density is proportional to the integral of the pump pulse envelope which is approximately given by a Heaviside step function for a rapid pump pulse. We can then integrate Eq. (3.2) to find the solution for each case (impulsive or displacive model).

By inserting Eq. (3.3) to Eq. (3.2), we obtain the solution for an impulsive force at $t \geq 0$,

$$Q(t) = \frac{I}{M_s \sqrt{\omega_0^2 - \gamma_D^2}} e^{-\gamma_D t} \sin(t\sqrt{\omega_0^2 - \gamma_D^2}). \qquad (3.5)$$

An typical oscillation due to an impulsive force is shown in Fig. 3.1(a). This is similar to ringing a bell, where the driving force is applied for only a short time. The solution shows that an impulsive force starts oscillations about the current equilibrium position, which will damp out exponentially. An impulsive force results if the femtosecond pump
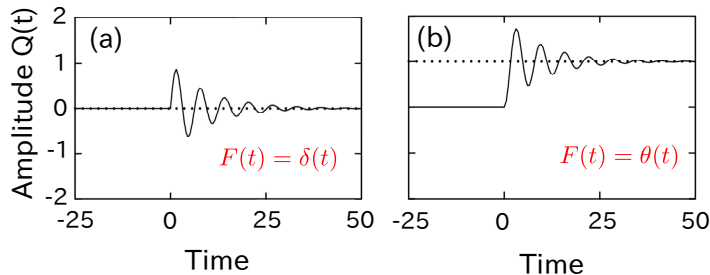
Figure 3.1 Schematic solution to the harmonic oscillator model for (a) impulsive force and (b) displacive force. Here $\gamma_{\mathrm{D}} = 0.1\omega_0$ is used.

pulse is not resonant with the conduction and valence band states as is the case in below bandgap excitation. Because of the uncertainty principle, virtual carriers are created and the density of these carriers will adiabatically follow the pulse envelope.

On the other hand, by inserting Eq. (3.4) to Eq. (3.2), we obtain the solution for a displacive force,

$$Q(t) = \frac{D}{m\omega_0^2}\left[1 - e^{-\gamma_{\mathrm{D}}t}\left(\cos(t\sqrt{\omega_0^2 - \gamma_{\mathrm{D}}^2}) + \frac{\gamma_{\mathrm{D}}}{\sqrt{\omega_0^2 - \gamma_{\mathrm{D}}^2}}\sin(t\sqrt{\omega_0^2 - \gamma_{\mathrm{D}}^2}).\right)\right] \quad (3.6)$$

In Fig. 3.1(b), we show an illustrative oscillation due to a displacive force. The situation is analogous to putting weights on a spring suspended from the ceiling. The weights cause the spring to stretch to a new equilibrium position and if the weights were applied fast enough, the spring will oscillate around the new equilibrium position. Displacive forces typically arise when the femtosecond pump pulse has resonant transitions creating real carriers in the semiconductor as is the case for excitation above the bandgap. However, due to the broad spectral width for ultrafast pump excitation, there are Fourier component for excitation both above and below the bandgap and both real and virtual carriers will in general be created leading to impulsive and displacive contributions to the coherent phonon generation process.

3.2 Microscopic theory of coherent phonons

The phenomenological oscillator model basically gives the essential physics of coherent phonons in semiconductors. However it left open the question of exact definition of the coherent phonon amplitudes. It was found that the key to understanding the microscopic origin of the driven oscillator model for coherent phonon generation is actually to realize that the coherent phonon amplitude is proportional to the following expectation value [10],

$$Q_{\mathbf{q}}(t) \equiv \langle b_{\mathbf{q}} + b_{-\mathbf{q}}^\dagger \rangle, \quad (3.7)$$

Fig. 3.1: fig/fch3-impdisp.eps

where $\langle b_{\mathbf{q}} \rangle$ and $\langle b_{-\mathbf{q}}^{\dagger} \rangle$ are the expectation values of the phonon creation and annihilation operators for phonon wavevector $\mathbf{q}$ and $-\mathbf{q}$, respectively. It is also known that the lattice displacement operator $u(\mathbf{r})$ can be expressed in terms of the phonon creation and annihilation operators,

$$u(\mathbf{r}) = \sum_{\mathbf{q}} \sqrt{\frac{\hbar}{2 M_s \omega_{\mathbf{q}}}} \left(b_{\mathbf{q}} + b_{-\mathbf{q}}^{\dagger} \right) \tag{3.8}$$

where M_s is the mass of the system. Therefore the coherent phonon amplitude is proportional to the Fourier components of the displacement.

We should note that the expectation values 3.7 will vanish in a phonon oscillator eigenstate and there are also fluctuations defined by $\langle u^2 \rangle = \langle b b^{\dagger} + b^{\dagger} b \rangle$. These phonons are incoherent phonons in the mode. However, the expectation values do not vanish for the coherent states given by a coherent superposition of more than one phonon eigenstate. The canonical coherent states are defined for each complex number z in terms of eigenstate of harmonic oscillator,

$$\Psi^{\mathrm{coh}} = |z\rangle = \mathrm{e}^{(z b^{\dagger} - z^* b)} |0\rangle = \sum_{n} \frac{z^n}{\sqrt{n!}} \mathrm{e}^{-z^2} |n\rangle, \tag{3.9}$$

hence we coined the term "coherent phonons". These states are essentially the same as those used in quantum optics to describe the quasi-classical photon states of the electromagnetic field. The coherent phonon states are eigenfunctions of the phonon annihilation operator $b_{\mathbf{q}}$ for phonons with wavevector $\mathbf{q}$, i.e. $b_{\mathbf{q}} |z\rangle = z|z\rangle$, and represent minimum-uncertainty Gaussian wavepackets that oscillate back and forth in the parabolic potential without broadening and thus when the amplitude z is large they behave like a macroscopic harmonic oscillator.

To obtain the equations of motion for $\langle b_{\mathbf{q}}^{\dagger} \rangle$ and $\langle b_{\mathbf{q}} \rangle$, we can use the Heisenberg equations for the expectation values of operators,

$$\frac{d\mathcal{O}}{dt} = \frac{i}{h}[H, \mathcal{O}], \tag{3.10}$$

where $\mathcal{O}$ is any quantum operator. In a simplified system consisting of two electronic bands (conduction and valence bands) interacting with certain phonon modes, the Hamiltonian can be expressed by

$$H = \sum_{n,\mathbf{k}} \epsilon_{n\mathbf{k}} c_{n\mathbf{k}}^{\dagger} c_{n\mathbf{k}} + \sum_{\mathbf{q}} \hbar \omega_{\mathbf{q}} b_{\mathbf{q}}^{\dagger} b_{\mathbf{q}} + \sum_{n,\mathbf{k},\mathbf{q}} \mathcal{M}_{\mathbf{k},\mathbf{q}}^{n} \left(b_{\mathbf{q}} + b_{-\mathbf{q}}^{\dagger} \right) c_{n\mathbf{k}+\mathbf{q}}^{\dagger} c_{n\mathbf{k}}, \tag{3.11}$$

where the first term is the electron Hamiltonian, the second term is the phonon Hamiltonian, and the third term is the electron-phonon interaction Hamiltonian with $\mathcal{M}_{\mathbf{k},\mathbf{q}}^{n}$ as the electron phonon matrix element at the electronic subband n for electron wavevector $\mathbf{k}$ and phonon wavevector $\mathbf{q}$. Inserting this Hamiltonian to the Heisenberg

equation and using the definition of coherent phonon amplitude in Eq. (3.7), we can obtain the dynamical equation of motion for the coherent phonon amplitude,

$$\frac{\partial^2 Q_{\mathbf{q}}(t)}{\partial t^2} + \omega_{\mathbf{q}}^2 Q_{\mathbf{q}}(t) = S_{\mathbf{q}}(t), \tag{3.12}$$

where

$$S_{\mathbf{q}} = -\frac{2\omega_{\mathbf{q}}}{\hbar} \sum_{n,\mathbf{k}} \mathcal{M}_{\mathbf{k},-\mathbf{q}}^n n_{\mathbf{k},\mathbf{k}-\mathbf{q}}^n \tag{3.13}$$

is the driving force of the coherent oscillation (see Appendix A for a detailed derivation of Eqs. (3.12) and (3.13)). Here $n_{\mathbf{k},\mathbf{k}-\mathbf{q}}^n = \langle c_{n\mathbf{k}}^\dagger c_{n\mathbf{k}-\mathbf{q}} \rangle$ is the Fourier transform of the electronic density matrix. The electronic density matrix is nonzero only after excitation with an ultrafast laser pulse. The rapid creation of electrons/holes by the femtosecond pump pulse changes the forcing function and triggers the coherent phonon oscillations.

Equation (3.12) is very similar to the phenomenological model in Eq. (3.1) except that it is written in momentum space. In fact, because of the Fourier transform relation between the coherent phonon amplitude and the lattice displacement, we have actually obtained Eq. (3.1) from the microscopic model in Eq. (3.12). However there is no damping term because the anharmonic terms are neglected in the lattice potential. Since the wavelength of the pump laser is large compared with the spacing between atoms in the nanostructure, usually the electrons and holes are created in a macroscopicaly uniform state, which excites only the $q = 0$ phonon modes. Coherent phonon studies in carbon nanotubes and graphene nanostructures have also focused primarily on the $q = 0$ phonon modes, which include the radial breathing modes (RBMs) in carbon nanotubes and the radial-breathing-like modes in (RBLMs) in graphene nanoribbons. In addition, by considering excitonic effects in carbon nanotubes, we may also expect to excite $q \neq 0$ modes which will be discussed in later chapter of this thesis.

3.3 Equations of motion for coherent phonons in nanotubes and nanoribbons

For a single wall carbon nanotube (SWNT) or graphene nanoribbon (GNR), since we have several subbands for electronic states and phonon energy dispersion, the notation of coherent phonon amplitude is slightly more cumbersome. Both electronic structure and phonon dispersion now have several branches because of zone folding, each of which is denoted by a cutting line label μ and ν, respectively (see the discussion on the cutting line concept in Chapter 2). The equations of motion for coherent phonon modes are obtained using a microscopic description of the electron-phonon interaction as described in the previous section. For each phonon mode in the nanotube and

nanoribbon, the coherent phonon amplitude is given as

$$Q_{m\nu q}(t) \equiv \langle b_{m\nu q} + b^{\dagger}_{m\nu,-q} \rangle, \tag{3.14}$$

where the subscript m labels the six phonon modes in the graphene phonon dispersion and q is the 1D phonon wave vector of the SWNT or GNR. The full expression for the equation of motion is

$$\frac{\partial^2 Q_{m\nu q}(t)}{\partial t^2} + \omega_{m\nu}^2(q) Q_{m\nu q}(t) = -\frac{2\omega_{m\nu}(q)}{\hbar} \sum_{nn'\mu k} \mathcal{M}_{m,\nu}^{nn',\mu}(k,-q) \langle c^{\dagger}_{n',\mu+\nu,k-q}(t) c_{n\mu k}(t) \rangle. \tag{3.15}$$

To simplify Eq. (3.15), we assume that the optical pulse and the distribution of photoexcited carriers are spatially uniform over the nanotube. The electronic density matrix is thus diagonal and can be written as [11]

$$\langle c^{\dagger}_{n',\mu+\nu,k-q}(t) c_{n\mu k}(t) \rangle = \delta_{n',n} \delta_{\nu,0} \delta_{q,0} f_{n\mu}(k,t), \tag{3.16}$$

where $f_{n\mu}(k,t)$ is the photoexcited carrier distribution in the subband $n\mu$ with wavevector k at time t. We also consider that the only coherent phonon modes that are excited are the $\nu = 0$ and $q = 0$ modes, whose amplitudes satisfy a driven oscillator equation,

$$\frac{\partial^2 Q_m(t)}{\partial t^2} + \omega_m^2 Q_m(t) = S_m(t), \tag{3.17}$$

where $Q_m(t) \equiv Q_{m00}(t)$ and $\omega_m \equiv \omega_{m0}(q)$. The driven oscillator equation is solved subject to the initial conditions $Q_m(0) = 0$ and $\dot{Q}_m(0) = 0$. Therefore, taking the initial conditions into account, the driving function $S_m(t)$ is given by

$$S_m(t) = -\frac{2\omega_m}{\hbar} \sum_{n\mu k} \mathcal{M}_m^{n\mu}(k) \left[f_{n\mu}(k,t) - f_{n\mu}(k,0) \right], \tag{3.18}$$

where $f_{n\mu}(k,t)$ is the time-dependent carrier distribution function, $f_{n\mu}(k,t)$ is the initial equilibrium electron distribution function, and $\mathcal{M}_m^{n\mu}(k) \equiv \mathcal{M}_{m,\nu=0}^{n\mu}(k,q=0)$.

The coherent phonon driving function $S_m(t)$ depends on the electron-phonon matrix elements and photoexcited electron distribution functions. In principle, we could solve for the time-dependent distribution functions fully by solving the Boltzmann equation formalism taking photogeneration and relaxation effects into account [11],

$$\frac{\partial f_{n\mu}(k,t)}{\partial t} = \left[\frac{\partial f_{n\mu}(k,t)}{\partial t} \right]_{\text{gen}} + \left[\frac{\partial f_{n\mu}(k,t)}{\partial t} \right]_{\text{sc}} + \left[\frac{\partial f_{n\mu}(k,t)}{\partial t} \right]_{\text{cc}} \tag{3.19}$$

where $f_{n\mu}(k,t)$ is the time-dependent distribution function for electrons (or holes) in subband (n,μ) with wave vector k. The first term on the right-hand side represents the time rate of change of the distribution functions due to transient photogeneration of electron-hole pairs by the pump, while the second term represents the time rate of distribution change due to scattering or relaxation process by optical phonons.

The final term describes the time rate of change of the distribution functions due to carrier-carrier scattering.

To simplify the calculations, we introduce a useful approximation as follows. After photoexcitation, the electron-hole pairs slowly scatter and recombine. Jiang *et al.* found that the relaxation times in graphite-related system are on the order of a few picoseconds, ($\sim 5 - 10\,\text{ps}$) [63], which is much slower than either the ultrafast laser pulse or a typical coherent phonon oscillation period in SWNTs and GNRs considered in this study. The driving function $S_m(t)$ in the present case thus rises sharply in a steplike fashion and then slowly vanishes as the distribution functions $f_{n\mu}(k,t)$ return to $f_{n\mu}(k,0)$. We may then safely neglect slow carrier relaxation effects and retain only the photogeneration term in the Boltzmann equation. Even if the relaxation effects are considered, these can be taken into account by simply including a phenomenological decay constant corresponding to the finite lifetime of photoexcited carriers.

By considering only the photogeneration term in the Boltzmann equation, the net photogenerated conduction-band electron distribution function $f_{c\mu}(k,t) - f_{c\mu}(k,0)$ for any optical transition from the valence band to the conduction band (v $\to$ c) is equal to the net photogenerated hole distribution function $f_{v\mu}(k,t) - f_{v\mu}(k,0)$ for each value of wavevector k. In this case we obtain a simplified expression for the driving function in terms of the conduction band distribution functions,

$$S_m(t) = -\frac{2\omega_m}{\hbar} \sum_{\mu k} \mathcal{M}_m^\mu(k) \left[f_{c\mu}(k,t) - f_{c\mu}(k,0) \right], \tag{3.20}$$

where

$$\mathcal{M}_m^\mu(k) \equiv \mathcal{M}_m^{c\mu}(k) - \mathcal{M}_m^{v\mu}(k) \tag{3.21}$$

is the net electron-phonon matrix element corresponding to the creation of photoexcited electrons and holes at the same time.

3.4 Optical transitions and absorption

In order to obtain the time-dependent carrier distribution, we can compute the photogeneration rate within the dipole approximation using Fermi's golden rule [64], and thus involving the optical (electron-photon) matrix element $\mathcal{D}_{nn'}^\mu(k)$ for a transition between n and n' within a cutting line μ. We only focus our attention to light polarized parallel to the tube or ribbon axis (let us say z axis) because the optical absorption due to the parallel polarization is about 5 times greater than that due to the perpendicular polarization [65].

In the case of parallel polarization, optical transitions can only occur between states with the same angular-momentum quantum number μ. For the photogeneration rate we find

$$\frac{\partial f_{n\mu}(k)}{\partial t} = A_f\, u(t) \sum_{n'} |\mathcal{D}_{nn'}^\mu(k)|^2 \left[f_{n\mu}(k,t) - f_{n'\mu}(k,t) \right]\, \delta\left(\Delta E_{nn'}^\mu(k) - \hbar\omega \right), \tag{3.22}$$

where $\Delta E_{nn'}^{\mu}(k) = |E_{n\mu}(k) - E_{n'\mu}(k)|$ is the k-dependent transition energies and $u(t)$ is the time-dependent energy density of the pump pulse. The prefactor A_f is defined by

$$A_f = \frac{8\pi^2 e^2}{\hbar n_g^2 E_{\mathrm{L}}^2} \left(\frac{\hbar^2}{m_0}\right), \tag{3.23}$$

where e is the electron charge, m_0 is the free electron mass, n_g is the index of refraction in the surrounding medium, and E_{L} is the pump laser energy. The pump energy density $u(t)$ in Eq. (3.22) is related to the pump fluence,

$$F = \int u(t)(c/n_g)\mathrm{d}t. \tag{3.24}$$

It can be assumed that the pump beam consists of a train of N_{pulse} identical Gaussian pulses each with an intensity full width at half maximum (FWHM) of τ_p, which we define as the pump duration. The Gaussian pulses are equally spaced in time with the time interval between pulses being T_{pulse}. The peak intensity of the first pulse is taken to occur at $t = 0$. To account for spectral broadening, we also replace the delta function in Eq. (3.22) by a Lorentzian lineshape with a FWHM of Γ_p.

The optical matrix element for vertical transitions between an initial state $|nk\rangle$ and a final state $|n'k\rangle$ within a cutting line μ is defined as

$$\mathcal{D}_{\mathrm{nn'}}^{\mu} = \frac{\hbar}{\sqrt{2m_0}} \, \hat{\mathbf{P}} \cdot \langle n'k|\nabla|nk\rangle, \tag{3.25}$$

where $\hat{\mathbf{P}}$ is the unit electric polarization vector of light. The state $|nk\rangle$ corresponds to the wavefunction Ψ_{nk} that can be obtained within the extended tight-binding (ETB) framework as discussed in Chapter 2. In coherent phonon spectroscopy, a probe pulse is used to measure the time-varying absorption coefficient of the carbon nanotube. The time-dependent absorption coefficient is given by [66]

$$\alpha(E_{\mathrm{L}}, t) = A_\alpha \sum_{nn'\mu} \int \frac{\mathrm{d}k}{\pi} |\mathcal{M}_{\mathrm{op}}^{nn'\mu}(k)|^2 \left[f_{n\mu}(k,t) - f_{n'\mu}(k,t)\right] \, \delta\left(\Delta E_{nn'}^{\mu}(k) - \hbar\omega\right) \tag{3.26}$$

where the prefactor A_α is defined by

$$A_\alpha = \frac{A_f E_{\mathrm{L}} n_g}{c A_s}. \tag{3.27}$$

In Eq. (3.27), A_f is the same prefactor as that for the photogeneration rate in Eq. (3.22), A_s is the cross-section area of the material (e.g. $\pi(d_t/2)^2$ for a SWNT), and c is the speed of light in vacuum.

It is important to note that the distribution function $f_{n\mu}(k)$ and the band structure $E_{n\mu}(k)$ are time dependent. The time dependence of $f_{n\mu}(k)$ comes from the photogeneration of carriers described by the equation of motion for the photogeneration rate, while the time dependence of $E_{n\mu}(k)$ comes from variations in the carbon-carbon

bond lengths due to the macroscopic coherent phonon induced atomic displacements in Eq. (3.8). This time-dependent deformation of the nanotube or nanoribbon bond lengths alters the tight-binding Hamiltonian and overlap matrix elements in the ETB model. To first order in the lattice displacements, the energies $E_{n\mu}(k)$ vary with time, however, the tight-binding wave functions and optical matrix elements $\mathcal{M}_{\mathrm{op}}^{nn'\mu}(k)$ do not. In coherent phonon spectroscopy, excitation of coherent phonons by the pump modulates the optical properties of the materials giving rise to a transient differential transmission signal. In our model, we take the theoretical coherent phonon signal to be proportional to the power spectrum of the transient differential transmission after background subtraction. We can compute the power spectrum or Fourier transform intensity using some available numerical packages [67].

3.5 Electron-phonon interaction

As can be seen in Eq. (3.20), the electron-phonon interaction determines driving force for the coherent phonon oscillation. The deformation potential electron-phonon interaction between carriers photoexcited by ultrafast laser pulses and the phonon modes is thus responsible for the generation of coherent phonons. The electron-phonon interaction is expressed by a modification to the tight binding parameters by the lattice vibrations in SWNTs and GNRs. In modeling the electron-phonon interaction, we use two different models within the ETB approximation [68] and effective mass theory [69]. The former one is useful to obtain the microscopic driving force term in Eq. (3.20) numerically, while the latter (which is simpler and will be discussed intensively in this work for the SWNT and GNR systems) is used to analytically analyze the dependencies of coherent phonon amplitudes on the excitation energy and on the geometrical structure of SWNTs and GNRs. The results and discussion on coherent phonon amplitudes in SWNTs and GNRs, especially regarding the radial breathing mode (RBM) and radial-breathing-like mode (RBLM) that become the main topics of this thesis, will be covered in Chapter 4.

3.5.1 ETB electron-phonon interaction

To obtain the electron-phonon matrix elements within the ETB approximation, we rewrite the ETB electronic wavefunction as follows [68]:

$$\Psi_{n,\boldsymbol{k}}(\boldsymbol{r}) = \frac{1}{\sqrt{N_u}} \sum_{s,o} C_{s,o}(n,\boldsymbol{k}) \sum_{\boldsymbol{R}_t} e^{i\boldsymbol{k}\cdot\boldsymbol{R}_t} \phi_{t,o}(\boldsymbol{r} - \boldsymbol{R}_t), \qquad (3.28)$$

where n denotes the band index, N_u is the number of hexagons in the unit cell, $s = A$ and B is an index denoting each of the distinct carbon atoms of graphene, and $\boldsymbol{R}_t$ denotes the equilibrium atom positions relative to the origin. Here $\phi_{t,o}$ denotes the atomic wave functions for the orbitals $o = 2s, 2p_x, 2p_y$, and $2p_z$ at $\boldsymbol{R}_t$, respectively.

A lattice vibration with the amplitude of a phonon mode $U(R_t)$ will induce a potential variation δV given by

$$
\begin{aligned}
\delta V &= \sum_{R_t} v[r - R_t - U(R_t)] - v(r - R_t) \\
&\approx -\sum_{R_t} \nabla v(r - R_t) \cdot U(R_t),
\end{aligned}
\tag{3.29}
$$

where v is the Kohn-Sham potential of a neutral pseudo-atom [42]. The electron-phonon matrix element for a certain phonon mode is defined by [68]

$$
\begin{aligned}
\mathcal{M}_{n,k}^{n',k'} &= \langle \Psi_{n',k'}(r)|\delta V|\Psi_{n,k}(r)\rangle \\
&= -\frac{1}{N_u}\sum_{s',o'}\sum_{s,o} C_{s',o'}^*(n',k')C_{s,o}(n,k) \\
&\quad \times \sum_{u',u} e^{i(-k'\cdot R_{u',s'}+k\cdot R_{u,s})}\delta m(t',o',t,o),
\end{aligned}
\tag{3.30}
$$

where $\delta m(t',o',t,o)$ is the atomic deformation potential. To calculate the electron-phonon matrix element of Eq. 3.30 for each phonon mode, the amplitude of the atomic vibration $U(R_t)$ for the phonon mode (m,ν,q) is defined by

$$
U(R_t) = A_{m\nu}(q)\sqrt{\bar{n}_{m\nu}(q)}\,\hat{e}_{m\nu}(R_t)e^{\pm i\omega_{m\nu}(q)t},
\tag{3.31}
$$

where $\pm$ sign is for phonon creation ($+$) and annihilation ($-$), respectively, and $A_{m\nu}$, $\bar{n}_{m\nu}$, $\hat{e}_{m\nu}$, and ω are the phonon amplitude, number, eigenvector, and frequency, respectively. At equilibrium, the phonon number $\bar{n}$ in Eq. (3.31) is determined by the Bose-Einstein distribution function $n_{m\nu}(q)$ for phonons with a frequency $\omega_{m\nu}(q)$,

$$
n_{m\nu}(q) = \frac{1}{e^{\hbar\omega_{m\nu q}/k_B T} - 1},
\tag{3.32}
$$

where $T = 300$ K is the lattice temperature at room temperature and k_B is the Boltzmann constant. For phonon creation, the phonon number $\bar{n} = n + 1$ while for phonon annihilation, $\bar{n} = n$. The amplitude of the zero-point phonon vibration is

$$
A_{m\nu}(q) = \sqrt{\frac{\hbar}{2M_S\omega_{m\nu}(q)}},
\tag{3.33}
$$

and the phonon eigenvector $\hat{e}_{m\nu}(R_t)$ is obtained from solving the dynamical matrix in the phonon dispersion calculation.

The atomic deformation potential δm can be separated into off-site and on-site deformation potentials,

$$
\delta m = \delta m_\alpha + \delta m_\lambda,
\tag{3.34}
$$
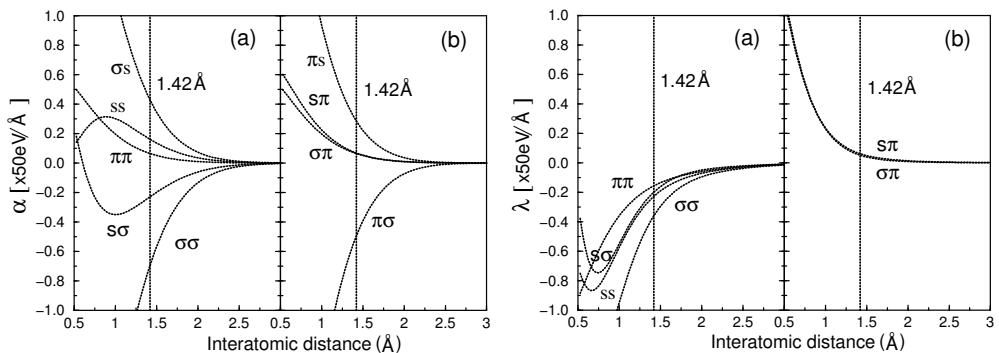
Figure 3.2 (Left) α_p and (Right) λ_p as a function of inter-atomic distance. The vertical line corresponds to 1.42Å which is the C-C distance in graphite [68].

with the off-site and on-site deformation potentials δm_α and δm_λ given by

$$
\begin{aligned}
\delta m_\alpha &= \int \phi_{s',o'}(\boldsymbol{r} - \boldsymbol{R}_{t'}) \left\{ \nabla v(\boldsymbol{r} - \boldsymbol{R}_{t'}) \cdot \boldsymbol{U}(\boldsymbol{R}_{t'}) \right. \\
&\quad + \left. \nabla v(\boldsymbol{r} - \boldsymbol{R}_t) \cdot \boldsymbol{U}(\boldsymbol{R}_t) \right\} \phi_{s,o}(\boldsymbol{r} - \boldsymbol{R}_t) \mathrm{d}\boldsymbol{r}, \\
\delta m_\lambda &= \delta_{\boldsymbol{R}_t, \boldsymbol{R}_{t'}} \int \phi_{s',o'}(\boldsymbol{r} - \boldsymbol{R}_{t'}) \\
&\quad \times \left\{ \sum_{\boldsymbol{R}_{t''} \neq \boldsymbol{R}_{t'}} \nabla v(\boldsymbol{r} - \boldsymbol{R}_{t''}) \cdot \boldsymbol{U}(\boldsymbol{R}_{t''}) \right\} \phi_{s',o}(\boldsymbol{r} - \boldsymbol{R}_{t'}) \mathrm{d}\boldsymbol{r}.
\end{aligned}
\tag{3.35}
$$

The off-site and on-site atomic deformation potentials are, respectively, the corrections to off-diagonal and diagonal Hamiltonian matrix elements and both terms are on the same order of magnitude [70].

When using the Slater-Koster scheme to construct tight-binding Hamiltonian matrix elements between two carbon atoms [42], the carbon $2p$ orbitals are chosen to be along or perpendicular to the bond connecting the two atoms. The four fundamental hopping and overlap integrals are (ss), $(s\sigma)$, $(\sigma\sigma)$, and $(\pi\pi)$. We follow the same procedure as was used to construct the deformation potential matrix elements $\langle \phi | \nabla v | \phi \rangle$. We introduce the matrix elements,

$$
\begin{aligned}
\alpha_p(\boldsymbol{\tau}) &= \int \phi_\mu(\boldsymbol{r}) \nabla v(\boldsymbol{r}) \phi_\nu(\boldsymbol{r} - \boldsymbol{\tau}) \mathrm{d}\boldsymbol{r} = \alpha_p(\tau) \hat{I}(\alpha_p), \\
\lambda_p(\boldsymbol{\tau}) &= \int \phi_\mu(\boldsymbol{r}) \nabla v(\boldsymbol{r} - \boldsymbol{\tau}) \phi_\nu(\boldsymbol{r}) \mathrm{d}\boldsymbol{r} = \lambda_p(\tau) \hat{I}(\lambda_p),
\end{aligned}
\tag{3.36}
$$

where $\hat{I}(\alpha_p)$ and $\hat{I}(\lambda_p)$ are unit vectors describing the direction of the off-site and on-site deformation potential vectors α_p and λ_p, respectively, and $p = \mu\nu$. The $2p$ orbital ϕ_μ (ϕ_ν) is along or perpendicular to the bond connecting the two carbon atoms and

Fig. 3.2: fig/fch3-matel.eps

τ is the distance between the two atoms. From α_p, we can also obtain another matrix element,

$$
\begin{aligned}
\beta_p(\tau) &= \int \phi_\mu(\boldsymbol{r}) \nabla v(\boldsymbol{r} - \boldsymbol{\tau}) \phi_\nu(\boldsymbol{r} - \boldsymbol{\tau}) \mathrm{d}\boldsymbol{r} \\
&= \int \phi_\nu(\boldsymbol{r}) \nabla v(\boldsymbol{r}) \phi_\mu(\boldsymbol{r} + \boldsymbol{\tau}) \mathrm{d}\boldsymbol{r} = \beta_p(\tau) \hat{I}(\beta_p).
\end{aligned}
\tag{3.37}
$$

However, the integral in Eq. (3.37) can be expressed by α terms. In Fig. 3.2, the calculated values of α_p and λ_p are plotted as a function of inter-atomic distance between two carbon atoms [68]. At $r = 1.42$Å, the bond length between a carbon atom and one of its nearest neighbors, we have $\alpha_{\pi\pi} \approx 3.2$eV/Å and $|\lambda_{\pi\pi}| \approx 7.8$eV/Å, and $|\alpha_{\pi\sigma}| \approx 24.9$eV/Å.

3.5.2   Effective mass theory

We can also calculate the electron-phonon matrix elements by using effective mass theory. Indeed, considering the effective mass theory allows us to analyze the trend of coherent phonon amplitudes of SWNTs and GNRs more clearly. Here we derive a specific Hamiltonian needed to calculate the electron-phonon matrix elements in SWNTs and GNRs [69, 13]. The results will be shown later in Chapter 4

The electron-phonon Hamiltonian in effective mass theory for graphene-related systems basically can be decomposed into the on-site and off-site Hamiltonians,

$$
H_{\mathrm{ep}} = \mathcal{H}_{\mathrm{on}} + \mathcal{H}_{\mathrm{off}}.
\tag{3.38}
$$

The details of the on-site and off-site interactions are given in Appendix B, following Sasaki's work on the deformation-induced gauge field in graphene [71]. We will directly use the results in formulating the on-site and off-site Hamiltonians. The on-site and off-site interactions are induced by a lattice deformation which gives rise to a change in the transfer integral and a change in the potential between A and B atoms in the graphene unit cell. In order to derive H_{ep} within effective mass theory for SWNTs and GNRs, we adopt a coordinate system shown in Fig. 3.3

The on-site Hamiltonian can be expressed in terms of the divergence of u_{A} and u_{B}, which represent the displacement vector of A-atom and B-atom in the graphene unit cell, respectively. This Hamiltonian is written as [71]

$$
\mathcal{H}_{\mathrm{on}} = g_{\mathrm{on}} \begin{pmatrix} \nabla \cdot u_{\mathrm{B}}(\mathbf{r}) & 0 \\ 0 & \nabla \cdot u_{\mathrm{A}}(\mathbf{r}) \end{pmatrix}.
\tag{3.39}
$$

For the discussion of the RBM and RBLM electron-phonon interactions in SWNTs and GNRs, we rewrite (3.39) as follows:

$$
\mathcal{H}_{\mathrm{on}} = g_{\mathrm{on}} \left[\sigma_0 \nabla \cdot \left(\frac{u_{\mathrm{A}}(\mathbf{r}) + u_{\mathrm{B}}(\mathbf{r})}{2} \right) + \sigma_z \nabla \cdot \left(\frac{u_{\mathrm{A}}(\mathbf{r}) - u_{\mathrm{B}}(\mathbf{r})}{2} \right) \right],
\tag{3.40}
$$
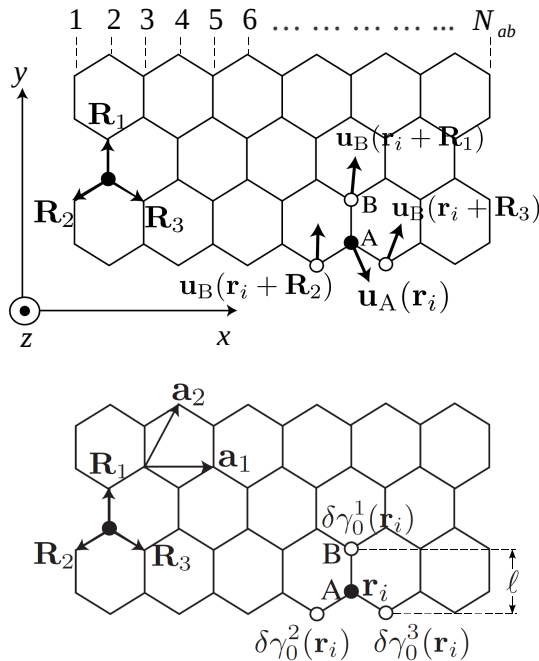
Figure 3.3 Upper panel shows displacements of B-atoms at $\mathbf{r}_i + \mathbf{R}_a$ ($a = 1, 2, 3$), that is $\mathbf{u}_B(\mathbf{r}_i + \mathbf{R}_a)$, which give rise to a deformation potential at A-atom of $\mathbf{r}_i$. Lower panel shows local modulations of the hopping integral defined by $\delta\gamma_0^a(\mathbf{r})$ ($a = 1, 2, 3$). In this coordinate system we have the nearest-neighbor vectors $\mathbf{R}_1 = (0, a_{CC})$, $\mathbf{R}_2 = (-\sqrt{3}/2, -1/2)a_{CC}$, $\mathbf{R}_3 = (\sqrt{3}/2, -1/2)a_{CC}$, where $a_{CC} = a/\sqrt{3}$. Here $\ell = 3a_{CC}/2$ is used in Eq. (3.47).

where g_{on} denotes the gradient of the atomic potential at $\mathbf{r}$ (here we use the constant $g_{on} = 17.0\,\text{eV}$ as obtained from a first-principle calculation [42]), σ_0 is the identity matrix, and σ_z is the z-component of the vector of Pauli matrices. Although RBM and RBLM are optic phonon modes, but on the planar graphene they are actually formed from the out-of-plane acoustic and in-plane acoustic phonon modes of graphene, respectively. In these cases, we have $u_A(\mathbf{r}) = u_B(\mathbf{r}) = \mathbf{u}(\mathbf{r})$. Therefore, Eq (3.40) can be simplified to be

$$\mathcal{H}_{on} = g_{on}\sigma_0\nabla \cdot u(r). \tag{3.41}$$

Let $\nabla \cdot u(r) = u_{ph}$, we can write Eq. (3.41) as

$$\mathcal{H}_{on} = u_{ph}\begin{pmatrix} g_{on} & 0 \\ 0 & g_{on} \end{pmatrix}. \tag{3.42}$$

In Eq. (3.42), u_{ph} is a dimensionless parameter determined by the type of vibrations. For example, in the case of RBM oscillation in a zigzag nanotube, u_{ph} is found to be

Fig. 3.3: fig/fch3-graphenedef.eps

$2s_r/d_t$, where $s_r = \sqrt{\hbar/2M_s\omega_{\mathrm{RBM}}}$ is the phonon amplitude for the RBM [12, 69] and M_s is total mass of carbon atoms in the unit cell.

Next, to derive the off-site interaction Hamiltonian, we start with the fact that the lattice deformation modifies the nearest-neighbor hopping integral locally as $-\gamma_0 \to -\gamma_0 + \delta\gamma_0^a(\mathbf{r}_i)$ ($a = 1, 2, 3$). The corresponding perturbation of the lattice deformation is given by

$$\mathcal{H}_{\mathrm{off}} \equiv \sum_{i \in \mathrm{A}} \sum_{a=1,2,3} \delta\gamma_0^a(\mathbf{r}_i) \left[(c_{i+a}^{\mathrm{B}})^\dagger c_i^{\mathrm{A}} + (c_i^{\mathrm{A}})^\dagger c_{i+a}^{\mathrm{B}} \right], \tag{3.43}$$

where c_i^{A} is the annihilation operator for a π electron on an A-atom at position $\mathbf{r}_i$, and $(c_{i+a}^{\mathrm{B}})^\dagger$ is the creation operator for a π electron on a B-atom at position $\mathbf{r}_{i+a}$ ($= \mathbf{r}_i + \mathbf{R}_a$). This perturbation gives rise to scattering within a region near the K point of graphene whose interaction is given by a deformation-induced gauge field $\mathbf{A}(\mathbf{r}) = (A_x(\mathbf{r}), A_y(\mathbf{r}))$ as

$$\mathcal{H}_{\mathrm{off}} = v_{\mathrm{F}}\sigma \cdot \mathbf{A}(\mathbf{r}), \tag{3.44}$$

where $v_{\mathrm{F}} = 3\gamma_0 a_{\mathrm{CC}}/2\hbar$ ($\sim 10^6$ m/s) is the Fermi velocity and σ is the Pauli matrix. The deformation-induced gauge field $\mathbf{A}(\mathbf{r})$ for the off-site interaction is defined from $\delta\gamma_0^a(\mathbf{r})$ ($a = 1, 2, 3$) as (see also Appendix B)

$$v_{\mathrm{F}} A_x(\mathbf{r}) \quad = \quad \delta\gamma_0^1(\mathbf{r}) - \frac{1}{2}\left[\delta\gamma_0^2(\mathbf{r}) + \delta\gamma_0^3(\mathbf{r}) \right], \tag{3.45}$$

$$v_{\mathrm{F}} A_y(\mathbf{r}) \quad = \quad \frac{\sqrt{3}}{2}\left[\delta\gamma_0^2(\mathbf{r}) - \delta\gamma_0^3(\mathbf{r}) \right]. \tag{3.46}$$

The perturbation to the nearest-neighbor hopping integral for the RBM and RBLM electron-phonon interactions is given by

$$\delta\gamma_0^a(\mathbf{r}) = \frac{g_{\mathrm{off}}}{\ell a_{\mathrm{CC}}} \mathbf{R}_a \cdot \{\mathbf{u}(\mathbf{r} + \mathbf{R}_a) - u(r)\}, \tag{3.47}$$

where g_{off} is the off-site coupling constant ($g_{\mathrm{off}} = 6.4\,\mathrm{eV}$) and $\ell = 3a_{\mathrm{CC}}/2$ (see the lower panel of Fig. 3.3). Here the displacement vector of a carbon atom at $\mathbf{r}$ in general is expressed by $u(r) = [u_x(\mathbf{r}), u_y(\mathbf{r})]$. Using a Taylor expansion, we approximate equation (3.47) as

$$\delta\gamma_0^a(\mathbf{r}) = \frac{g_{\mathrm{off}}}{\ell a_{\mathrm{CC}}} \mathbf{R}_a \cdot \{(\mathbf{R}_a \cdot \nabla)u(r)\}. \tag{3.48}$$

Using $\mathbf{R}_1$, $\mathbf{R}_2$, and $\mathbf{R}_3$ in Fig. 3.3, we obtain the deformation-induced gauge field of equations (3.45) and (3.46) as follows:

$$v_{\mathrm{F}} A_x(\mathbf{r}) \quad = \quad -\frac{g_{\mathrm{off}}}{2}\left[\frac{\partial u_x(\mathbf{r})}{\partial x} + \frac{\partial u_y(\mathbf{r})}{\partial y} \right], \tag{3.49}$$

$$v_{\mathrm{F}} A_y(\mathbf{r}) \quad = \quad \frac{g_{\mathrm{off}}}{2}\left[\frac{\partial u_x(\mathbf{r})}{\partial y} + \frac{\partial u_y(\mathbf{r})}{\partial x} \right]. \tag{3.50}$$

It can be derived that $v_F A_y = 0$ for both RBM and RBLM cases [13, 69]. Therefore, the off-site Hamiltonian can be written as

$$\mathcal{H}_{\text{off}} = \sigma_x v_F A_x = u_{\text{ph}} \begin{pmatrix} 0 & -\dfrac{g_{\text{off}}}{2} \\ -\dfrac{g_{\text{off}}}{2} & 0 \end{pmatrix}. \tag{3.51}$$

Finally, we can get the electron-phonon Hamiltonian of Eq. (3.38),

$$H_{\text{ep}} = \mathcal{H}_{\text{on}} + \mathcal{H}_{\text{off}} = u_{\text{ph}} \begin{pmatrix} g_{\text{on}} & -\dfrac{g_{\text{off}}}{2} \\ -\dfrac{g_{\text{off}}}{2} & g_{\text{on}} \end{pmatrix}. \tag{3.52}$$

To obtain the electron-phonon matrix elements based on effective mass theory, we use the following two wavefunctions,

$$\Psi_{\text{c}} = \frac{e^{i\boldsymbol{k}\cdot\boldsymbol{r}}}{\sqrt{2S}} \begin{pmatrix} e^{-i\Theta(\boldsymbol{k})/2} \\ e^{+i\Theta(\boldsymbol{k})/2} \end{pmatrix}, \Psi_{\text{v}} = \frac{e^{i\boldsymbol{k}\cdot\boldsymbol{r}}}{\sqrt{2S}} \begin{pmatrix} e^{-i\Theta(\boldsymbol{k})/2} \\ -e^{+i\Theta(\boldsymbol{k})/2} \end{pmatrix}, \tag{3.53}$$

for conduction and valence states, respectively, where S is the surface area of graphene and $\Theta(\boldsymbol{k})$ is an angle of $\mathbf{k} = (\mathbf{k}_x, \mathbf{k}_y)$ measured from the k_x-axis. Depending on the geometry of the materials, we may also redefine $\Theta(\boldsymbol{k})$ with respect to another reference, which we will do for the case of SWNT and GNR systems. We will further clarify the behavior of electron phonon matrix elements for SWNT and GNRs within effective mass theory in Chapter 4 when discussing the excitation- and structural-dependencies of the coherent phonon amplitudes.

Chapter 4

Coherent phonon amplitudes in SWNTs and GNRs

Using the concepts we have developed in Chapter 3, we are now able to investigate coherent phonon properties in a variety of graphene systems. In this chapter, we show and discuss simulation results based on extended-tight binding (ETB) method for the ultrafast dynamics of laser-induced coherent phonons in single wall carbon nanotubes (SWNTs) and graphene nanoribbons (GNRs). In particular, we examine the coherent radial breathing mode (RBM) amplitudes of SWNTs and the coherent radial breathing like mode (RBLM) amplitudes of GNRs as a function of excitation energy and chirality. The coherent phonon amplitudes give direct information on initial oscillation phase so that we can directly know whether the diameter (width) of a given SWNT (GNR) in the RBM (RBLM) will initially increase or decrease at a certain excitation energy. We find that the coherent phonon amplitudes are very sensitive to the changes in excitation energy and are strongly structure dependent. An effective-mass theory for the electron-phonon interaction gives a physical explanation for these phenomena.

4.1 Coherent RBM phonons in SWNTs

As discussed earlier in Chapter 3, the coherent RBM phonon amplitude Q with frequency ω satisfies a driven oscillator equation (3.17), which we now rewrite using simpler notations (see Ref. [12]),

$$\frac{\partial^2 Q(t)}{\partial t^2} + \omega^2 Q(t) = S(t), \tag{4.1}$$

subject to the initial conditions $Q(0) = 0$ and $\dot{Q}(0) = 0$. Here $S(t)$ is the driving function which depends on the photoexcited carrier distribution function and is given

by

$$S(t) = -\frac{2\omega}{\hbar} \sum_{\mu k} \mathcal{M}_\mu^{\mathrm{ep}}(k) \delta f_\mu(k, t), \qquad (4.2)$$

where $\mathcal{M}_\mu^{\mathrm{ep}}(k)$ is the k-dependent RBM electron-phonon matrix element for the μ-th cutting line (1D Brillouin zone of a SWNT) and δf_μ is the net photogenerated electron distribution function with a pump pulse pumping at the E_{ii} transition energy as obtained by solving a Boltzmann equation for the photogeneration process. The photogeneration rate in the Boltzmann equation depends on the excitation laser energy [11]; it also contains the electron-photon matrix element $\mathcal{D}^{\mathrm{op}}$ for the case of light polarized along the tube axis, so that we have the proportionality

$$\delta f_\mu \propto |\mathcal{D}_\mu^{\mathrm{op}}|. \qquad (4.3)$$

For the calculation of electron-phonon and electron-photon interactions, we incorporate SWNT electronic energies and wave functions obtained from the ETB method [43], and the phonon dispersions from the force constant model [47].

In a typical simulation, the necessary inputs are the excitation energy, E_{laser}, and the chiral index, (n, m). We will mainly use the $(11, 0)$ and $(13, 0)$ semiconducting zigzag nanotubes as examples for discussing the excitation and chirality dependence of the RBM coherent phonon amplitudes. Though the main examples studied in this work are semiconducting SWNTs, the theory is also valid for metallic SWNTs. It will be shown later that the chirality dependence of the coherent phonon amplitude between different nanotube types has the same origin. For a given excitation energy, we solve Eq. (5.3) for a specific SWNT to obtain the coherent RBM phonon amplitude oscillating at the RBM frequency. We use the same common input parameters for the pump-probe setup as those used in Ref. [11], i.e. we excite the RBM phonons with a single 50 fs laser pulse, where the pump fluence is taken to be 10^{-5} J/cm^2, and the FWHM spectral linewidth is assumed to be 0.15 eV. Note that here the pump and probe energies are considered to be the same. Therefore, this setup should not be confused with an experimental setup discussed in Chapter 1 (Fig. 1.6), in which the probe energy is varied for a constant pump energy and leads to another type of coherent phonon phase shift related to the phase change near the resonance.

In this part we also do not consider excitonic effects because we will not discuss the peak positions or line shapes of the coherent phonon spectra. For such discussions, the excitonic effects cannot be neglected since the E_{ii} energies are shifted from those calculated within a single particle picture [72, 62], and these will be the main subject in Chapter 5. In the present chapter, we only explain macroscopic SWNT lattice response which is homogeneous along the tube axis. Therefore, considering only the electron-phonon interaction is sufficient.
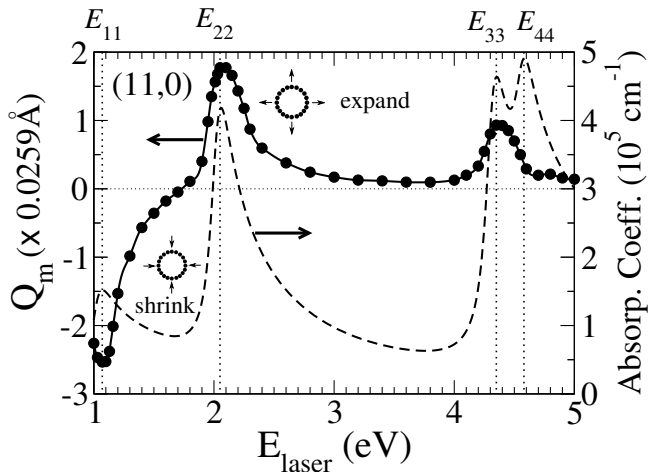
Figure 4.1 The coherent RBM phonon amplitude Q_m for an $(11,0)$ zigzag tube as a function of laser excitation energy E_{laser}. For clarity, Q_m is plotted in units of 0.0259. A positive (negative) sign of the vibration amplitude denotes a vibration whose initial phase corresponds to an expanding (shrinking) diameter. The absorption coefficient versus E_{laser} is shown for comparison with the Q_m behavior.

4.1.1 Excitation energy dependence

Let us firstly discuss excitation energy dependence of the coherent RBM phonon amplitudes. In Fig. 4.1, we plot the coherent RBM phonon amplitude Q_m in an $(11,0)$ nanotube at an early time, along with the absorption coefficient as a function of E_{laser}. Here Q_m can be imagined by roughly defining $Q(t) = Q_m \cos \omega t$, where the origin of time is now indicated by the first maximum (minimum) of $Q(t)$ found after $t = 0$ for a positive (negative) coherent phonon vibration. Therefore, in this definition, $Q_m > 0$ and $Q_m < 0$ correspond to the tube diameter expansion and contraction, respectively.

From Fig. 4.1, we see that the pump light is strongly absorbed at the E_{ii} energies. The resulting increase in the number of photoexcited carriers increases the coherent phonon driving function $S(t)$ in Eq. (4.2) and thus enhances the coherent phonon oscillation amplitude near the E_{ii} transitions. Note that at E_{11} the amplitude has a negative sign, indicating that the tube diameter initially shrinks and oscillates about a smaller diameter, while at E_{22} and higher energies (e.g., E_{33} or E_{44}) the tube diameter initially expands and oscillates about a larger diameter. According to a common concept based on the Franck-Condon principle, solid lattices usually tend to expand in the presence of ultrafast carrier photoexcitation since the electronic excited states are anti-bonding states. When an electron is excited, it will try to find a new equilibrium position at the minimum of the excited anti-bonding state energy. This minimum energy is located at a larger coordinate than that of the ground state, and

Fig. 4.1: fig/fch4-cpamp1100.eps

thus the lattice expands. However, this is not always the case for RBM coherent phonons in the SWNT system, where the tube diameter can either expand or contract depending on the excitation energy.

In order to understand this phenomenon, we consider the magnitude and phase of the oscillation amplitude $Q(t)$ driven by $S(t)$ in Eq. (4.2). First, since $\delta f \propto |\mathcal{D}^{\mathrm{op}}|$ as in Eq. (4.3), the magnitude of oscillations should be proportional to the product of the electron-phonon and electron-photon matrix elements:

$$|Q| \propto |\mathcal{M}^{\mathrm{ep}}||\mathcal{D}^{\mathrm{op}}|. \tag{4.4}$$

Second, according to Eq. (4.2) and noting that $\delta f_{\mu}(k)$ is positive for most cases of interest (*i.e.* no gain in the system), the initial phase of $Q(t)$ is only determined by the sign of $\mathcal{M}_{\mu}^{\mathrm{ep}}(k)$ summed over all cutting lines μ and all k points. The unique values of $|\mathcal{M}^{\mathrm{ep}}|$ and $|\mathcal{D}^{\mathrm{op}}|$ for a fixed selection of energy and (n, m) then determines the excitation energy and chirality dependence of the coherent phonon amplitudes.

4.1.2   Chirality dependence

Let us now discuss the type dependence or chirality dependence of coherent RBM phonon amplitudes by comparing two semiconducting zigzag nanotubes of different families and types. In Fig. 4.2, we plot the electron-phonon matrix elements for RBM coherent phonons in the $(11, 0)$ (type-I) and $(13, 0)$ (type-II) nanotubes as a function of 1D wavevector k. The k dependence of $\mathcal{M}_{\mu}^{\mathrm{ep}}(k)$ for the RBM phonon is shown for the first two cutting lines, for E_{11} and E_{22}. As can be seen in the figure, both positive and negative values of $\mathcal{M}_{\mu}^{\mathrm{ep}}(k)$ are possible. Also, according to Eq. (4.2), if we pump near the E_{ii} band edge, the electron distributions would be localized near $k = 0$ in the 1D Brillouin zone of the zigzag nanotubes, for which the k_{ii} points for the E_{ii} energies lie at $k = 0$. Therefore, the positive (negative) values of $S(t)$ at the E_{22} (E_{11}) transition energy are determined by the negative (positive) value of $\mathcal{M}_{\mu}^{\mathrm{ep}}(k)$ near $k = 0$.

For the two nanotubes, the signs of the electron-phonon matrix elements differ at E_{11} and E_{22}. The reason is that for type-I and type-II nanotubes the E_{11} and E_{22} cutting line positions with respect to the K-point in the 2D graphene Brillouin zone are opposite to each other [73]. Depending on the cutting line positions relative to the K-point, the corresponding $\mathcal{M}_{\mu}^{\mathrm{ep}}(k)$ for a given cutting line is negative in the region to the right of the K-point and positive in the region to the left [74]. This will be proved in the next section using an effective-mass theory. From this argument, we predict that the type-I (type-II) zigzag nanotubes would start their coherent RBM phonon oscillations by initially decreasing (increasing) the tube diameter at E_{11}, while at E_{22} the behavior is just the opposite, as shown in Fig. 4.2.
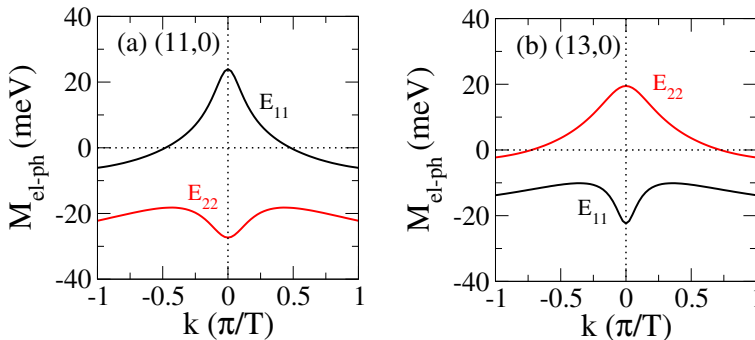
Figure 4.2 RBM electron-phonon matrix elements of (a) $(11,0)$ and (b) $(13,0)$ zigzag nanotubes within the ETB approximation.

4.1.3 Analysis by the effective mass theory

Since the electron-phonon matrix element determines the initial lattice response of the SWNTs, we further decompose $\mathcal{M}^{\mathrm{ep}}$ into its electron and hole components for each SWNT in order to understand which component gives a significant contribution to the ETB matrix element $\mathcal{M}^{\mathrm{ep}}$. This electron-phonon matrix element for the photo-excited electron is basically a sum of conduction band (c) and valence band (v) electron-phonon matrix elements, which represent the electron and hole contributions, respectively [74],

$$\mathcal{M}^{\mathrm{ep}}(k) = \mathcal{M}^{\mathrm{ep}}(k_{\mathrm{c}}) - \mathcal{M}^{\mathrm{ep}}(k_{\mathrm{v}})$$
$$= \langle \mathrm{c}|H_{\mathrm{ep}}|\mathrm{c}\rangle - \langle \mathrm{v}|H_{\mathrm{ep}}|\mathrm{v}\rangle, \tag{4.5}$$

where H_{ep} is the SWNT electron-phonon interaction Hamiltonian.

In Fig. 4.3, we plot the electron and hole components of $\mathcal{M}^{\mathrm{ep}}$ in the ETB model as a function of the 1D wavevector k. If we compare the contributions from each component, we see that in the $(11,0)$ tube the electron (hole) component gives a larger contribution to $\mathcal{M}^{\mathrm{ep}}$ at E_{11} (E_{22}). On the other hand, in the $(13,0)$ tube, the hole (electron) component gives a larger contribution to $\mathcal{M}^{\mathrm{ep}}$ at E_{11} (E_{22}). We can analyze these results within an effective-mass theory. Using the effective-mass theory, we can obtain a simple analytical expression explaining the sign of the SWNT electron-phonon matrix elements, which can then be compared with the ETB results.

In a nearest-neighbor effective-mass approximation, the RBM H_{ep} for an (n,m) SWNT with a chiral angle θ and diameter d_t can be written as [69],

$$H_{\mathrm{ep}} = \frac{2s_r}{d_t} \begin{pmatrix} g_{\mathrm{on}} & -\frac{g_{\mathrm{off}}}{2}\mathrm{e}^{i3\theta} \\ -\frac{g_{\mathrm{off}}}{2}\mathrm{e}^{-i3\theta} & g_{\mathrm{on}} \end{pmatrix}, \tag{4.6}$$

Fig. 4.2: fig/fch4-elphETB.eps
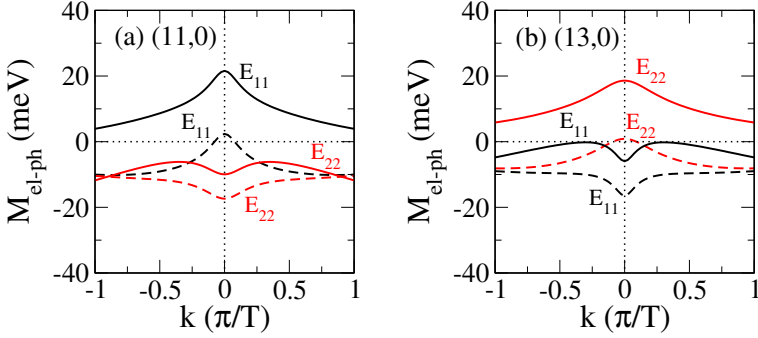
Figure 4.3 Electron and hole components of the ETB $\mathcal{M}^{\mathrm{ep}}$ shown by solid and dashed lines, respectively, for (a) $(11,0)$ and (b) $(13,0)$ zigzag nanotubes, as a function of k. The matrix elements for E_{11} and E_{22} are shown in black and red, respectively.

where g_{on} (g_{off}) is the on-site (off-site) coupling constant. Here $s_r = \sqrt{\hbar/2M\omega_{\mathrm{RBM}}}$ is the phonon amplitude for the RBM, where ω_{RBM} is the phonon frequency and M is the total mass of the carbon atoms within the unit cell. To obtain $\mathcal{M}^{\mathrm{ep}}$ in Eq. (4.5), we adopt the following two wavefunctions,

$$\Psi_{\mathrm{c}} = \frac{e^{i\boldsymbol{k}\cdot\boldsymbol{r}}}{\sqrt{2S}}\begin{pmatrix} e^{-i\Theta(\boldsymbol{k})/2} \\ e^{+i\Theta(\boldsymbol{k})/2} \end{pmatrix}, \Psi_{\mathrm{v}} = \frac{e^{i\boldsymbol{k}\cdot\boldsymbol{r}}}{\sqrt{2S}}\begin{pmatrix} e^{-i\Theta(\boldsymbol{k})/2} \\ -e^{+i\Theta(\boldsymbol{k})/2} \end{pmatrix}, \tag{4.7}$$

for conduction and valence states, respectively, which are suitable near the graphene K-point [69]. In Eq. (4.7), S is the surface area of graphene and $\Theta(\boldsymbol{k})$ is an angle at the K-point measured from a line perpendicular to the cutting lines (see Fig. 4.4).

By inserting the wavefunctions in Eq. (4.7) into Eq. (4.5), we obtain

$$+\langle \mathrm{c}|H_{\mathrm{ep}}|\mathrm{c}\rangle = \frac{s_r}{d_t}\left(-g_{\mathrm{off}}\cos(\Theta(\boldsymbol{k})+3\theta)+2g_{\mathrm{on}}\right), \tag{4.8a}$$

$$-\langle \mathrm{v}|H_{\mathrm{ep}}|\mathrm{v}\rangle = \frac{s_r}{d_t}\left(-g_{\mathrm{off}}\cos(\Theta(\boldsymbol{k})+3\theta)-2g_{\mathrm{on}}\right), \tag{4.8b}$$

and thus

$$\mathcal{M}^{\mathrm{ep}} = \frac{s_r}{d_t}\left(-2g_{\mathrm{off}}\cos(\Theta(\boldsymbol{k})+3\theta)\right). \tag{4.9}$$

From Eqs. (4.8a) and (4.8b), it is clear that the electron and hole contributions to $\mathcal{M}^{\mathrm{ep}}$ are simply distinguished by the off-site and on-site interactions. These equations are thus qualitatively consistent with the results in Fig. 4.3. According to the density-functional calculation by Porezag *et al.* [42], we adopt the off-site coupling constant $g_{\mathrm{off}} = 6.4\,\mathrm{eV}$ and the on-site coupling constant $g_{\mathrm{on}} = 17.0\,\mathrm{eV}$, which are calculated for the first nearest-neighbor carbon-carbon distance [69]. However, g_{on} has no effect on the electron-phonon matrix element since it vanishes in Eq. (4.9). The more accurate treatment for the effective-mass theory should consider the asymmetry between the

Fig. 4.3: fig/fch4-elphsep.eps
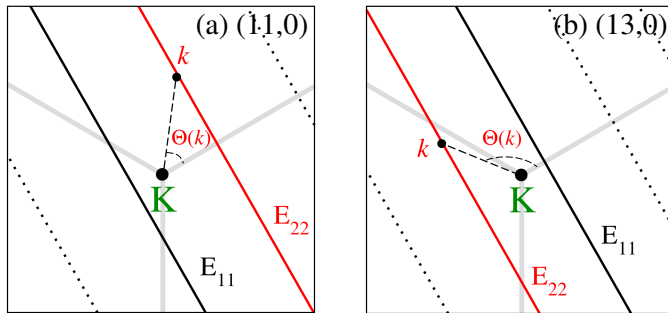
Figure 4.4 Cutting lines for (a) (11,0) and (b) (13,0) zigzag nanotubes near the graphene K-point. Solid lines denote the E_{11} and E_{22} cutting lines, while the dotted lines correspond to higher cutting lines. The angle $\Theta(\boldsymbol{k})$ is measured counterclockwise from a line perpendicular to the cutting lines, where the positive direction of the line is to the right of the K-point. Here $\Theta(\boldsymbol{k})$ is shown for a k point on the E_{22} cutting line for both SWNTs. The difference between the type-I and type-II families can be understood from the position of the E_{11} or E_{22} cutting lines relative to the K-point [73].

valence bands and the conduction bands [75]. Within the present model, we do not consider such an asymmetry since the chirality dependence of the electron-phonon matrix element can readily be described by the $\cos(\Theta(\boldsymbol{k}))$ term, which will give a positive or negative sign in front of g_{off}.

In Fig. 4.5, we then plot the matrix elements of Eq. (4.9) for the $(11, 0)$ and $(13, 0)$ nanotubes, where the on-site term (g_{on}) disappears and only the off-site term (g_{off}) contributes to $\mathcal{M}^{\text{ep}}$. It can be seen that the effective-mass theory (see Figs. 4.5(a) and (b)) nicely reproduces the ETB calculation results near $k_{ii} = 0$ (see Figs. 4.2(a) and (b)). However, the first nearest-neighbor effective-mass model cannot reproduce the ETB matrix element results at k far from $k_{ii} = 0$. We can see this since at E_{11} and E_{22} $\mathcal{M}^{\text{ep}}$ are almost symmetric around $\mathcal{M}^{\text{ep}} = 0$ in Figs. 4.5(a) and (b) but the $\mathcal{M}^{\text{ep}}$ are not symmetric in Figs. 4.2(a) and (b). In Fig. 4.5(c), we show $\mathcal{M}^{\text{ep}}$ for the $(11, 0)$ tube within the ETB model considering interactions up to the fourth nearest-neighbors. Based on this figure, we consider that the exact $\mathcal{M}^{\text{ep}}$ analytical expression at k far from the k_{ii} should take into account the longer-range electron-phonon interactions. Nevertheless, the first nearest-neighbor effective-mass theory has already given physical insight into the k-dependent $\mathcal{M}^{\text{ep}}$, and considering the approximation up to the fourth nearest-neigbors is sufficient to converge the $\mathcal{M}^{\text{ep}}$ values.

For the zigzag nanotubes, Eq. (4.9) also explains the dependence of $\mathcal{M}^{\text{ep}}$ on the cutting line (or $\boldsymbol{k}$) position. Let us take the examples in Fig. 4.4, in which we show the cutting lines for the $(11, 0)$ and $(13, 0)$ nanotubes. The E_{22} cutting line for the $(11, 0)$ $((13, 0))$ tube is to the right (left) of the K-point, giving a positive (negative)

Fig. 4.4: fig/fch4-cntcutline.eps
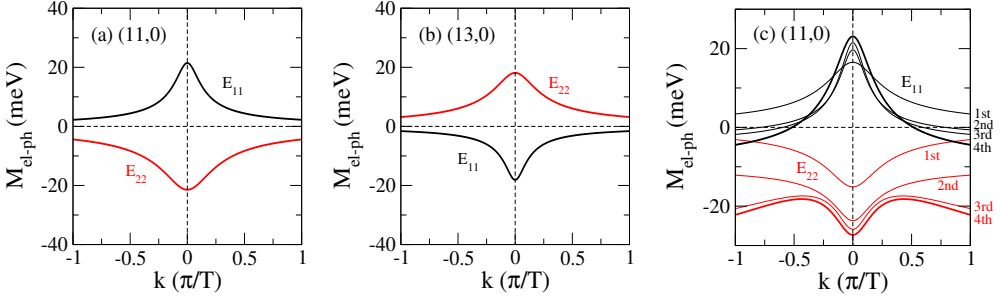
Figure 4.5 RBM electron-phonon matrix elements of (a) $(11,0)$ and (b) $(13,0)$ nanotubes calculated within the effective-mass theory using $g_{\text{off}} = 6.4\,\text{eV}$. In panels (a) and (b), the matrix elements near $k = 0$ are comparable with the results in Fig. 4.2. Panel (c) shows the matrix elements of an $(11,0)$ nanotube calculated within the ETB model for interactions up to the fourth nearest-neighbors. The results including fourth nearest neighbors exactly reproduce the results in Fig. 4.2.(a).

$\cos(\Theta(\boldsymbol{k}))$ and thus a negative (positive) $\mathcal{M}^{\text{ep}}$ for the E_{22} transition. According to Eq. (4.2), the negative (positive) $\mathcal{M}^{\text{ep}}$ corresponds to the initial increase (decrease) of the tube diameter. In such a way, the chirality dependence of the coherent phonon amplitude is simply determined by the electron-phonon interaction.

However, we should note that the simple rule does not work well for E_{33} and E_{44}, as can be seen in Fig. 4.1. For instance, the coherent phonon amplitude at E_{33} has the same sign as that at E_{22} although their cutting line positions are opposite to each other with respect to the K-point. The reason for the breakdown of this simple rule is that the cutting lines for E_{33} and E_{44} are far from the K-point so that the wavefunctions of Eq. (4.7) are no longer good approximations. In this case, the ETB wavefunctions are necessary for obtaining the coherent phonon amplitudes.

4.1.4   Map of the coherent phonon amplitudes

To consider the more general family behavior of the RBM coherent phonon amplitudes, we recalculate Q_{m} using the ETB method for 33 different SWNT chiralities with diameters of $0.7 - 1.1\,\text{nm}$ and for photoexcitations at E_{ii} in the range $1.5 - 3.0\,\text{eV}$. The results are shown in Fig. 4.6. Note that in addition to the semiconducting SWNTs, we also give some results for metallic SWNTs. It is known that the density of states for E_{ii} in metallic SWNTs are split into the lower E_{ii}^{L} and higher E_{ii}^{H} branches, except for the armchair SWNTs [26]. Here we consider Q_{m} in metallic SWNTs only at E_{11}^{L}. The cutting line for E_{11}^{L} is located to the right of the K-point. We can see in Fig. 4.6 that all the metallic SWNTs start vibrations by increasing their diameter at E_{11}^{L}. The reason is the same as in type-II nanotubes, where the cutting lines for the E_{11} transitions are located to the right of the K-point, giving a negative $\mathcal{M}^{\text{ep}}$ (hence a positive Q_{m}) as
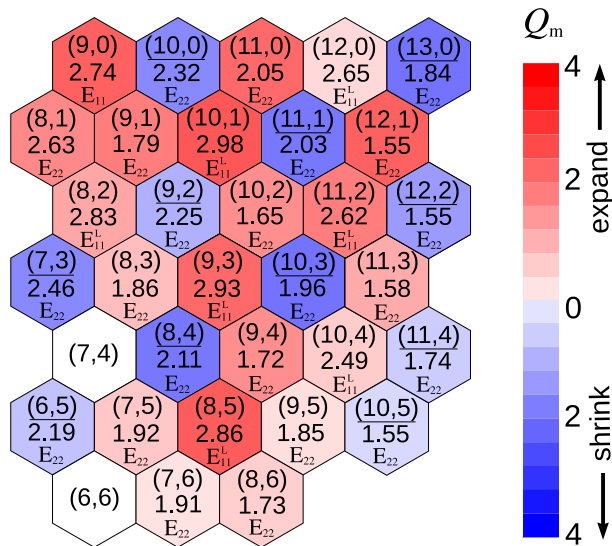
Figure 4.6 The lattice response of SWNTs with diameters in the range $0.7 - 1.1\,\text{nm}$ is mapped onto the unrolled graphene lattice specifiying the tube chiralities (n, m). In this map Q_m is expressed in terms of $\sqrt{\hbar/2M\omega_{\text{RBM}}}$. Red and blue colored hexagons denote the SWNTs whose vibrations start by increasing or decreasing their diameter, respectively. The laser excitation energies are selected within the range $1.5 - 3.0\,\text{eV}$. For each (n, m) tube, the corresponding E_{ii} (in eV) found within this energy region is listed on each hexagon with the label E_{ii}. The calculated results for the $(7, 4)$ and $(6, 6)$ nanotubes are not shown in this figure because their $E_{11}^{\text{L}} > 3.0\,\text{eV}$ and the $(6, 6)$ tube gives a negligibly small Q_{m}.

explained within the effective-mass theory. On the other hand, at E_{11}^{H}, the nanotubes should start their coherent vibrations by decreasing their diameters. In the case of armchair nanotubes, for which $E_{11}^{\text{L}} = E_{11}^{\text{H}}$, we expect that no vibration should occur because the two contributions from E_{11}^{L} and E_{11}^{H} should cancel each other.

For semiconducting nanotubes, we see that most of the type-I (type-II) nanotubes start vibrating at E_{11} by decreasing (increasing) their diameters and at higher energies by increasing (decreasing) their diameters. In a few cases, e.g., $(7, 6)$, $(9, 5)$, and $(10, 5)$ nanotubes, the deviation from this rule might come from the 3θ term in Eq. (4.9), especially for the near-armchair nanotubes where θ approaches $\pi/6$. We consider that in the case of armchair nanotubes, such like the $(6, 6)$ nanotube, which is metallic, the coherent phonon amplitude becomes small because of the trigonal warping effect [26].

4.2 Coherent RBLM phonons in GNRs

In this section, we extend the microscopic theory for generating and detecting coherent phonons in SWNTs to the case of coherent phonons in GNRs, although there are
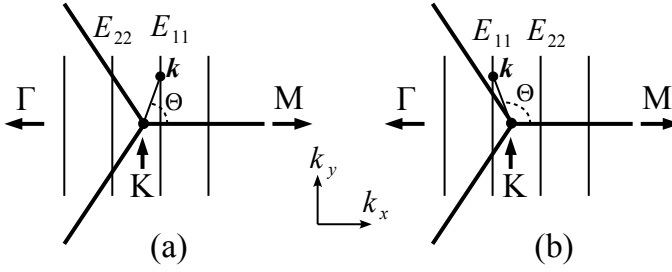
Figure 4.7 Cutting lines for (a) mod 0 aGNR and (b) mod 1 aGNRs near the Dirac K point. To make clear the definition of $\Theta(k)$, in this figure $\Theta(k)$ is shown for an arbitrary **k** at E_{11}. In fact, in the case of mod 0 and mod 1 aGNRs the E_{11} transitions occur at $\Theta(k) = 0$ and $\Theta(k) = \pi$, respectively. The difference between the mod 0 and mod 1 aGNRs can be understood from the position of the E_{11} or E_{22} cutting lines relative to the K point.

no measurements of coherent phonons to date in GNRs. Therefore, our discussion here gives some predictions of CP behavior in GNRs. As discussed in Chapter 2, we basically can consider armchair and zigzag ribbons denoted N_{ab} aGNR and N_{ab} zGNR, respectively, where N_{ab} is the number of AB carbon dimers in the unit cell. However, the presence of localized edge state in the zGNR is quite complicated to be taken into account. Therefore we restrict our discussion here only for coherent phonon amplitudes in aGNRs.

In GNRs there are N_{ab} coherent phonon active modes that vibrate in the plane of the nanoribbon. In all cases, the coherent phonon active mode with the lowest frequency is RBLM mode in which the nanoribbon width periodically expands and contracts. For coherent RBLM phonons the ribbon width $W(t)$ is directly proportional to the coherent phonon amplitude $Q(t)$ [13]. The RBLM phonon energies are sensitive to the ribbon width W and scale roughly as the inverse of the ribbon width in accordance with a simple zone folding expression $E = 0.4/W$ eV with W in units of .

Armchair nanoribbons belong to one of three families depending on the mod number $\mathrm{mod}(N_{ab}, 3)$. Based on a simple band structure calculation, we classify mod 0 and mod 1 aGNRs as semiconductors and mod 2 aGNRs as metals [37, 44]. Since coherent phonon spectroscopy gives direct phase information on the coherent phonon amplitude, it is useful to examine the driving function kernel $S(\mathbf{k})$ as a function of excitation energy and nanoribbon species. For this purpose, let us write the RBLM electron-phonon interaction for an aGNR as

$$H_{\mathrm{ep}} = u_{\mathrm{arm}} \begin{pmatrix} g_{\mathrm{on}} & -\dfrac{g_{\mathrm{off}}}{2} \\ -\dfrac{g_{\mathrm{off}}}{2} & g_{\mathrm{on}} \end{pmatrix}, \tag{4.10}$$

Fig. 4.7: fig/fch4-gnrcl.eps

Table 4.1: Initial lattice behavior due to coherent phonon oscillations at E_{11} and E_{22} in aGNRs.

family	E_{11}	E_{22}
mod 0	expand	contract
mod 1	contract	expand
mod 2	expand or contract	expand or contract

where g_{on} (g_{off}) is the on-site (off-site) coupling constant in eV, while u_{arm} is a ribbon width- or N_{ab}-dependent phonon amplitude. To obtain the electron-phonon matrix element $\mathcal{M}^{\mathrm{ep}}$, we use the same wavefunctions as in (4.7). The wavefunctions are suitable near the graphene Dirac K point and thus they can explain well the aGNR lattice response especially at relatively low energy E_{11} and E_{22} optical transitions. We then obtain a formula for aGNR $\mathcal{M}^{\mathrm{ep}}$ similar to that for the nanotube case,

$$\mathcal{M}^{\mathrm{ep}} = -u_{\mathrm{arm}} \left(2g_{\mathrm{off}} \cos \Theta(k)\right). \tag{4.11}$$

Here $\Theta(k)$ is now defined by the angle that $\mathbf{k}$ points in the two dimensional Brillouin zone measured from the line in $\mathbf{k}$ space perpendicular to the discrete one dimensional Brillouin zone (cutting lines) which goes over the K point (hexagonal corner, see Fig. 4.7). Therefore, the driving function kernel can be written as [13]

$$S(\mathbf{k}) = \frac{2\omega_{\mathrm{RBLM}}}{\hbar} \, u_{\mathrm{arm}} \left[2g_{\mathrm{off}} \cos(\Theta(k))\right], \tag{4.12}$$

where ω_{RBLM} is the RBLM frequency at $q = 0$. From this equation, we can analyze the N_{ab} and E_{ii} dependence of the aGNR initial lattice response. First of all, we should note that g_{off} and u_{arm} are always positive, while $\cos \Theta(k)$ can either be positive or nepgative depending on the value of $\mathbf{k}$ at which the E_{ii} transition occurs.

Using this argument, we can classify the aGNR lattice response based on the aGNR types. For example, let us consider semiconducting mod 0 aGNR and mod 1 aGNRs. The cutting line position for their E_{11} and E_{22} optical transitions are just opposite to each other. For a mod 0 aGNR, we see that $\cos \Theta(k)$ becomes positive (negative) at E_{11} (E_{22}), and thus the aGNR starts the coherent phonon oscillations by expanding (shrinking) its width. This can be seen in the illustration of $\Theta(k)$ in Fig. 4.7. The opposite behavior is true for mod 1 aGNRs.

We should note that the prediction of expansion or contraction of the ribbon width is quite ambiguous for mod 2 metallic aGNRs since in metallic aGNRs two cutting lines are equidistant from the K point and are the lower and higher branches of an E_{ii} transition. Both branches contribute to E_{ii} and we sum up the matrix elements from each contribution to obtain $\mathcal{M}^{\mathrm{ep}}$. For example, if the 1D k-points for the lower and higher branches of E_{ii} are the same, the matrix elements cancel because $\cos \Theta(k) + \cos(\pi - \Theta(k)) = 0$. In this case, the coherent phonon amplitude will be small for the

mod 2 metallic aGNRs as compared to the mod 0 or mod 1 semiconducting aGNRs. In reality, we have slightly different k-points for the two E_{ii} branches due to trigonal warping effects [26]. When trigonal warping effects are included, the resulting nonzero value of $\mathcal{M}^{\mathrm{ep}}$ allows us to determine if the ribbon width initially expands or contracts. We finally summarize the lattice behavior at E_{11} and E_{22} transitions for all families of aGNRs in Table 4.1.

Chapter 5

Excitonic effects on coherent phonon dynamics

In this chapter, we discuss how excitons can affect the generation of coherent radial breathing modes (RBMs) in the ultrafast spectroscopy single wall carbon nanotubes (SWNTs). Photoexcited excitons can localize spatially and give rise to an almost periodic driving force in real space which involves many phonon wavevectors of the exciton-phonon interaction. The equation of motion for the coherent phonons is modeled phenomenologically by the Klein-Gordon equation, which we solve for the oscillation amplitudes as a function of space and time. By averaging the calculated amplitudes per nanotube length, we obtain time-dependent coherent phonon amplitudes that resemble homogeneous oscillations observed in some pump-probe experiments. We interpret this result to mean that the experiments are only able to see a spatial average of coherent phonon oscillations over the wavelength of light in carbon nanotubes and the microscopic details are averaged out. This interpretation is also clarified by calculating the time-dependent absorption spectra resulting from the macroscopic atomic displacements induced by the coherent phonon oscillations. The calculated coherent phonon spectra including excitonic effects show the experimentally observed symmetric peaks at the nanotube transition energies in contrast to the asymmetric peaks obtained when excitonic effects were not included.

5.1   Introduction

Excitons should have at least four important effects on the generation and detection of coherent phonons in SWNTs: (1) the optical transitions will shift to lower energy owing to the Coloumb interaction between the photoexcited electron-hole pair, [29] (2) the strength of the optical transitions will be enhanced since the excitonic wavefunctions have larger optical matrix elements resulting from the localized exciton wavefunc-

tions, [35] (3) the phonon interaction matrix elements may also change because the electron-phonon and hole-phonon matrix elements now become exciton-phonon matrix elements, [35] and (4) in SWNTs, the excitons can become localized along the tube with a typical size of about 1 nm. [76] This will change which phonon modes can couple to the photogenerated excitons. Excitons are known to have localized wavefunctions in both real and reciprocal space, [34] and this should modify the electron-phonon picture of the coherent phonon generation. Due to the localized exciton wavefunctions, the driving force of a coherent phonon is expected to be a Gaussian-like driving force in real space for each localized exciton, whose width is about 1 nm, instead of a constant force considered in the previous works. [11, 12] The localized force can be obtained only if we consider the coupling of excitons and phonons.

The interaction between excitons and coherent phonons will involve many phonon wavevectors for making localized vibrations and many electron (and hole) wavevectors for describing these excitons. By applying strong pump light to the SWNTs, many excitons are generated and the average distances between two nearest excitons are estimated to be about 20 nm. [77, 78] This indicates that the driving force for coherent phonon generation can be approximated by many Gaussian forcing functions, each of which originates from an exciton and are separated by the distance between two excitons. Using such a driving force model also implies that the coherent phonon amplitudes are inhomogeneous along the nanotube axis. However, since the wavelength of light (~ 500 nm) is much larger than the spatial modification of the RBM amplitudes, the laser light can only probe the average of the coherent vibrations.

To simulate the exciton effects using coherent phonon spectroscopy, we model the coherent RBM phonon amplitude $Q(z, t)$ as a function of space and time using the Klein-Gordon equation that will be shown to explain the dispersive wave properties. The driving forces are localized almost periodically, therefore the calculated coherent phonon amplitudes of the RBM are no longer constant along the tube axis. However, by taking an average over the tube length for the calculated coherent phonon amplitudes, we find that the average amplitude fits the oscillations as a function of time observed in the experiments. In order to compare our theory directly with experiments, in which the change of transmittance ($\Delta T/T$) or reflectivity ($\Delta R/R$) is measured, we calculate the time-dependent absorption spectra for macroscopic atomic displacements induced by the coherent phonon oscillations $Q(z, t)$. The symmetric line shape found in the calculated spectra is also consistent with the experimental observations.

5.2   Coherent phonon model with exciton effects

In the conventional model for the coherent phonon generation mechanism in semiconductor systems, phonon modes that are typically excited are the ones with phonon

wavevector $q = 0$. The coherent phonon amplitudes $Q_c(t)$ satisfy a driven oscillator equation, [10, 79]

$$\frac{\partial^2 Q_c(t)}{\partial t^2} + \omega_0^2 Q_c(t) = S_c(t), \tag{5.1}$$

where ω_0 is the phonon frequency at $q = 0$ and $S_c(t)$ is a driving force that depends on the physical properties of a specific material. In the case of a SWNT, without considering the excitonic effects, $S_c(t)$ was given by [11, 12]

$$S_c(t) = -\frac{2\,\omega_0}{\hbar} \sum_{\mu k} \mathcal{M}_\mu^{\mathrm{ep}}(k)\delta f_\mu(k, t), \tag{5.2}$$

where $\mathcal{M}_\mu^{\mathrm{ep}}(k)$ is the electron-phonon matrix element for the μ-th cutting line (one-dimensional Brillouin zone of a SWNT) as a function of the one-dimensional electron wavevector k and is calculated for each phonon mode at $q = 0$. The distribution function δf^μ of photo-excited carriers generated by a laser pulse pumping at the E_{ii} transition energy is obtained by solving a Boltzmann equation for the photogeneration process. [11]

We can see in Eqs. (5.1) and (5.2) that $Q_c(t)$ and $S_c(t)$ have a time dependence only and no spatial dependence when we consider electron-photon (or hole-photon) and electron-phonon (or hole-phonon) interactions, i.e. we ignored the excitonic interaction between the photoexcited electrons and holes. We now extend this model by considering that the exciton effects (exciton-photon and exciton-phonon interactions) give a spatial dependence to the coherent phonon amplitude and to the driving force, which we denote as $Q(z, t)$ and $S(z, t)$, respectively. Here z is the position along the nanotube axis. To describe the coherent phonon amplitude $Q(z, t)$, we propose using of the Klein-Gordon equation,

$$\frac{\partial^2 Q(z, t)}{\partial t^2} - c^2\frac{\partial^2 Q(z, t)}{\partial z^2} = S(z, t) - \kappa Q(z, t) \tag{5.3}$$

where c and κ are the propagation speed and dispersion parameter depending on the SWNT structure, respectively. The Klein-Gordon equation is solved subject to the two initial conditions $Q(z, 0) = 0$ and $\dot{Q}(z, 0) = 0$. The exciton-induced driving force $S(z, t)$ is now given by

$$S(z, t) = -\frac{2}{\hbar} \sum_{\mu, k, q} \omega_q \mathcal{M}_{\mathrm{ex\text{-}ph}}^\mu(k, q)\delta f_\mu(k, t)\mathrm{e}^{iqz}, \tag{5.4}$$

where $\mathcal{M}_{\mathrm{ex\text{-}ph}}^\mu(k, q)$ is the exciton-phonon matrix element on the μ-th cutting line as a function of the exciton wavevector k and phonon wavevector q. By using the driving force expression of Eq. (5.4), the amplitude $Q(z, t)$ is dimensionless because the dimension of $S(z, t)$ is the inverse of time square (instead of length per inverse of time square). Here the actual coherent phonon amplitudes with units of length can be obtained by multiplying $Q(z, t)$ with the zero-point phonon amplitude $Q_0 = \sqrt{\hbar/2M_c\omega_0}$, where M_c is the total mass of carbon atoms in the nanotube unit cell.
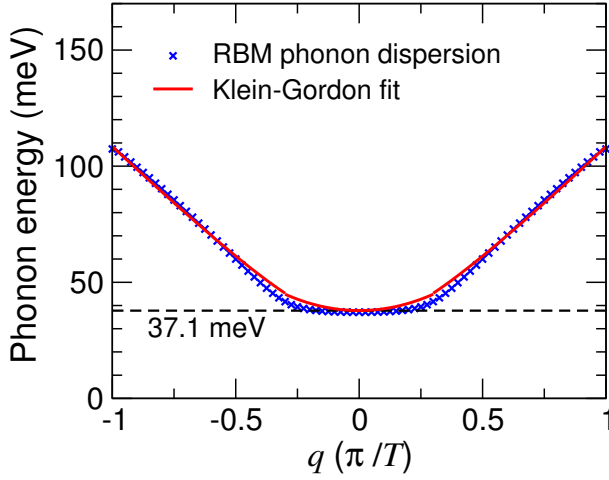
Figure 5.1 RBM phonon dispersion of a $(11,0)$ nanotube. Theoretical data are represented by cross symbols, which are calculated using a force constant model as in Refs. [11] and [47]. The solid line shows the fitted RBM dispersion using the Klein-Gordon dispersion relation in Eq. (5.8). The phonon energy, $\hbar\omega$ is plotted as a function of q in the units of π/T. Here $T = 0.431$ nm is the unit cell length of the $(11,0)$ tube.

The reason why we adopt the Klein-Gordon equation to explain the exciton-induced coherent phonon generation in SWNTs is based on a phenomenological consideration. We generally expect that the coherent RBM phonons are propagating dispersively along the nanotube axis. Integrating $Q(z,t)$ and $S(z,t)$ over z should give $Q_c(t)$ and $S_c(t)$ in Eq. (5.1) which describes the homogeneous vibration observed in experiments. Parameters c and κ in the Klein-Gordon equation can then be obtained from the RBM phonon dispersion, which gives positive c and κ values. To obtain this relationship, we consider the Klein-Gordon equation (5.3) with $S(z,t) = 0$ and take a Fourier transform defined by

$$\tilde{Q}(q,\omega) = \int_{-\infty}^{\infty} \int_{-\infty}^{\infty} Q(z,t)e^{i(qz-\omega t)}\mathrm{d}z\mathrm{d}t, \tag{5.5}$$

to obtain

$$-\omega^2\tilde{Q} + c^2q^2\tilde{Q} = -\kappa\tilde{Q}. \tag{5.6}$$

From Eq. (5.6) we have a dispersion relation for the Klein-Gordon equation,

$$-\omega^2 + c^2q^2 = -\kappa. \tag{5.7}$$

The physical solution of Eq (5.7) for $\omega > 0$ is

$$\omega(q) = \sqrt{c^2q^2 + \kappa}. \tag{5.8}$$
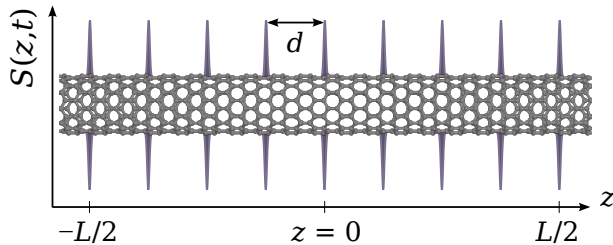
Figure 5.2 Schematic illustration of the Gaussian impulsive force $S(z, t)$ created by excitons which align along the nanotube axis with an average separation of d. The force $S(z, t)$ is symmetric in the circumferential direction.

We can then fit the wave dispersion to the RBM phonon dispersion which is already available by force constant or first-principle models. [47, 80, 53] We are particularly interested in the region of $q \ll \pi/T$ (T is the unit cell length of a SWNT [81]) because this is the typical size over which an exciton in reciprocal space interacts with a phonon. [34, 35] Fitting the RBM phonon dispersion to Eq. (5.8) thus gives the values of both c and κ to be used in the Klein-Gordon equation. As for the phonon dispersion shown in Fig. 5.1, which is calculated for a $(11, 0)$ tube, we obtain $c = 2.545 \, \mathrm{nm/\,ps}$ and $\kappa = 3147.22 \, \mathrm{ps}^{-2}$. Hereafter, unless otherwise mentioned, we will consider the $(11, 0)$ tube as a representative example for the simulation.

We can further simplify Eq. (5.4) by considering that a periodic Gaussian force appears approximately every $15-30 \, \mathrm{nm}$ along the tube axis according to the calculation of the photoexcited carrier density. For example, by solving for the photo-excited distribution δf using the method described in Ref. [11], we estimate an exciton density for a $(11, 0)$ tube at an excitonic transition energy $E_{22} = 1.78 \, \mathrm{eV}$ which is about $5.6 \times 10^{-2} \, \mathrm{nm}^{-1}$. This exciton density corresponds to the average separation between two excitons of about $18 \, \mathrm{nm}$. A Gaussian force centered at the exciton position z_i is then approximated by

$$S_i(z, t) = A_g e^{-(z-z_i)^2/2\sigma_z^2} \theta(t), \tag{5.9}$$

where $\theta(t)$ is the Heaviside step function, A_g is the force magnitude obtained from the product of the exciton-phonon interaction and related factors in Eq. (5.4) [excitonic matrix elements are discussed in Appendix C], and σ_z is the width of the exciton-phonon matrix element for a given (n, m) SWNT.

A typical value of σ_z is related to the exciton size in real space ($\sim 1 \, \mathrm{nm}$). The exciton wavefunctions, exciton energies, exciton-photon and exciton-phonon matrix elements are all calculated by solving the Bethe-Salpeter equation within the extended tight-binding method as developed by Jiang *et al.* [34, 35] The force magnitude thus obtained is on the order of $10^3 \, \mathrm{ps}^{-2}$. For the lowest E_{22} exciton state of the $(11, 0)$ tube, we obtain $\sigma_z = 0.9 \, \mathrm{nm}$ and $A_g = 4.82 \times 10^3 \, \mathrm{ps}^{-2}$. The total driving force used

Fig. 5.2: fig/fch5-excitonforce.eps
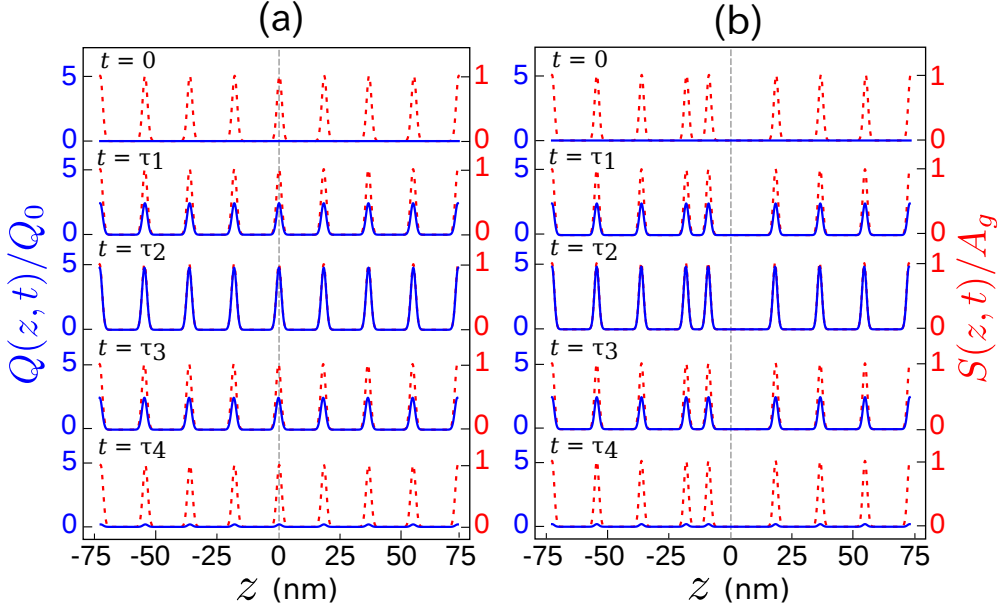
Figure 5.3 Time evolution of coherent phonon amplitudes in a $(11,0)$ nanotube for (a) perfectly uniform spacing between excitons with an average separation $d = 18\,\text{nm}$ and for (b) a slightly random distribution where the center force is shifted by $9\,\text{nm}$. Solid lines show snapshots of $Q(z,t)$ as a function of z (position along the tube axis) for several different t values with a time sequence $\tau_j = j\tau/4$, where $\tau = 0.112\,\text{ps}$ is the fundamental period. $Q(z,t)$ is plotted in terms of the zero-point phonon amplitude for the $(11,0)$ tube, $Q_0 = 2.59 \times 10^{-3}\,\text{nm}$. Dotted lines show the force $S(z,t)$ for comparison.

in solving Eq. (5.3) is a summation of Gaussian forces in terms of Eq. (5.9),

$$S(z,t) = \sum_{i=1}^{N} S_i(z,t), \tag{5.10}$$

where N is the number of excitons (and thus the number of Gaussian forces) in a SWNT. In Fig. 5.2, we show a schematic diagram of a typical model for our simulation. The driving force $S(z,t)$ has an axial symmetry and is aligned along the nanotube axis with a separation of d. To avoid any motions of the center of mass, the general force $S(\boldsymbol{r},t)$ should also satisfy a sum rule,

$$\int_{-\infty}^{\infty} S(\boldsymbol{r},t)\mathrm{d}\boldsymbol{r} = 0, \tag{5.11}$$

which is automatically satisfied for $S(z,t)$ in Eq. (5.10) because of the axial symmetry of the model, as can also be understood from Fig. 5.2. In the present calculation, we fix $d = 18\,\text{nm}$, and there are $N = 9$ narrow Gaussian forces arranged periodically

Fig. 5.3: fig/fch5-Qzt.eps
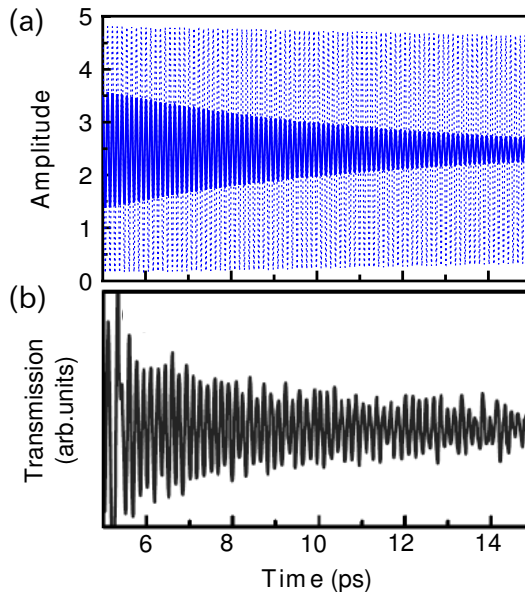
Figure 5.4 (a) Average of coherent phonon amplitudes per length, $A(t)$, plotted as a function of time for a $(11, 0)$ nanotube ($\tau = 0.112$ ps) and shown in units of $Q_0 = 2.59 \times 10^{-3}$ nm. The dotted line represents the average amplitude for the force distribution shown in either Fig. 5.3(a) or 5.3(b). The solid line represents the average amplitude if a decay constant $0.2\,\text{ps}^{-1}$ is taken into account. (b) An example of the transmission oscillation data available for a $(13, 3)$ tube measured in a pump-probe experiment with $\tau = 0.162$ ps (reproduced from Ref. [8]). The average coherent phonon amplitude shown in (a) resembles the oscillating feature of the experimental transmission shown in (b).

(thus $L = 144$ nm). The RBM phonon energy near $q = 0$ is 37.1 meV, corresponding to a frequency $\omega = 297\,\text{cm}^{-1}$ and a vibration period $\tau = 0.112$ ps.

5.3   Time evolution of coherent phonons

In Fig. 5.3, we plot the coherent RBM phonon amplitudes $Q(z, t)$ for a $(11, 0)$ nanotube pumped at its E_{22} transition energy, in which a snapshot is taken for $t = 0$ to τ_4, where $\tau_j = j\tau/4$. Two different cases are shown in Figs. 5.3(a) and (b), in which the separation between excitons might be perfectly uniform or slightly random, respectively. The calculation is done numerically by solving for $Q(z, t)$ from Eq. (5.3) with periodic boundary conditions at $\pm L/2$. We can observe some periodic peaks corresponding to each localized force and these peaks also do not move as a function of time. One might then ask whether or not such exciton effects correctly describe the coherent phonon oscillations in SWNTs. This can be answered by considering the average of the inhomogeneous $Q(z, t)$ per nanotube length.

Fig. 5.4: fig/fch5-Aintegrated.eps

To clarify that our model can describe homogeneous coherent RBM phonon oscillations observed in experiments, [7, 8] we define an average of $Q(z,t)$ as follows

$$A(t) = \frac{1}{L} \int_L Q(z,t) \mathrm{d}z. \tag{5.12}$$

In Fig. 5.4(a), we plot $A(t)$ for the $(11,0)$ tube considered above. We also include a decay constant of $0.2\,\mathrm{ps}^{-1}$ to resemble the experimental results. Interestingly, now the coherent phonon amplitudes, which have been averaged before, could fit the experimental shape of the homogeneous transmission oscillation in Figs. 5.4(b). We then interpret that such an experiment cannot observe the nanoscopic vibration of the exciton effects on the coherent phonon amplitudes, but it can only observe the averaged amplitudes. Moreover, the definition (5.12) is important mathematically to describe the homogeneous coherent phonon amplitudes in experiments if we are able to recover Eq. (5.1) from the Klein-Gordon equation (5.3). Indeed, by integrating both left and right sides of Eq. (5.3),

$$\int_L Q_{tt} \mathrm{d}z - \int_L c^2 Q_{zz} \mathrm{d}z = - \int_L \kappa Q \mathrm{d}z + \int_L S \mathrm{d}z,$$

and using $\int_L Q_{tt} \mathrm{d}z = A_{tt}$, $\int_L \kappa Q \mathrm{d}z = \kappa A$, $\int_L Q_{zz} \mathrm{d}z = 0$, we can obtain

$$A_{tt} + \kappa A(t) = S(z), \tag{5.13}$$

which is nothing but the driven oscillator model in Eq. (5.1).

5.4   Propagation of coherent phonons

It is important to note that we have assumed certain distributions of excitons as a function of z. As shown in Figs. 5.3(a) and (b), we only present the two simplest cases of the exciton distributions that we can imagine. However, excitons in nature might not be uniformly spaced and any exciton distributions with random spacing can be possible. Nevertheless, we expect that our result for the average amplitude $A(t)$ in Fig. 5.4 is approximately constant regardless of the exciton spacing, as far as the average exciton density remains the same. This can be rationalized by considering a trial solution of the Klein-Gordon equation,

$$Q(z,t) = \mathrm{e}^{-\lambda z} \mathrm{e}^{i(qz-\omega t)}, \tag{5.14}$$

which comprises a travelling wave and a decay term with parameter λ to be determined.

By substituting Eq. (5.14) into Eq. (5.3) and setting $S(z,t) = 0$, we obtain

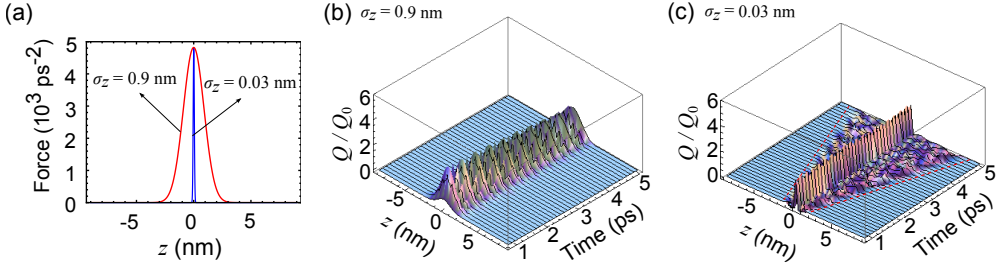$$\lambda = iq \pm \sqrt{\frac{\kappa}{c^2} - q^2}, \tag{5.15}$$

Figure 5.5 (a) Driving forces with two different parameters $\sigma_z(= 0.9\,\text{nm}) > \sigma_{zc}$ and $\sigma_z(= 0.03\,\text{nm}) < \sigma_{zc}$, which give (b) only localized and (c) localized and propagating wave components, respectively. For the $(11,0)$ tube in this simulation, we have $\sigma_{zc} = 0.045\,\text{nm}$. The propagating wave components in (c) travel with a speed of $1.68\,\text{nm/ps}$, as indicated by the slope of the dashed line.

where we have assumed $\omega = qc$ and the sign $\pm$ is determined for the $\pm z$ region. Depending on whether the value of $\sqrt{\kappa/c^2 - q^2}$ is real or pure imaginary, respectively, we can get a spatially localized or propagating solution of $Q(z,t)$. In the presence of a force, we can solve Eq. (5.3) using the Green's function method for a single Gaussian force $S(z,t) = A_g e^{-z^2/2\sigma_z^2}\theta(t)$. The solution for $Q(z,t)$ in the region $-L/2 < z < L/2$ with a boundary condition, $Q(-L/2,t) = Q(L/2,t)$, is given by

$$Q(z,t) = \frac{2\sigma_z A_g \sqrt{2\pi}}{L} \sum_{n=0}^{\infty} \left[\frac{e^{-q_n^2 \sigma_z^2/2}}{c^2 q_n^2 + \kappa} \left(\cos(q_n z) \times (1 - \cos(t\sqrt{c^2 q_n^2 + \kappa})) \right) \right], \quad (5.16)$$

where $q_n = n\pi/L$. This solution consists of a wavepacket of standing waves weighted by a Gaussian distribution and a denominator which comes from the phonon dispersion relation of Eq. (5.8). The Gaussian distribution originates from the Fourier transform of the Gaussian force in real space. In this case, the selection of q is determined by the Fourier transform of the driving force $S(z,t)$. For a Gaussian force in our model, the q value can be selected for the region $0 < q < 1/\sigma_z$. If the maximum $q = 1/\sigma_z$ is smaller than $q_c = \sqrt{\kappa}/c$, then $Q(z,t)$ is localized. If $1/\sigma_z$ is larger than q_c, then $Q(z,t)$ is divided into two contributions: $0 < q < q_c$ and $q_c \leq q < 1/\sigma_z$, in which the former q value gives the localized wave and the latter part gives the propagating wave. We can then define a critical parameter $\sigma_{zc} = 1/q_c$ to explain the localization or propagation of the coherent phonons obtained from the Klein-Gordon equation. It can be further seen that the q_c value is nothing but the critical point the flat dispersion to the linear dispersion in the RBM phonon dispersion relation as shown in Fig. 5.1.

For the $(11,0)$ tube, we have a critical parameter $\sigma_{zc} = (2.545/\sqrt{3147.22})\,\text{nm} = 0.045\,\text{nm}$. Since in our simulation we already used $\sigma_z = 0.9\,\text{nm}$ which is much larger than σ_{zc}, it is then expected that the coherent phonon is sufficiently localized. To

emphasize this fact, we show two different cases of Klein-Gordon waves in Fig. 5.5 for $\sigma_z = 0.9\,\text{nm}$ and $\sigma_z = 0.03\,\text{nm}$. Figure 5.5(a) shows the two forces with different σ_z values, while Figs. 5.5(b) and (c) shows the corresponding coherent phonon amplitudes that are generated. It can be seen that we obtain localized (propagating) waves by using $\sigma_z > \sigma_{zc}$ ($\sigma_z < \sigma_{zc}$). Intuitively, we can understand from Fig. 5.5(c) that a faster appearance of an amplitude propagating along the z direction can be obtained when σ_z becomes much smaller than σ_{zc} although some parts of $Q(z,t)$ remain localized (contribution from $0 < q < q_c$). The propagating wave components in Fig. 5.5(c) travel with a velocity $\sqrt{\kappa}/q$, where q in this case is related to σ_z directly by $q = 1/\sigma_z$, thus giving a speed of $\sqrt{3147.22\,\text{ps}^{-2}} \times 0.03\,\text{nm} = 1.68\,\text{nm}/\text{ps}$.

In contrast, in the case of σ_z much larger than σ_{zc} [e.g. Fig. 5.5(b)], we cannot see any amplitudes along the z direction except in a limited region where the force exists, i.e. the propagating wave components cannot be observed. Indeed, the actual RBM dispersion is a bit flatter than the approximation from the Klein-Gordon wave dispersion (see Fig. 5.1). This means that the modes are localized even more. Therefore, in our case of $\sigma_z = 0.9\,\text{nm}$, each excitonic force will not interfere with neighboring force sites separated by distance d, which indicates that the average amplitude $A(t)$ in Fig. 5.4 is not affected by a random separation between every excitonic force. In general, we may say that the localized vibration is a characteristic of the optical phonon propagation driven by a localized force because the wavepacket is dominated by $q \approx 0$ phonons but the contribution of the group velocity comes from $q \geq q_c$. This optical phonon feature differs from that of acoustic phonon whose solution is expressed in terms of traveling waves. [82]

5.5   Coherent phonon spectra

We then calculate the optical absorption spectra as a function of time using the calculated $Q(z,t)$. It is expected that the inhomogeneous coherent phonon oscillations induce a macroscopic atomic displacement which modifies the transfer integral and thus modulates the energy gap. We calculate the absorption coefficient $\alpha(E_L, t)$, where E_L is the laser excitation energy, by evaluating it in the dipole approximation using Fermi's golden rule. The absorption coefficient at a photon energy E_L obtained by including exciton effects is given by [66, 83]

$$\alpha(E_L, t) = \frac{8e^2}{E_L R m_0 c_0} \sum_{\mu k} |\mathcal{M}^{\mu}_{\text{ex-op}}|^2 \delta f^{\mu}(k, t)\, \delta\left(E_{ii}(t) - E_L\right), \qquad (5.17)$$

where $\mathcal{M}^{\mu}_{\text{ex-op}}$ is the exciton-photon matrix element within the dipole approximation corresponding to the transition between the initial and final state on the μ-th cutting line, R is the tube radius, m_0 is the electron mass, and c_0 is the speed of light. The exciton energy E_{ii} is now time-dependent because of the change in transfer integral due to coherent RBM phonon vibrations $A(t)$.
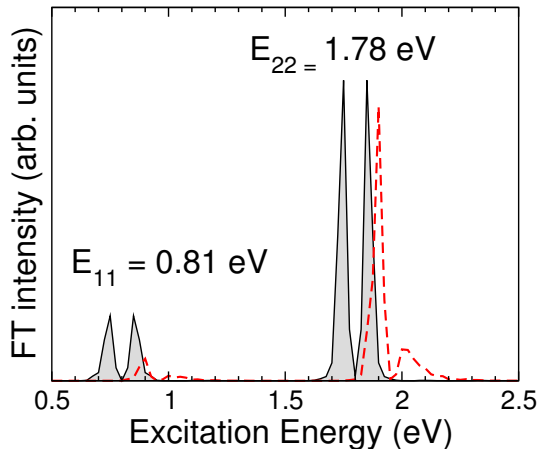
Figure 5.6 Fourier transform intensity of the time-dependent absorption coefficient for the coherent RBM phonon of a (11,0) nanotube as a function of excitation energies. The solid line represents the coherent phonon spectra which include excitonic effects, showing a symmetric double-peaked line shape at each transition energy E_{ii}. The dashed line represents the coherent phonon spectra without excitonic effects, in which asymmetric line shapes were obtained previously [11].

Since the bandgap is inversely proportional to the diameter oscillation (or to the coherent RBM amplitudes), the time-dependent absorption $\alpha(E_{\mathrm{L}}, t)$ has the same oscillating feature as the average amplitude $A(t)$. However, exciton effects acting on the absorption spectrum will modify the shape of the absorption spectra compared to that obtained without inclusion of the exciton effects. We should then calculate the time-dependent absorption for a broad range of excitation energies, for example, within the range of 0.5 to 2.5 eV. By performing a Fourier transformation numerically over this energy range, we can obtain the RBM coherent phonon spectra as shown in Fig. 5.6, which include E_{11} and E_{22} for the (11,0) tube that we consider. The coherent phonon spectra calculated by including the excitonic effects given in Fig. 5.6 show double-peaked structures as a function of the excitation energies, either with or without including the excitonic effects, as indicated by the solid and dashed lines in Fig. 5.6, respectively.

The reason for the presence of the double-peak features (either symmetric or asymmetric) in the excitation-dependent coherent phonon intensity can be explained as follows. The generation of coherent RBM phonons modifies the electronic structure of SWNTs and thus it can be detected as temporal oscillations in the transmittance of the probe beam. Since the RBM is an isotropic vibration of the nanotube lattice in the radial direction, i.e. the diameter periodically oscillates at the RBM frequency, this makes the band gap E_g also oscillate at the same frequency. As a result, interband

transition energies oscillate in time, leading to ultrafast modulations of the absorption coefficients at the RBM frequency, which is also equivalent to the oscillations in the probe transmittance, and thus correspondingly, the excitation energy dependence of the coherent phonon intensity shows a derivative-like behavior. More explicitly, the effect on the absorption α for small changes in the gap can be modeled by

$$\alpha(E_{\mathrm{L}} - E_g) \approx \alpha(E_{\mathrm{L}} - E_g^0) - \frac{\partial \alpha(E_{\mathrm{L}} - E_g^0)}{\partial E_{\mathrm{L}}} \delta E_g + \dots, \qquad (5.18)$$

which gives

$$\Delta\alpha \approx -\frac{\partial \alpha(E_{\mathrm{L}} - E_g^0)}{\partial E_{\mathrm{L}}} \delta E_g, \qquad (5.19)$$

where E_g is assumed to be time-dependent, and δE_g here corresponds to a small change in the bandgap. Since the coherent phonon intensity is obtained by taking the Fourier transform (power spectrum) of the differential transmission, the coherent phonon intensity is thus proportional to the square of the derivative of the absorption coefficient.

The excitonic absorption coefficient basically has a symmetric lineshape with a single peak. [30] Therefore, the derivative of the excitonic absorption coefficient will give a symmetric double-peak feature, in contrast to the asymmetric lineshape expected from the 1D van Hove singularity (joint density of states). Here the use of the Klein-Gordon equation which gives nonhomogeneous macroscopic atomic displacements is then also justified by obtaining the symmetric line shape for the coherent phonon spectra. On the other hand, in the free carrier model without the excitonic effects, we see an asymmetric double-peaked structure at each transition with the stronger peak at lower energy and the weaker peak at higher energy, which originate from the derivative of the asymmetric lineshape of the absorption coefficient. Moreover it has also been noted in some earlier works that the transition energy was shifted upward by several hundred meV. [5, 30]

As a final remark, we would like to mention that considering the localized excitons in this work might be just one possibility that gives the symmetric peak of the absorption spectrum because the origin of the symmetric absorption lineshape is basically from the presence of discrete energy levels of excitons in carbon nanotubes. In this sense, if there are other configurations of excitons in carbon nanotubes, which are not localized, such cases might also give rise to the symmetric absorption lineshape. This can be an open issue for future studies. However, we expect that as an initial condition of the system after the excitation by the pump pulse, the excitons should be localized with a certain average separation.

Chapter 6

Conclusions

In this thesis, we have discussed theoretical calculation for the coherent phonon properties in single wall carbon nanotubes (SWNTs) and graphene nanoribbons (GNRs). Calculations have been performed particularly for the radial breathing modes (RBMs) of SWNTs and radial breathing like modes (RBLMs) of GNRs. In order to understand the coherent phonon properties, we need a detailed knowledge of the electronic structure, optical matrix elements, phonon modes and electron-phonon matrix elements. In this study, we have developed a microscopic theory for coherent phonon generation which uses an extended tight-binding model and effective mass theory. Our finding can then be divided into two parts as follows.

Excitation and structural dependence of coherent phonon amplitudes in SWNTs and GNRs

We found that the coherent RBM (of SWNTs) and RBLM (of GNRs) phonon amplitudes strongly depend on tube chirality and ribbon type. In addition, we find the phase of the amplitude (i.e. whether the tube diameter or ribbon width initially expand or contract) can vary depending on the tube chirality or ribbon type. Comparison of our ETB results with a simplified effective mass theory provides an explanation of the initial contraction or expansion of the materials.

Using effective mass theory for the electron-phonon interactions, we can analytically analyze how the tube diameter and the ribbon width changes in response to femtosecond laser excitation. We found that the initial phase of the coherent phonon oscillation depends on the relative position of the E_{11} and E_{22} cutting lines with respect to the K point, which originate from the k-dependent electron-phonon interaction. The theoretical prediction will need further confirmation from experimentalists in the near future. We suggest the use of resonant ultrafast pump-probe spectroscopy with pulse-shaping technique to clarify our finding in this work for SWNTs and GNRs.

Excitonic effects on coherent phonon amplitudes in SWNTs

SWNTs have a special feature in which excitons can exist even at room temperature. We have shown that excitonic effects modify the coherent phonon amplitudes in SWNTs as described by the Klein-Gordon equation. The localized exciton wavefunctions result in an almost periodic and localized driving force in space, and thus also give localized coherent phonon amplitudes. Although the exciton effects make the amplitudes inhomogeneous, these amplitudes might be difficult to observe in experiments since the long wavelength of the probe pulse averages over the sample. However, when we define a spatial average of the localized coherent phonon amplitudes, the average amplitudes can be fitted to the experimental results.

Moreover, we are able to simulate the experimental observation of a symmetric double-peak feature of coherent phonon intensity as a function of excitation energy, which is an obvious signature of the excitonic effects in SWNTs. Therefore, we may say that the pump-probe experiments on coherent phonons in SWNTs can only observe the average of the coherent phonon amplitudes induced by the exciton effects. As a side note, we also predict that the coherent RBM phonons in SWNTs do not propagate within the timescale of photoexcited carrier relaxation.

<p align="center">***</p>

Finally, as the experimental ability to make better samples (i.e. graphene nanoribbons and carbon nanotubes of a fixed chirality) improves, we would expect more experiments to confirm our recent theoretical prediction suggested in this thesis. Furthermore, we also expect that one would be able to generate coherent phonons in that are not RBM or RBLM, but instead correspond to $q \neq 0$ acoustic modes. The study of coherent phonons in carbon based nanostructures is only in its infancy and the future promises to be rewarding.

Appendix A

Derivation of coherent phonon equations of motion

Here we give a detailed derivation for coherent phonon equations of motion (3.12) and (3.13). We start with the Hamiltonian defined by

$$H = H_{\mathrm{e}} + H_{\mathrm{ph}} + H_{\mathrm{ep}}, \tag{A.1}$$

where

$$H_{\mathrm{e}} = \sum_{n,\mathbf{k}} \epsilon_{n\mathbf{k}} c_{n\mathbf{k}}^{\dagger} c_{n\mathbf{k}}, \tag{A.2a}$$

$$H_{\mathrm{p}} = \sum_{\mathbf{q}} \hbar\omega_{\mathbf{q}} b_{\mathbf{q}}^{\dagger} b_{\mathbf{q}}, \tag{A.2b}$$

$$H_{\mathrm{ep}} = \sum_{n,\mathbf{k},\mathbf{q}} \mathcal{M}_{\mathbf{k},\mathbf{q}}^{n} \left(b_{\mathbf{q}} + b_{-\mathbf{q}}^{\dagger} \right) c_{n\mathbf{k}+\mathbf{q}}^{\dagger} c_{n\mathbf{k}}, \tag{A.2c}$$

are the electron Hamiltonian, the phonon Hamiltonian, and the electron-phonon interaction Hamiltonian, respectively. Here the indices n, $\mathbf{k}$, and $\mathbf{q}$ respectively denote the electronic energy state, electron wavevector, and phonon wavevector.

To obtain the equations of motion for coherent phonons, we use the Heisenberg equation,

$$\frac{d\mathcal{O}}{dt} = \frac{i}{h}[H, \mathcal{O}]. \tag{A.3}$$

In this case, the operator $\mathcal{O}$ is to be substituted by the phonon annihilation operator $b_{\mathbf{q}}$ and creation operator $b_{\mathbf{q}}^{\dagger}$ because we define the coherent phonon amplitude $Q(t)$ as

$$Q(t) \equiv \langle b_{\mathbf{q}} + b_{-\mathbf{q}}^{\dagger} \rangle. \tag{A.4}$$

Since $[H_{\mathrm{e}}, b_{\mathbf{q}}] = [H_{\mathrm{e}}, b_{\mathbf{q}}^{\dagger}] = 0$, for the generation of coherent phonons we can simply insert the phonon Hamiltonian H_{p} and H_{ep} as the total Hamiltonian $H = H_{\mathrm{p}} + H_{\mathrm{ep}}$ into the Heisenberg equation of motion.

Annihilation operator equation

The dynamical equation for the annihilation operator is

$$\frac{\partial b_{\mathbf{q}}(t)}{\partial t} = \frac{i}{\hbar}[H_{\mathrm{p}} + H_{\mathrm{ep}}, b_{\mathbf{q}}(t)]. \tag{A.5}$$

Let us work with each term one by one:

- H_{p} term

$$[H_{\mathrm{p}}, b_{\mathbf{q}}] = \sum_{\mathbf{q}'} \hbar\omega_{\mathbf{q}'}[b_{\mathbf{q}'}^{\dagger} b_{\mathbf{q}'}, b_{\mathbf{q}}]$$

$$= \hbar\omega_{\mathbf{q}}[b_{\mathbf{q}}^{\dagger}, b_{\mathbf{q}}]b_{\mathbf{q}}$$

$$\therefore [H_{\mathrm{p}}, b_{\mathbf{q}}] = -\hbar\omega_{\mathbf{q}}b_{\mathbf{q}} \tag{A.6}$$

- H_{ep} term

$$[H_{\mathrm{ep}}, b_{\mathbf{q}}] = \sum_{n,\mathbf{k},\mathbf{q}'} \mathcal{M}_{\mathbf{k},\mathbf{q}'}^{n} c_{n\mathbf{k}+\mathbf{q}'}^{\dagger} c_{n\mathbf{k}}[b_{-\mathbf{q}'}^{\dagger}, b_{\mathbf{q}}]$$

$$= \sum_{n,\mathbf{k},\mathbf{q}'} \mathcal{M}_{\mathbf{k},\mathbf{q}'}^{n} c_{n\mathbf{k}+\mathbf{q}'}^{\dagger} c_{n\mathbf{k}}\delta_{\mathbf{q}',-\mathbf{q}}$$

$$\therefore [H_{\mathrm{ep}}, b_{\mathbf{q}}] = -\sum_{n,\mathbf{k},\mathbf{q}} \mathcal{M}_{\mathbf{k},-\mathbf{q}}^{n} c_{n\mathbf{k}-\mathbf{q}}^{\dagger} c_{n\mathbf{k}} \tag{A.7}$$

Inserting Eqs. (A.6) and (A.7) to (A.5), we obtain

$$\frac{\partial b_{\mathbf{q}}(t)}{\partial t} = -i\omega_{\mathbf{q}}b_{\mathbf{q}}(t) - \frac{i}{\hbar}\sum_{n,\mathbf{k}} \mathcal{M}_{\mathbf{k},-\mathbf{q}}^{n} c_{n\mathbf{k}-\mathbf{q}}^{\dagger}(t)c_{n\mathbf{k}}(t) \tag{A.8}$$

Creation operator equation

Similar to the equation of motion for the annihilation operator, we can obtain the equation of motion for the creation operator,

$$\frac{\partial b_{\mathbf{q}}^{\dagger}(t)}{\partial t} = \frac{i}{\hbar}[H_{\mathrm{p}} + H_{\mathrm{ep}}, b_{\mathbf{q}}^{\dagger}(t)]. \tag{A.9}$$

Work out each term one by one:

- H_{p} term

$$[H_{\mathrm{p}}, b_{\mathbf{q}}^{\dagger}] = \sum_{\mathbf{q}'} \hbar\omega_{\mathbf{q}'}[b_{\mathbf{q}'}^{\dagger} b_{\mathbf{q}'}, b_{\mathbf{q}}^{\dagger}]$$

$$= \hbar\omega_{\mathbf{q}}[b_{\mathbf{q}}, b_{\mathbf{q}}^{\dagger}]b_{\mathbf{q}}^{\dagger}$$

$$\therefore [H_{\mathrm{p}}, b_{\mathbf{q}}] = \hbar\omega_{\mathbf{q}}b_{\mathbf{q}}^{\dagger} \tag{A.10}$$

- H_{ep} term

$$[H_{\text{ep}}, b_{\mathbf{q}}^{\dagger}] = \sum_{n,\mathbf{k},\mathbf{q}'} \mathcal{M}_{\mathbf{k},\mathbf{q}'}^n c_{n\mathbf{k}+\mathbf{q}'}^{\dagger} c_{n\mathbf{k}} [b_{\mathbf{q}'}, b_{\mathbf{q}}^{\dagger}]$$

$$= \sum_{n,\mathbf{k},\mathbf{q}'} \mathcal{M}_{\mathbf{k},\mathbf{q}'}^n c_{n\mathbf{k}+\mathbf{q}'}^{\dagger} c_{n\mathbf{k}} \delta_{\mathbf{q}',\mathbf{q}}$$

$$\therefore [H_{\text{ep}}, b_{\mathbf{q}}^{\dagger}] = \sum_{n,\mathbf{k}} \mathcal{M}_{\mathbf{k},\mathbf{q}}^n c_{n\mathbf{k}+\mathbf{q}}^{\dagger} c_{n\mathbf{k}} \tag{A.11}$$

Inserting Eqs. (A.10) and (A.11) to (A.9), we obtain

$$\frac{\partial b_{\mathbf{q}}^{\dagger}(t)}{\partial t} = i\omega_{\mathbf{q}} b_{\mathbf{q}}^{\dagger}(t) + \frac{i}{\hbar} \sum_{n,\mathbf{k}} \mathcal{M}_{\mathbf{k},\mathbf{q}}^n c_{n\mathbf{k}+\mathbf{q}}^{\dagger}(t) c_{n\mathbf{k}}(t). \tag{A.12}$$

Coherent phonon amplitude

Now, the coherent phonon amplitude is defined by

$$Q(t) \equiv \langle b_{\mathbf{q}} + b_{-\mathbf{q}}^{\dagger} \rangle. \tag{A.13}$$

We can take the first derivative of the coherent phonon amplitude,

$$\frac{\partial Q(t)}{\partial t} = \left\langle \frac{\partial b_{\mathbf{q}}}{\partial t} + \frac{\partial b_{-\mathbf{q}}^{\dagger}}{\partial t} \right\rangle, \tag{A.14}$$

and use the results of the annihilation and creation operator equations in (A.8) and (A.12). We obtain

$$\frac{\partial Q(t)}{\partial t} = \left\langle -i\omega_{\mathbf{q}} b_{\mathbf{q}}(t) - \frac{i}{\hbar} \sum_{n,\mathbf{k}} \mathcal{M}_{\mathbf{k},-\mathbf{q}}^n \cancel{c_{n\mathbf{k}-\mathbf{q}}^{\dagger}(t) c_{n\mathbf{k}}(t)} \right.$$

$$\left. + i\omega_{\mathbf{q}} b_{-\mathbf{q}}^{\dagger}(t) + \frac{i}{\hbar} \sum_{n,\mathbf{k}} \mathcal{M}_{\mathbf{k},-\mathbf{q}}^n \cancel{c_{n\mathbf{k}-\mathbf{q}}^{\dagger}(t) c_{n\mathbf{k}}(t)} \right\rangle$$

$$\therefore \frac{\partial Q(t)}{\partial t} = -i\omega_{\mathbf{q}} \langle b_{\mathbf{q}} - b_{-\mathbf{q}}^{\dagger} \rangle \tag{A.15}$$

Taking the second derivative of Eq. (A.15), we now have

$$\frac{\partial^2 Q(t)}{\partial t^2} = -i\omega_{\mathbf{q}} \left\langle \frac{\partial b_{\mathbf{q}}}{\partial t} - \frac{\partial b_{-\mathbf{q}}^{\dagger}}{\partial t} \right\rangle, \tag{A.16}$$

and again we use the results of the annihilation and creation operator dynamical

equations,

$$
\frac{\partial^2 Q(t)}{\partial t^2} = -i\omega_{\mathbf{q}}\Big\langle -i\omega_{\mathbf{q}}b_{\mathbf{q}}(t) - \frac{i}{\hbar}\sum_{n,\mathbf{k}}\mathcal{M}^n_{\mathbf{k},-\mathbf{q}}c^\dagger_{n\mathbf{k}-\mathbf{q}}(t)c_{n\mathbf{k}}(t)
$$

$$
- i\omega_{\mathbf{q}}b^\dagger_{-\mathbf{q}}(t) - \frac{i}{\hbar}\sum_{n,\mathbf{k}}\mathcal{M}^n_{\mathbf{k},-\mathbf{q}}c^\dagger_{n\mathbf{k}-\mathbf{q}}(t)c_{n\mathbf{k}}(t)\Big\rangle
$$

$$
= -i\omega_{\mathbf{q}}\left(-i\omega_{\mathbf{q}}\langle b_{\mathbf{q}}(t) + b^\dagger_{-\mathbf{q}}(t)\rangle - 2\frac{i}{\hbar}\sum_{n,\mathbf{k}}\mathcal{M}^n_{\mathbf{k},-\mathbf{q}}\langle c^\dagger_{n\mathbf{k}-\mathbf{q}}(t)c_{n\mathbf{k}}(t)\rangle\right)
$$

$$
= -\omega_{\mathbf{q}}^2 Q(t) - \frac{2\omega_q}{\hbar}\sum_{n,\mathbf{k}}\mathcal{M}^n_{\mathbf{k},-\mathbf{q}}\langle c^\dagger_{n\mathbf{k}-\mathbf{q}}(t)c_{n\mathbf{k}}(t)\rangle.
$$

By defining $n^n_{\mathbf{k},\mathbf{k}-\mathbf{q}} = \langle c^\dagger_{n\mathbf{k}-\mathbf{q}}(t)c_{n\mathbf{k}}(t)\rangle$, we finally obtain

$$
\frac{\partial^2 Q_{\mathbf{q}}(t)}{\partial t^2} + \omega_{\mathbf{q}}^2 Q_{\mathbf{q}}(t) = -\frac{2\omega_{\mathbf{q}}}{\hbar}\sum_{n,\mathbf{k}}\mathcal{M}^n_{\mathbf{k},-\mathbf{q}}n^n_{\mathbf{k},\mathbf{k}-\mathbf{q}}, \tag{A.17}
$$

which is nothing but Eq. (3.12).

Appendix B

Deformation-induced gauge field in graphene

Here we review how to obtain the off-site Hamiltonian and on-site Hamiltonian given in Eqs. (3.50) and (3.39), respectively, within the effective mass theory, as discussed by Sasaki and Saito [71]. The dynamics of the conducting electrons in graphene materials are different from those of ideal flat graphene, because in the former case, there are shape fluctuations, such as effects of cylindrical shape and phonon vibration, that result in the modification of the overlap matrix elements of nearest-neighbor π-orbitals and of the on-site potential energy. We refer to the modification of the nearest-neighbor hopping integral as the off-site interaction and a shift of the on-site potential energy as the on-site interaction.

Off-site interaction

First we consider the perturbation from the off-site interaction in which only off-diagonal matrix element has a non-zero value. A lattice deformation induces a local modification of the nearest-neighbor hopping integral as $-\gamma_0 \to -\gamma_0 + \delta\gamma_0^a(\boldsymbol{r}_i)$ ($a = 1, 2, 3$). The perturbation $\mathcal{H}_1$ is defined as

$$\mathcal{H}_1 \equiv \sum_{i\in A} \sum_{a=1,2,3} \delta\gamma_0^a(\mathbf{r}_i) \left((c_{i+a}^{\mathrm{B}})^\dagger c_i^{\mathrm{A}} + (c_i^{\mathrm{A}})^\dagger c_{i+a}^{\mathrm{B}}\right). \tag{B.1}$$

We also define the Bloch wavefunction with wavevector $\boldsymbol{k}$,

$$|\Psi_s^{\boldsymbol{k}}\rangle = \frac{1}{\sqrt{N_u}} \sum_{i\in s} e^{i\boldsymbol{k}\cdot\boldsymbol{r}_i} (c_i^s)^\dagger |0\rangle \quad (s = \mathrm{A}, \mathrm{B}), \tag{B.2}$$

where the sum on i is taken over the crystal, N_u is the number of the hexagonal unit cells, and $|0\rangle$ denotes the state of carbon atoms without π-electrons. We use the same geometrical configuration of graphene as shown in Fig. 3.3.

The off-site matrix element of $\mathcal{H}_1$ with respect to the Bloch wave functions in Eq. (B.2) with $\boldsymbol{k}$ and $\boldsymbol{k} + \delta\boldsymbol{k}$ is given by

$$\langle\Psi_{\text{A}}^{\boldsymbol{k}+\delta\boldsymbol{k}}|\mathcal{H}_1|\Psi_{\text{B}}^{\boldsymbol{k}}\rangle = \frac{1}{N_u}\sum_{i\in\text{A}}\sum_{a=1,2,3}\delta\gamma_0^a(\boldsymbol{r}_i)f_a(\boldsymbol{k})e^{-i\delta\boldsymbol{k}\cdot\boldsymbol{r}_i},$$

$$\langle\Psi_{\text{B}}^{\boldsymbol{k}+\delta\boldsymbol{k}}|\mathcal{H}_1|\Psi_{\text{A}}^{\boldsymbol{k}}\rangle = \frac{1}{N_u}\sum_{i\in\text{A}}\sum_{a=1,2,3}\delta\gamma_0^a(\boldsymbol{r}_i)f_a(\boldsymbol{k})^*e^{-i\delta\boldsymbol{k}\cdot(\boldsymbol{r}_i+\boldsymbol{R}_a)}.$$

$$(B.3)$$

Here we consider that when $\delta\boldsymbol{k}$ is small enough compared with the reciprocal lattice vector, a wavevector $\boldsymbol{k}$ near the K (or K') point is scattered to the $\boldsymbol{k}' = \boldsymbol{k} + \delta\boldsymbol{k}$ within the region near the K (or K') point. If $\boldsymbol{k}$ is measured from $\boldsymbol{k}_{\text{F}}$, we obtain

$$\langle\Psi_{\text{A}}^{\boldsymbol{k}_{\text{F}}+\boldsymbol{k}+\delta\boldsymbol{k}}|\mathcal{H}_1|\Psi_{\text{B}}^{\boldsymbol{k}_{\text{F}}+\boldsymbol{k}}\rangle = \frac{1}{N_u}\sum_{i\in\text{A}}\sum_{a=1,2,3}\delta\gamma_a(\boldsymbol{r}_i)f_a(\boldsymbol{k}_{\text{F}})e^{-i\delta\boldsymbol{k}\cdot\boldsymbol{r}_i} + \mathcal{O}(\delta k\delta\gamma_a),$$

$$\langle\Psi_{\text{B}}^{\boldsymbol{k}_{\text{F}}+\boldsymbol{k}+\delta\boldsymbol{k}}|\mathcal{H}_1|\Psi_{\text{A}}^{\boldsymbol{k}_{\text{F}}+\boldsymbol{k}}\rangle = \frac{1}{N_u}\sum_{i\in\text{A}}\sum_{a=1,2,3}\delta\gamma_a(\boldsymbol{r}_i)f_a(\boldsymbol{k}_{\text{F}})^*e^{-i\delta\boldsymbol{k}\cdot\boldsymbol{r}_i} + \mathcal{O}(\delta k\delta\gamma_a),$$

$$(B.4)$$

The correction indicated by $\mathcal{O}(\delta k\delta\gamma_a)$ in Eq. (B.4) is negligible when $|\delta\boldsymbol{k}| \ll |\boldsymbol{k}_{\text{F}}|$. Substituting $f_1(\boldsymbol{k}_{\text{F}}) = 1$, $f_2(\boldsymbol{k}_{\text{F}}) = e^{-i\frac{2\pi}{3}}$ and $f_3(\boldsymbol{k}_{\text{F}}) = e^{+i\frac{2\pi}{3}}$ into Eq. (B.4), we can obtain

$$\langle\Psi_{\text{A}}^{\boldsymbol{k}_{\text{F}}+\boldsymbol{k}+\delta\boldsymbol{k}}|\mathcal{H}_1|\Psi_{\text{B}}^{\boldsymbol{k}_{\text{F}}+\boldsymbol{k}}\rangle = \frac{v_{\text{F}}}{N_u}\sum_{i\in\text{A}}\left\{A_x^{\text{q}}(\boldsymbol{r}_i) - iA_y^{\text{q}}(\boldsymbol{r}_i)\right\}e^{-i\delta\boldsymbol{k}\cdot\boldsymbol{r}_i},$$

$$\langle\Psi_{\text{B}}^{\boldsymbol{k}_{\text{F}}+\boldsymbol{k}+\delta\boldsymbol{k}}|\mathcal{H}_1|\Psi_{\text{A}}^{\boldsymbol{k}_{\text{F}}+\boldsymbol{k}}\rangle = \frac{v_{\text{F}}}{N_u}\sum_{i\in\text{A}}\left\{A_x^{\text{q}}(\boldsymbol{r}_i) + iA_y^{\text{q}}(\boldsymbol{r}_i)\right\}e^{-i\delta\boldsymbol{k}\cdot\boldsymbol{r}_i},$$

$$(B.5)$$

where $\boldsymbol{A}^{\text{q}}(\boldsymbol{r}) = (A_x^{\text{q}}(\boldsymbol{r}), A_y^{\text{q}}(\boldsymbol{r}))$ is defined by $\delta\gamma_0^a(\boldsymbol{r})$ ($a = 1, 2, 3$) as

$$v_{\text{F}}A_x^{\text{q}}(\boldsymbol{r}) = \delta\gamma_0^1(\boldsymbol{r}) - \frac{1}{2}\left(\delta\gamma_0^2(\boldsymbol{r}) + \delta\gamma_0^3(\boldsymbol{r})\right),$$

$$v_{\text{F}}A_y^{\text{q}}(\boldsymbol{r}) = \frac{\sqrt{3}}{2}\left(\delta\gamma_0^2(\boldsymbol{r}) - \delta\gamma_0^3(\boldsymbol{r})\right).$$

$$(B.6)$$

Since the diagonal term vanishes, i.e. $\langle\Psi_s^{\boldsymbol{k}}|\mathcal{H}_1|\Psi_s^{\boldsymbol{k}'}\rangle = 0$ ($s = \text{A,B}$), Eq. (B.5) shows that $\mathcal{H}_1$ is expressed by $v_{\text{F}}\sigma\cdot\boldsymbol{A}^{\text{q}}(\boldsymbol{r})$ in the effective-mass Hamiltonian. Therefore, the total Hamiltonian of a deformed graphene near the K point is expressed by

$$\mathcal{H}_0^{\text{K}} + \mathcal{H}_1^{\text{K}} = v_{\text{F}}\sigma\cdot(\hat{\boldsymbol{p}} + \boldsymbol{A}^{\text{q}}(\boldsymbol{r})).$$

$$(B.7)$$

We can see from Eq. (B.7) that the off-site interaction can be included in the effective-mass equations as a gauge field, $\boldsymbol{A}^{\text{q}}(\boldsymbol{r})$. We call $\boldsymbol{A}^{\text{q}}(\boldsymbol{r})$ as the **deformation-induced gauge field** and distinguish it from the electromagnetic gauge field $\boldsymbol{A}(\boldsymbol{r})$ [71].

On-site interaction

Now we consider the on-site interaction by a defect of the crystal. A lattice deformation gives rise not only to a change in the transfer integral between A and B atoms but

also a change in the potential at the A (B) atom ϕ_A (ϕ_B) which we call the off-site and on-site deformation potential, respectively. We denote the on-site deformation potential by a 2×2 matrix as

$$\mathcal{H}_{\text{on}} = \begin{pmatrix} \phi_A(\boldsymbol{r}_i) & 0 \\ 0 & \phi_B(\boldsymbol{r}_i + \boldsymbol{R}_1) \end{pmatrix}. \tag{B.8}$$

Using the coordinate system introduced in Fig. 3.3, we denote the displacement vector of A-atom at $\boldsymbol{r}_i$ is $\boldsymbol{u}_A(\boldsymbol{r}_i)$ and that of B-atom at $\boldsymbol{r}_j$ is $\boldsymbol{u}_B(\boldsymbol{r}_j)$. The deformation potential of A-atom at $\boldsymbol{r}_i$, $\phi_A(\boldsymbol{r}_i)$, is induced by the relative displacements of three nearest neighbor B-atoms from the A-atom $(\boldsymbol{u}_B(\boldsymbol{r}_i + \boldsymbol{R}_a) - \boldsymbol{u}_A(\boldsymbol{r}_i))$ as

$$\phi_A(\boldsymbol{r}_i) = \frac{g_{\text{on}}}{\ell a_{\text{cc}}} \sum_{a=1,2,3} \boldsymbol{R}_a \cdot (\boldsymbol{u}_B(\boldsymbol{r}_i + \boldsymbol{R}_a) - \boldsymbol{u}_A(\boldsymbol{r}_i)), \tag{B.9}$$

where g_{on} denotes gradient of the atomic potential at $\boldsymbol{r}_i$, and ℓ denotes $3a_{\text{cc}}/2$. Here we assume that $|\boldsymbol{u}_B(\boldsymbol{r}_i + \boldsymbol{R}_a) - \boldsymbol{u}_A(\boldsymbol{r}_i)| \ll a_{\text{cc}}$ and that $\phi_A(\boldsymbol{r}_i)$ depends linearly on the relative displacement vector.

By expanding $\boldsymbol{u}_B(\boldsymbol{r}_i + \boldsymbol{R}_2)$ as $\boldsymbol{u}_B(\boldsymbol{r}_i + \boldsymbol{R}_2) = \boldsymbol{u}_B(\boldsymbol{r}_i + \boldsymbol{R}_1) + ((\boldsymbol{R}_2 - \boldsymbol{R}_1) \cdot \nabla)\boldsymbol{u}_B(\boldsymbol{r}_i + \boldsymbol{R}_1) + \cdots$ and $\boldsymbol{u}_B(\boldsymbol{r}_i + \boldsymbol{R}_3)$ as $\boldsymbol{u}_B(\boldsymbol{r}_i + \boldsymbol{R}_3) = \boldsymbol{u}_B(\boldsymbol{r}_i + \boldsymbol{R}_1) + ((\boldsymbol{R}_3 - \boldsymbol{R}_1) \cdot \nabla)\boldsymbol{u}_B(\boldsymbol{r}_i + \boldsymbol{R}_1) + \cdots$, we see that Eq. (B.9) can be approximated by

$$\phi_A(\boldsymbol{r}_i) = g_{\text{on}} \nabla \cdot \boldsymbol{u}_B(\boldsymbol{r}_i + \boldsymbol{R}_1) + \cdots, \tag{B.10}$$

where we have used $\sum_{a=1,2,3} \boldsymbol{R}_a = 0$. It is noted that a general expression for the deformation potential, Eq. (B.10), is valid in the case that $\boldsymbol{u}_B(\boldsymbol{r})$ is a smooth function of $\boldsymbol{r}$. When this is not the case, we have to use Eq. (B.9). In the continuous limit, we may use $\boldsymbol{r}$ to represent the positions of both A and B atoms in the unit cell, then we have $\phi_A(\boldsymbol{r}) = g_{\text{on}} \nabla \cdot \boldsymbol{u}_B(\boldsymbol{r}) + \cdots$. Similarly, the deformation potential of B-site of $\boldsymbol{r}_i + \boldsymbol{R}_1$ is given by

$$\phi_B(\boldsymbol{r}_i + \boldsymbol{R}_1) = \frac{g_{\text{on}}}{\ell a_{\text{cc}}} \sum_{a=1,2,3} -\boldsymbol{R}_a \cdot (\boldsymbol{u}_A(\boldsymbol{r}_i + \boldsymbol{R}_1 - \boldsymbol{R}_a) - \boldsymbol{u}_B(\boldsymbol{r}_i + \boldsymbol{R}_1)). \tag{B.11}$$

By using $\boldsymbol{u}_A(\boldsymbol{r}_i + \boldsymbol{R}_1 - \boldsymbol{R}_2) = \boldsymbol{u}_A(\boldsymbol{r}_i) + ((\boldsymbol{R}_1 - \boldsymbol{R}_2) \cdot \nabla)\boldsymbol{u}_A(\boldsymbol{r}_i) + \cdots$ and $\boldsymbol{u}_A(\boldsymbol{r}_i + \boldsymbol{R}_1 - \boldsymbol{R}_3) = \boldsymbol{u}_A(\boldsymbol{r}_i) + ((\boldsymbol{R}_1 - \boldsymbol{R}_3) \cdot \nabla)\boldsymbol{u}_A(\boldsymbol{r}_i) + \cdots$, we see that Eq. (B.11) can be approximated by

$$\phi_B(\boldsymbol{r}_i + \boldsymbol{R}_1) = g_{\text{on}} \nabla \cdot \boldsymbol{u}_A(\boldsymbol{r}_i) + \cdots. \tag{B.12}$$

Thus, for the intravalley scattering, we may rewrite Eq. (B.8) using Eqs. (B.10) and (B.12) as

$$\mathcal{H}_{\text{on}} = g_{\text{on}} \begin{pmatrix} \nabla \cdot \boldsymbol{u}_B(\boldsymbol{r}) & 0 \\ 0 & \nabla \cdot \boldsymbol{u}_A(\boldsymbol{r}) \end{pmatrix} + \cdots. \tag{B.13}$$

According to the result of density-functional theory by Porezag *et al.*, [42] we use the parameter for g_{on} (=17eV). For the discussion of el-ph interaction of acoustic

$$s(\boldsymbol{r}) \equiv \frac{\boldsymbol{u}_{\mathrm{A}}(\boldsymbol{r}) + \boldsymbol{u}_{\mathrm{B}}(\boldsymbol{r})}{2}, \tag{B.14}$$

and optical

$$\boldsymbol{u}(\boldsymbol{r}) \equiv \boldsymbol{u}_{\mathrm{B}}(\boldsymbol{r}) - \boldsymbol{u}_{\mathrm{A}}(\boldsymbol{r}), \tag{B.15}$$

phonon modes, we can rewrite Eq. (B.13) using the Pauli matrices as

$$\mathcal{H}_{\mathrm{on}} = \frac{g_{\mathrm{on}}}{2}\sigma_0 \nabla \cdot (\boldsymbol{u}_{\mathrm{A}}(\boldsymbol{r}) + \boldsymbol{u}_{\mathrm{B}}(\boldsymbol{r})) + \frac{g_{\mathrm{on}}}{2}\sigma_z \nabla \cdot (\boldsymbol{u}_{\mathrm{B}}(\boldsymbol{r}) - \boldsymbol{u}_{\mathrm{A}}(\boldsymbol{r})). \tag{B.16}$$

Appendix C

Exciton-photon and exciton-phonon matrix elements

Here we describe how to obtain the exciton-photon and exciton-phonon matrix elements, which are used in Chapter 5. To calculate the exciton-photon and exciton-phonon matrix elements, we need information of the exciton energies and exciton wavefunctions. The exciton energy and exciton wave function coefficients are calculated by solving the Bethe-Salpeter equation as described in Sec. 2.4. All these calculations are performed within the extended tight-binding (ETB) approximation [84].

Exciton-photon matrix elements

The exciton-photon matrix elements between an excited state $|\Psi_0^n\rangle$ and the ground state $|0\rangle$ in the dipole approximation are expressed as [35]

$$\mathcal{M}_{\text{ex-op}} = \langle\Psi_0^n|H_{\text{el-op}}|0\rangle, \tag{C.1}$$

where $H_{\text{el-op}}$ is the electron-photon Hamiltonian. Due to the selection rule for the wave vector in the parallel polarization, we can write $H_{\text{el-op}}$ as

$$H_{\text{el-op}} = \sum_{\mathbf{k}} \mathcal{D}_{\mathbf{k}} c^{\dagger}_{\mathbf{k}c} c_{\mathbf{k}v}(a + a^{\dagger}), \tag{C.2}$$

where $\mathcal{D}_{\mathbf{k}}$ is the electron-photon interaction within the dipole approximation for a vertical transition between the initial and final states $\mathbf{k}$, $c^{\dagger}_{\mathbf{k}c}$ ($c_{\mathbf{k}v}$) is the electron creation (annihilation) operator in the conduction (valence) band, and $a^{\dagger}$ (a) is the photon creation (annihilation) operator. The exciton wave function $|\Psi_{\mathbf{q}}^n\rangle$ with a center-of-mass momentum $\mathbf{Q}$ is expressed as

$$|\Psi_{\mathbf{Q}}^n\rangle = \sum_{\mathbf{k}} Z^n_{\mathbf{k}c,(\mathbf{k}-\mathbf{K})v} c^{\dagger}_{\mathbf{k}c} c_{(\mathbf{k}-\mathbf{K})v}|0\rangle, \tag{C.3}$$

where $Z^n_{\mathbf{k}c,(\mathbf{k}-\mathbf{K})v}$ is the eigen vector of the n-th ($n = 1, 2, \dots$) state of the Bethe-Salpeter equation. In Eq. (C.3), instead of summation over all cutting lines μ (one-dimensional Brillouin zone of carbon nanotubes), we use a single cutting line for any optical transition under consideration [34], and thus the index μ is removed in Eq. (C.3). The exciton-photon matrix elements for the transition between the excited states $|\Psi^n_0\rangle$ and the ground states $|0\rangle$ are then given by

$$\mathcal{M}_{\text{ex-op}} = \sum_{\mathbf{k}} \mathcal{D}_{\mathbf{k}} Z^{n*}_{\mathbf{k}c,\mathbf{k}v}. \tag{C.4}$$

Exciton-phonon matrix elements

The exciton-phonon matrix elements $\mathcal{M}_{\text{ex-ph}}$ between the initial state $|\Psi^{n_1}_{\mathbf{Q}_1}\rangle$ and a final state $|\Psi^{n_2}_{\mathbf{Q}_2}\rangle$ are expressed by

$$\mathcal{M}_{\text{ex-ph}} = \langle \Psi^{n_2}_{\mathbf{Q}_2} | H_{\text{el-ph}} | \Psi^{n_1}_{\mathbf{Q}_1} \rangle, \tag{C.5}$$

where $H_{\text{el-ph}}$ is the Hamiltonian for the electron-phonon coupling for the ν-th phonon mode and a phonon wave vector $\mathbf{q} = \mathbf{Q}_1 - \mathbf{Q}_2$ obtained from the momentum conservation. Note that here we slightly modify the notation of the electron-phonon matrix element compared to that used in Sec. 3.5.1. By taking into account the contribution from the electron and hole scattering processes simultaneously in the electron-phonon Hamiltonian, we have

$$H_{\text{el-ph}} = \sum_{\mathbf{k}\mathbf{q}\nu} \left[\mathcal{M}^\nu_{\mathbf{k},\mathbf{k}+\mathbf{q}}(c) c^\dagger_{(\mathbf{k}+\mathbf{q})c} c_{\mathbf{k}c} - \mathcal{M}^\nu_{\mathbf{k},\mathbf{k}+q}(v) c^\dagger_{(\mathbf{k}+\mathbf{q})v} c_{\mathbf{k}v} \right] (b_{\mathbf{q}\nu} + b^\dagger_{\mathbf{q}\nu}), \tag{C.6}$$

where $\mathcal{M}(c)$ [$\mathcal{M}(v)$] is the electron-phonon matrix element for the conduction (valence) band and the operator $b^\dagger_{\mathbf{q}\nu}$ ($b_{\mathbf{q}\nu}$) corresponds to the phonon creation (annihilation) at the ν-th phonon mode $\mathbf{q}$. Using that Hamiltonian, we then obtain

$$\begin{aligned}
\mathcal{M}_{\text{ex-ph}} = &\langle \Psi^{n_2}_{\mathbf{Q}_2} | H_{\text{el-ph}} | \Psi^{n_1}_{\mathbf{Q}_1} \rangle \\
= &\sum_{\mathbf{k}} \Big[M^\nu_{\mathbf{k},\mathbf{k}+\mathbf{q}}(c) Z^{n_2*}_{(\mathbf{k}+\mathbf{q})c,(\mathbf{k}-\mathbf{Q}_1)v} Z^{n_1}_{\mathbf{k}c,(\mathbf{k}-\mathbf{Q}_1)v} \\
&- M^\nu_{\mathbf{k},\mathbf{k}+\mathbf{q}}(v) Z^{n_2*}_{(\mathbf{k}+\mathbf{Q}_2)c,\mathbf{k}v} Z^{n_1}_{(\mathbf{k}+\mathbf{K}_2)c,(\mathbf{k}+\mathbf{q})v} \Big].
\end{aligned} \tag{C.7}$$

For a first-order resonance process, we have $\mathbf{Q}_1 = \mathbf{Q}_2 = \mathbf{k}$. We also just consider $\nu = 0$ for the coherent phonon generation. Therefore, the exciton-phonon matrix element in Eq. (C.7) is simplified as

$$\mathcal{M}_{\text{ex-ph}} = \sum_{\mathbf{k}} [\mathcal{M}_{\mathbf{k}}(c) - \mathcal{M}_{\mathbf{k}}(v)] |Z_{\mathbf{k}}|^2. \tag{C.8}$$

If we compare the exciton-phonon matrix element in Eq. (C.8) with the electron-phonon matrix element in Eq. (3.21), which is used as the driving force term for the

coherent phonon generation, we can see the difference is only that the exciton-phonon matrix element has a weighting factor in terms of the wavefunction coefficient $Z_{\mathbf{k}}$. The summation of electron-phonon matrix elements with exciton wavefunctions makes the driving force localized with a Gaussian shape following the shape of the exciton wavefunctions. This assumption is considered in Chapter 5 when we simplify the driving force model considering the excitonic effects as a Gaussian function multiplied with the step function with a certain force amplitude that can be obtained numerically.

Appendix D

Solution to the Klein-Gordon Equation

Here we give a solution to the Klein-Gordon equation in Eq. (5.3) by using the Green's function method. We start with the nonhomogeneous Klein-Gordon equation,

$$\frac{\partial^2 Q(z,t)}{\partial t^2} - c^2 \frac{\partial^2 Q(z,t)}{\partial z^2} = S(z,t) - \kappa Q(z,t), \tag{D.1}$$

where we have the driving force in terms of a Gaussian,

$$S(z,t) = A_g e^{-z^2/2\sigma_z^2} \theta(t). \tag{D.2}$$

The solution for $Q(z,t)$ in the region $-L/2 < z < L/2$ with a boundary condition, $Q(-L/2, t) = Q(L/2, t) = 0$, can be expressed in terms of Green's function $G(z, z', t)$,

$$Q(z,t) = \int_0^t \int_{-\infty}^{\infty} S(z', t') G(z, z', t - t') \mathrm{d}z' \mathrm{d}t', \tag{D.3}$$

$$G(z, z', t) = \frac{2}{L} \sum_{n=0}^{\infty} \cos(q_n z) \cos(q_n z') \frac{\sin(t\sqrt{c^2 q_n^2 + \kappa})}{\sqrt{c^2 q_n^2 + \kappa}}, \tag{D.4}$$

where $q_n = n\pi/L$. Inserting Eq. (D.2) to $Q(z,t)$ above and defining $\omega_n = \sqrt{c^2 q_n^2 + \kappa}$, we obtain

$$Q(z,t) = \frac{2A_g}{L} \int_0^t \int_{-\infty}^{\infty} e^{-z'^2/2\sigma_z^2} \sum_{n=0}^{\infty} \cos(q_n z) \cos(q_n z') \frac{\sin(\omega_n(t - t'))}{\omega_n} \mathrm{d}z' \mathrm{d}t'$$

$$= \frac{2A_g}{L} \sum_{n=0}^{\infty} \frac{\cos(q_n z)}{\omega_n} \int_0^t \int_{-\infty}^{\infty} e^{-z'^2/2\sigma_z^2} \frac{(e^{iq_n z'} + e^{-iq_n z'})}{2} \sin(\omega_n(t - t')) \mathrm{d}z' \mathrm{d}t'. \tag{D.5}$$

We can do the two integrations in Eq. (D.5) separately, and thus

$$
\begin{aligned}
Q(z,t) &= \frac{A_g}{L} \sum_{n=0}^{\infty} \frac{\cos(q_n z)}{\omega_n} \int_0^t \sin(\omega_n(t-t'))\mathrm{d}t' \int_{-\infty}^{\infty} (\mathrm{e}^{iq_n z'} + \mathrm{e}^{-iq_n z'})\mathrm{d}z' \\
&= \frac{A_g}{L} \sum_{n=0}^{\infty} \frac{\cos(q_n z)}{\omega_n} \left(\frac{1}{\omega_n}[1 - \cos(\omega_n t)] \right) \left(2\sigma_z \sqrt{2\pi}\ \mathrm{e}^{-q_n^2 \sigma_z^2/2} \right) \\
&= \frac{2\sigma_z A_g \sqrt{2\pi}}{L} \sum_{n=0}^{\infty} \left[\frac{\mathrm{e}^{-q_n^2 \sigma_z^2/2}}{c^2 q_n^2 + \kappa} \left(\cos(q_n z) \times (1 - \cos(t\sqrt{c^2 q_n^2 + \kappa})) \right) \right], \quad \text{(D.6)}
\end{aligned}
$$

as we have already seen in Eq. (5.16).

Appendix E

Calculation programs

There are several programs used to perform the coherent phonon calculation. All the necessary programs can be found under the following directory in `FLEX` workstation:

`~nugraha/for/00phd/`

Hereafter, this directory will simply be referred to as `ROOT/` directory. More detailed explanations about how to use the programs are given in the `00README` file in each subdirectory of `ROOT`.

Coherent phonon amplitude and spectra

Without excitonic effects

Directory: `ROOT/coherent/`

Main Program: `coherent.f`

Using `coherent.f`, we can calculate the coherent phonon amplitudes and spectra of carbon nanotubes with typical calculation inputs such as (n, m) and pump-probe energy. The calculation is performed within the extended-tight binding method, *without* including the excitonic effects (Chapter 4).

With excitonic effects

Directory: `ROOT/cpexc/`

Main Program: `cpexc.f`

Same as above, this program calculates the coherent phonon amplitudes and spectra with typical calculation inputs such as (n, m) and pump-probe energy. The calculation is performed by including the excitonic effects (Chapter 5).

Armchair nanoribbon

Directory: `ROOT/gnrcp/`

Main Program: `aGNR.f`

We could obtain similar results of coherent phonon amplitudes and coherent phonon spectra for armchair graphene nanoribbons. Typical calculation inputs now are the number of A-B atom pairs along the ribbon width and the pump-probe energy. The calculation is performed within the extended-tight binding method.

Effective mass theory

Directory: `ROOT/elphanalytic/`

Main Programs: `coupling.f90, fit.f90`

These programs give the electron-phonon matrix elements within the effective mass theory and also some plotting utilities for the analytical formula given in Chapter 4.

Green's function solver

Directory: `ROOT/fgreen/`

Main Program: `green.f90`

This program calculates coherent phonon amplitudes using Green's function technique. The output of amplitude calculation is also used in the `cpexc.f` program.

Mathematica notebooks

Directory: `ROOT/math/`

Main Programs: `coherentphonon.nb, gaussexciton.nb`

We also use Mathematica software to simulate the coherent phonon amplitudes in carbon nanotubes, especially when including the exciton effects. These programs give animations of coherent phonon amplitudes as a function of time and space. The programs also give the average spatial amplitudes defined in Chapter 5. The output is then used to calculate the coherent phonon spectra in `cpexc.f` program.

Bibliography

[1] R. Saito, G. Dresselhaus, and M. S. Dresselhaus, Physical Properties of Carbon Nanotubes (Imperial College Press, London, 1998).

[2] M. Fujita, K. Wakabayashi, K. Nakada, and K. Kusakabe, J. Phys. Soc. Jpn. 65, 1920–1923 (1996).

[3] K. Wakabayashi, M. Fujita, H. Ajiki, and M. Sigrist, Phys. Rev. B 59, 8271–8282 (1999).

[4] A. Jorio, M. S. Dresselhaus, and G. Dresselhaus, Carbon Nanotubes: Advanced Topics in Synthesis, Structure, Properties, and Applications (Springer-Verlag, Berlin, 2008).

[5] J.-H. Kim, A. R. T. Nugraha, L. G. Booshehri, E. H. Haroz, K. Sato, G. D. Sanders, K.-J. Yee, Y.-S. Lim, C. J. Stanton, R. Saito, and J. Kono, Chem. Phys. 413, 55–80 (2013).

[6] A. Gambetta, C. Manzoni, E. Menna, M. Meneghetti, G. Cerullo, G. Lanzani, S. Tretiak, A. Piryatinski, A. Saxena, R. L. Martin, and A. R. Bishop, Nat. Phys. 2, 515–520 (2006).

[7] Y. S Lim, K. J. Yee, J. H. Kim, E. H. Haroz, J. Shaver, J. Kono, S. K. Doorn, R. H. Hauge, and R. E. Smalley, Nano Lett. 6, 2696–2700 (2006).

[8] J.-H. Kim, K.-J. Han, N.-J. Kim, K.-J. Yee, Y.-S. Lim, G. D. Sanders, C. J. Stanton, L. G. Booshehri, E. H. Hároz, and J. Kono, Phys. Rev. Lett. 102, 037402 (2009).

[9] T. Kobayashi, Z. Nie, J. Du, K. Okamura, H. Kataura, Y. Sakakibara, and Y. Miyata, Phys. Rev. B 88, 035424 (2013).

[10] A. V. Kuznetsov and C. J. Stanton, Phys. Rev. Lett. 73, 3243–3246 (1994).

[11] G. D. Sanders, C. J. Stanton, J.-H. Kim, K.-J. Yee, Y.-S. Lim, E. H. Hároz, L. G. Booshehri, J. Kono, and R. Saito, Phys. Rev. B 79, 205434 (2009).

[12] A. R. T. Nugraha, G. D. Sanders, K. Sato, C. J. Stanton, M. S. Dresselhaus, and R. Saito, Phys. Rev. B 84, 174302 (2011).

[13] G. D. Sanders, A. R. T. Nugraha, R. Saito, and C. J. Stanton, Phys. Rev. B 85, 205401 (2012).

[14] A. R. T. Nugraha, E. Rosenthal, E. H. Hasdeo, G. D. Sanders, C. J. Stanton, M. S. Dresselhaus, and R. Saito, Phys. Rev. B 88, 075440 (2013).

[15] H. J. Zeiger, J. Vidal, T. K. Cheng, E. P. Ippen, G. Dresselhaus, and M. S. Dresselhaus, Phys. Rev. B 45, 768–778 (1992).

[16] A. Laubereau and W. Kaiser, Rev. Mod. Phys. 50, 607–665 (1978).

[17] G. D. Sanders, A. R. T. Nugraha, K. Sato, J.-H. Kim, J. Kono, R. Saito, and C. J. Stanton, J. Phys. Cond. Matt. 25, 144201 (2013).

[18] Y.-S. Lim, J.-G. Ahn, J.-H. Kim, K.-J. Yee, T. Joo, S.-H. Baik, E. H. Haroz, L. G. Booshehri, and J. Kono, ACS Nano 4, 3222–3226 (2010).

[19] T. Dumitrică, M. E. Garcia, H. O. Jeschke, and B. I. Yakobson, Phys. Rev. Lett. 92, 117401 (2004).

[20] A. H. Romero, M. E. Garcia, F. Valencia, H. Terrones, M. Terrones, and H. O. Jeschke, Nano Lett. 5, 1361–1365 (2005).

[21] T. Dumitrică, M. E. Garcia, H. O. Jeschke, and B. I. Yakobson, Phys. Rev. B 74, 193406 (2006).

[22] F. Valencia, A. H. Romero, H. O. Jeschke, and M. E. Garcia, Phys. Rev. B 74, 075409 (2006).

[23] M. J. O'Connell, S. M. Bachilo, C. B. Huffman, V. C. Moore, M. S. Strano, E. H. Haroz, K. L. Rialon, P. J. Boul, W. H. Noon, C. Kittrell, J. Ma, R. H. Hauge, R. B. Weisman, and R. E. Smalley, Science 297, 593 (2002).

[24] C. L. Kane and E. J. Mele, Phys. Rev. Lett. 90, 207401 (2003).

[25] R. B. Weisman and S. M. Bachilo, Nano Lett. 3, 1235 (2003).

[26] R. Saito, G. Dresselhaus, and M. S. Dresselhaus, Phys. Rev. B 61, 2981–2990 (2000).

[27] F. Wang, G. Dukovic, L. E. Brus, and T. F. Heinz, Science 308, 838–841 (2005).

[28] J. Maultzsch, R. Pomraenke, S. Reich, E. Chang, D. Prezzi, A. Ruini, E. Molinari, M. S. Strano, C. Thomsen, and C. Lienau, Phys. Rev. B 72, 241402 (2005).

[29] T. Ando, J. Phys. Soc. Jpn. 66, 1066–1073 (1997).

[30] C. D. Spataru, S. Ismail-Beigi, L. X. Benedict, and S. G. Louie, Phys. Rev. Lett. 92, 077402 (2004).

[31] V. Perebeinos, J. Tersoff, and P. Avouris, Phys. Rev. Lett. 92, 257402 (2004).

[32] Thomas G. Pedersen, Phys. Rev. B 67, 073401 (2003).

[33] H. Zhao and S. Mazumdar, Phys. Rev. Lett. 93, 157402 (2004).

[34] J. Jiang, R. Saito, Ge. G. Samsonidze, A. Jorio, S. G. Chou, G. Dresselhaus, and M. S. Dresselhaus, Phys. Rev. B 75, 035407 (2007).

[35] J. Jiang, R. Saito, K. Sato, J. S. Park, Ge. G. Samsonidze, A. Jorio, G. Dresselhaus, and M. S. Dresselhaus, Phys. Rev. B 75, 035405 (2007).

[36] K. Nakada, M. Fujita, G. Dresselhaus, and M. S. Dresselhaus, Phys. Rev. B 54, 17954–17961 (1996).

[37] Y. W. Son, M. L. Cohen, and S. G. Louie, Phys. Rev. Lett. 97, 216803 (2006).

[38] Ge. G. Samsonidze. Photophysics of carbon nanotubes. PhD thesis, Massachusetts Institute of Technology, 2006.

[39] H. Kataura, Y. Kumazawa, Y. Maniwa, I. Umezu, S. Suzuki, Y. Ohtsuka, and Y. Achiba, Synthetic Metals 103, 2555 – 2558 (1999).

[40] S. M. Bachilo, M. S. Strano, C. Kittrell, R. H. Hauge, R. E. Smalley, and R. B. Weisman, Science 298, 2361 (2002).

[41] A. Jorio, M. A. Pimenta, A. G. Souza Filho, Ge. G. Samsonidze, A. K. Swan, M. S. Ünlü, B. B. Goldberg, R. Saito, G. Dresselhaus, and M. S. Dresselhaus, Phys. Rev. Lett. 90, 107403 (2003).

[42] D. Porezag, Th. Frauenheim, Th. Köhler, G. Seifert, and R. Kaschner, Phys. Rev. B 51, 12947 (1995).

[43] Ge. G. Samsonidze, R. Saito, N. Kobayashi, A. Grüneis, J. Jiang, A. Jorio, S. G. Chou, G. Dresselhaus, and M. S. Dresselhaus, Appl. Phys. Lett. 85, 5703 (2004).

[44] H. Raza and E. C. Kan, Phys. Rev. B 77, 245434 (2008).

[45] D. Kahn, K.W. Kim, and M.A. Stroscio, J. Appl. Phys. 89, 5107–5111 (2001).

[46] G. D. Mahan, Phys. Rev. B 65, 235402 (2002).

[47] R.A. Jishi, L. Venkataraman, M.S. Dresselhaus, and G. Dresselhaus, Chem. Phys. Lett. 209, 77–82 (1993).

[48] C. Lobo and J. L. Martins, Zeitschrift für Physik D 39, 159–164 (1997).

[49] G. D. Mahan and G. S. Jeon, Phys. Rev. B 70, 075405 (2004).

[50] F. Mazzamuto, J. Saint-Martin, A. Valentin, C. Chassat, and P. Dollfus, J. Appl. Phys. 109, 064516–064516 (2011).

[51] G. S. Jeon and G. D. Mahan, Phys. Rev. B 72, 155415 (2005).

[52] J. Kürti, G. Kresse, and H. Kuzmany, Physical Review B 58, 8869–8872 (1998).

[53] O. Dubay and G. Kresse, Phys. Rev. B 67, 035401 (2003).

[54] L.H. Ye, B.G. Liu, D.S. Wang, and R. Han, Phys. Rev. B 69, 235409 (2004).

[55] R. Gillen, M. Mohr, C. Thomsen, and J. Maultzsch, Phys. Rev. B 80, 155418 (2009).

[56] O. Madelung, Introduction to Solid-State Theory (Springer-Verlag, Berlin, 1978).

[57] K. Sato, R. Saito, J. Jiang, G. Dresselhaus, and M. S. Dresselhaus, Phys. Rev. B 76, 195446 (2007).

[58] E. E. Salpeter and H. A. Bethe, Phys. Rev. 84, 1232 (1951).

[59] M. Rohlfing and S. G. Louie, Phys. Rev. B 62, 4927 (2000).

[60] J. Jiang, R. Saito, A. Grüneis, G. Dresselhaus, and M. S. Dresselhaus, Carbon 42, 3169–3179 (2004).

[61] T. Michel, M. Paillet, J. C. Meyer, V. N. Popov, L. Henrard, and J.-L. Sauvajol, Phys. Rev. B 75(15), 155432 (2007).

[62] A. R. T. Nugraha, R. Saito, K. Sato, P. T. Araujo, A. Jorio, and M. S. Dresselhaus, Appl. Phys. Lett. 97, 091905 (2010).

[63] J. Jiang, R. Saito, A. GrÃijneis, G. Dresselhaus, and M.S. Dresselhaus, Chem. Phys. Lett. 392, 383–389 (2004).

[64] A. Grüneis, R. Saito, Ge. G. Samsonidze, T. Kimura, M. A. Pimenta, A. Jorio, A. G. Souza Filho, G. Dresselhaus, and M. S. Dresselhaus, Phys. Rev. B 67, 165402 (2003).

[65] V. N. Popov and L. Henrard, Phys. Rev. B 70, 115407 (2004).

[66] R. J. Elliott, Phys. Rev. 108, 1384–1389 (1957).

[67] W. H. Press, B. P. Flannery, S. A. Teukolsky, and W. T. Vetterling, Numerical Recipes in Fortran: The Art of Scientific Computing (Cambridge University Press, Cambridge, 1992).

[68] J. Jiang, R. Saito, Ge. G. Samsonidze, S. G. Chou, A. Jorio, G. Dresselhaus, and M. S. Dresselhaus, Phys. Rev. B 72, 235408 (2005).

[69] K. Sasaki, R. Saito, G. Dresselhaus, M. S. Dresselhaus, H. Farhat, and J. Kong, Phys. Rev. B 78, 235405 (2008).

[70] R. Saito and H. Kamimura, J. Phys. Soc. Jpn. 52(2), 407–416 (1983).

[71] K. Sasaki and R. Saito, Prog. Theor. Phys. Suppl. 176, 253–278 (2008).

[72] S. Kilina and S. Tretiak, Adv. Func. Mat. 17, 3405–3420 (2007).

[73] R. Saito, K. Sato, Y. Oyama, J. Jiang, Ge. G. Samsonidze, G. Dresselhaus, and M. S. Dresselhaus, Phys. Rev. B 72, 153413 (2005).

[74] M. Machón, S. Reich, H. Telg, J. Maultzsch, P. Ordejón, and C. Thomsen, Phys. Rev. B 71, 035416 (2005).

[75] H. Suzuura and T. Ando, Phys. Rev. B 65, 235412 (2002).

[76] Carsten Georgi, Alexander A. Green, Mark C. Hersam, and Achim Hartschuh, ACS Nano 4, 5914–5920 (2010).

[77] D. Kammerlander, D. Prezzi, G. Goldoni, E. Molinari, and U. Hohenester, Phys. Rev. Lett. 99, 126806 (2007).

[78] K. Matsuda, T. Inoue, Y. Murakami, S. Maruyama, and Y. Kanemitsu, Phys. Rev. B 77, 033406 (2008).

[79] R. Merlin, Solid State Commun. 102, 207–220 (1997).

[80] J. Maultzsch, S. Reich, C. Thomsen, E. Dobardzic, I. Milosevic, and M. Damnjanovic, Solid State Comm. 121, 471–474 (2002).

[81] R. Saito, M. Fujita, G. Dresselhaus, and M. S. Dresselhaus, Phys. Rev. B 46, 1804–1811 (1992).

[82] G. D. Sanders, C. J. Stanton, and Chang Sub Kim, Phys. Rev. B 64, 235316 (2001).

[83] S. Konabe, T. Yamamoto, and K. Watanabe, Appl. Phys. Express 2, 092202 (2009).

[84] K. Sato, R. Saito, A. R.T. Nugraha, and S. Maruyama, Chem. Phys. Lett. 497, 94–98 (2010).

Publication list

First-authored papers

(1) A. R. T. Nugraha, E. Rosenthal, E. H. Hasdeo, G. D. Sanders C. J. Stanton, M. S. Dresselhaus, R. Saito: "Excitonic effects on coherent phonon dynamics in single wall carbon nanotubes", Phys. Rev. B, 88, 075440 (2013).

(2) A. R. T. Nugraha, G. D. Sanders, K. Sato, C. J. Stanton, M. S. Dresselhaus, and R. Saito: "Chirality dependence of coherent phonon amplitudes in single wall carbon nanotubes", Phys. Rev. B 84, 174302 (2011).

(3) A. R. T. Nugraha, K. Sato, and R. Saito: "Confinement of excitons for the lowest optical transition energies of single wall carbon nanotubes", e-J. Surf. Sci. Nanotech. 8, 367-371 (2010).

(4) A. R. T. Nugraha, R. Saito, K. Sato, P. T. Araujo, A. Jorio, and M. S. Dresselhaus: "Dielectric constant model for environmental effects on the exciton energies of single wall carbon nanotubes", Appl. Phys. Lett. 97, 091905 (2010).

Co-authored papers

(5) E. H. Hasdeo, A. R. T. Nugraha, K. Sato, R. Saito, M. S. Dresselhaus: "Origin of electronic Raman scattering and the Fano resonance in metallic carbon nanotubes", Phys. Rev. B, in press, arXiv:1301.7585 (2013).

(6) G. D. Sanders, A. R. T. Nugraha, R. Saito, C. J. Stanton: "Coherent radial breathing like phonons in graphene nanoribbons", Phys. Rev. B 85, 205401 (2012).

(7) G. D. Sanders, A. R. T. Nugraha, K. Sato, J.-H. Kim, J. Kono, C. J. Stanton, R. Saito: "Theory of coherent phonons in carbon nanotubes and graphene", J. Phys. Cond. Mat. 25, 144201 (2013), Invited Review Article.

(8) J.H. Kim, A. R. T. Nugraha, L. G. Booshehri, E. H. Haroz, K. Sato, G. D. Sanders, K.-J. Yee, Y.-S. Lim, C.-J. Stanton, R. Saito, J. Kono: "Coherent phonons in carbon nanotubes and graphene", Chem. Phys. 413, 55-80 (2013), Invited Special Issue.

(9) S. Cambre, S. Santos, W. Wenseleers, A. R. T. Nugraha, R. Saito, L. Cognet, and B. Lounis: "Luminescence properties of individual empty and water-filled single-walled carbon nanotubes", ACS Nano 6, 2649-2655 (2011).

(10) M. M. Haque, L. C. Yin, A. R. T. Nugraha, and R. Saito: "Vibrational and NMR properties of polyynes", Carbon 49, 3340-3345 (2011).

(11) P. T. Araujo, A. R. T. Nugraha, K. Sato, M. S. Dresselhaus, R. Saito, A. Jorio: "Chirality dependence of the dielectric constant for the excitonic transition energy of single wall carbon nanotubes", Phys. Status Solidi B 247, 2847-2850 (2010).

(12) K. Sato, A. R. T. Nugraha, and R. Saito: "Excitonic effects on Raman intensity of single wall carbon nanotubes", e-J. Surf. Sci. Nanotech. 8, 358-361 (2010).

(13) K. Sato, R. Saito, A. R. T. Nugraha, and S. Maruyama: "Excitonic effects on radial breathing mode intensity of single wall carbon nanotubes", Chem. Phys. Lett. 497, 94-98 (2010).

Presentations in Conferences

Oral presentations

- A. R. T. Nugraha, E. H. Hasdeo, and R. Saito: "Excitonic effects on coherent phonon spectroscopy of single wall carbon nanotubes", the 44th Fullerene-Nanotubes-Graphene General Symposium (11-13 March 2013), Tohoku University, Japan.

- A. R. T. Nugraha, E. Rosenthal, and R. Saito: "Excitonic effects on coherent phonon oscillations in single wall carbon nanotubes", ATI 2012 Nano-Carbon Meeting and Zao12 Meeting (22-23 July 2012), Yamagata-Zao, Japan.

- A. R. T. Nugraha and R. Saito: "Coherent phonon amplitudes of single wall carbon nanotubes", ATI 2011 Nano-Carbon Meeting and Zao11 Meeting (2-3 August 2011), Yamagata-Zao, Japan.

- A. R. T. Nugraha and R. Saito: "Chirality dependence of coherent phonon amplitudes in single wall carbon nanotubes", East Asian Postgraduate Workshop on Nanoscience and Nanotechnology (15-17 June 2011), Hong Kong University of Science and Technology, Hong Kong.

Poster presentations

- A. R. T. Nugraha, E. Rosenthal, E. H. Hasdeo, and R. Saito: "Exciton effects on coherent phonons in carbon nanotubes.", A3 Symposium of Emerging Materials (29-31 October 2012), Tohoku University, Japan.

- A. R. T. Nugraha, G. D. Sanders, C. J. Stanton, and R. Saito: "Excitonic effects on coherent phonons in single wall carbon nanotubes.", the 43rd Fullerene-Nanotubes-Graphene General Symposium (5-7 September 2012), Tohoku University, Japan.

- A. R. T. Nugraha, K. Sato, and R. Saito: "Coherent phonon spectroscopy of RBM and RBLM phonons in carbon nanotubes and graphene nanoribbons", The 42nd Fullerene-Nanotubes-Graphene General Symposium (6-8 March 2012), University of Tokyo, Japan.

- A. R. T. Nugraha and R. Saito: "Theory of coherent phonon oscillations in carbon nanotubes and graphene nanoribbons", The 4th GCOE International Symposium (20-22 February 2012), Aobayama Campus of Tohoku University, Sendai, Japan.

- A. R. T. Nugraha, K. Sato, and R. Saito: "Excitation and chirality dependence of coherent phonons in carbon nanotubes", A3 Symposium of Emerging Materials (13-15 October 2011), Royal International Hotel, Urumqi, China.

- A. R. T. Nugraha, K. Sato, and R. Saito: "Chirality-dependent coherent phonon amplitudes in single wall carbon nanotubes", The 41st Fullerene-Nanotubes-Graphene General Symposium (5-7 September 2011), Tokyo Metropolitan University, Tokyo, Japan.

- A. R. T. Nugraha, K. Sato, and R. Saito: "Chirality dependence of coherent phonon amplitudes in single wall carbon nanotubes", The 40th Fullerene-Nanotubes General Symposium (8-10 March 2011), Meijo University, Nagoya, Japan.

- A. R. T. Nugraha and R. Saito: "Introduction to coherent phonon spectroscopy of carbon nanotubes", 6-Senkyou Joint Symposium (22 February 2011), Aobayama Campus of Tohoku University, Sendai, Japan.

- A. R. T. Nugraha and R. Saito: "Excitation energy dependence of coherent phonon amplitudes in single wall carbon nanotubes", The 3rd GCOE International Symposium (17-19 February 2011), Aobayama Campus of Tohoku University, Sendai, Japan.